24/phdap/11 SATYAM SINGH

plag check copy

Paper Check

Document Details

Submission ID
trn:oid:::27535:135202535

Submission Date
Apr 14, 2026, 8:46 PM GMT+5:30

Download Date
Apr 14, 2026, 8:51 PM GMT+5:30

File Name
plag check copy.pdf

File Size
6.0 MB

167 Pages

30,016 Words

160,193 Characters

4% Overall Similarity

The combined total of all matches, including overlapping sources, for each database.

Filtered from the Report

- Bibliography
- Quoted Text
- Cited Text
- Small Matches (less than 14 words)

Exclusions

- 1 Excluded Source

Match Groups

58 Not Cited or Quoted 4%
Matches with neither in-text citation nor quotation marks

0 Missing Quotations 0%
Matches that are still very similar to source material

0 Missing Citation 0%
Matches that have quotation marks, but no in-text citation

0 Cited and Quoted 0%
Matches with in-text citation present, but no quotation marks

Top Sources

2% Internet sources
2% Publications
1% Submitted works (Student Papers)

Match Groups

- **58** Not Cited or Quoted 4%
  Matches with neither in-text citation nor quotation marks
- **0** Missing Quotations 0%
  Matches that are still very similar to source material
- **0** Missing Citation 0%
  Matches that have quotation marks, but no in-text citation
- **0** Cited and Quoted 0%
  Matches with in-text citation present, but no quotation marks

Top Sources

2% Internet sources
2% Publications
1% Submitted works (Student Papers)

Top Sources

The sources with the highest number of matches within the submission. Overlapping sources will not be displayed.

1	Publication	Manish, Naveen, Karanpal Singh, Amir Khan, Amrish K. Panwar, Tensangmu Lam...	<1%
2	Student papers	University of Auckland on 2024-04-21	<1%
3	Publication	Hyeonjin Kim, Sinho Choi, Dong-Hyun Peck, Seog-Young Yoon. "Influence of the c...	<1%
4	Internet	www.mdpi.com	<1%
5	Publication	Yongping Pu, Zijing Dong, Panpan Zhang, Yurong Wu, Jiaojiao Zhao, Yanjie Luo. "...	<1%
6	Internet	ira.lib.polyu.edu.hk	<1%
7	Internet	www.osti.gov	<1%
8	Internet	scholar.ui.ac.id	<1%
9	Publication	S. S. Batool, Z. Imran, Kamran Rasool, Jaweria Ambreen, Safia Hassan, Saira Arif, ...	<1%
10	Internet	hal.science	<1%

11 Publication
Jian- Fang Wu, Zheyi Zou, Bowei Pu, Lukas Ladenstein et al. "Liquid-like Li-ion Con... <1%

12 Student papers
University of Akron on 2024-06-13 <1%

13 Internet
depot-e.uqtr.ca <1%

14 Student papers
University of St Andrews on 2025-03-08 <1%

15 Internet
etheses.whiterose.ac.uk <1%

16 Internet
scholar.uoc.ac.in <1%

17 Internet
scholar.ufs.ac.za <1%

18 Internet
sure.su.ac.th <1%

19 Student papers
University of Sheffield on 2025-01-25 <1%

20 Internet
opus.lib.uts.edu.au <1%

21 Internet
pubs.rsc.org <1%

22 Internet
www.arlis.org <1%

23 Internet
www.diva-portal.org <1%

24 Student papers
Banaras Hindu University on 2022-06-06 <1%

25 Student papers
Korea University on 2021-04-12 <1%

26 Internet
dyuthi.cusat.ac.in <1%

27 Internet
link.springer.com <1%

28 Student papers
University of Sheffield on 2023-08-17 <1%

29 Student papers
University of Sheffield on 2023-09-29 <1%

30 Publication
V.C. Martins, R.F. Abreu, F.A.C. Nobrega, F.F. do Carmo et al. "Study of the structur... <1%

31 Internet
discovery.ucl.ac.uk <1%

32 Internet
ir.lib.uwo.ca <1%

33 Student papers
Curtin University of Technology on 2025-08-31 <1%

34 Publication
Km. Komal, Mukhtiyar Singh, Bharti Singh. "One step hydrothermal synthesis of ... <1%

35 Student papers
Malaviya National Institute of Technology on 2019-07-19 <1%

36 Student papers
University of St Andrews on 2013-04-18 <1%

37 Publication
Vijayakumar Prabu, Kathiresan Geetha, Ramachandran Sekar, Mani Ulaganathan... <1%

38 Internet
coek.info <1%

39 Internet

etd.lib.metu.edu.tr <1%

40 Internet

patents.google.com <1%

41 Internet

strathprints.strath.ac.uk <1%

ABSTRACT

The global transition toward carbon-neutral energy systems, transportation, and resilient grid-storage infrastructures has intensified the demand for rechargeable energy-storage technologies that simultaneously deliver high energy density, safety, long cycle life, and robust operational stability. Lithium-ion batteries (LIBs), despite of their widespread acceptance and decades of technological refinements, remain constrained by certain limitations associated with their liquid-electrolyte-based architecture. Organic carbonate electrolytes composed of $LiPF_6$, $LiClO_4$, or other similar salts dissolved in ethylene carbonate, dimethyl carbonate, and related solvents also offer high ionic mobility. But due to volatility, flammability, and electrochemical instability toward both the highly reducing lithium metal and the oxidative surfaces of high-voltage cathodes, they resist the use of a liquid electrolyte system. These limitations of liquid electrolytes have motivated a paradigm shift toward solid-state electrolytes (SSEs) as a pathway to develop fundamentally safer, more stable, high-performance next-generation rechargeable batteries. SSEs restrict the flammable liquid phase and introduce solid ion-conducting media. They are capable of withstanding high voltages, suppressing dendrites, and operating across a broad temperature range. The inherent high thermal stability, wide electrochemical window, and compatibility with lithium metal anodes create opportunities for transformative gains in energy density and long-term reliability.

Ceramic electrolytes offer highly ordered three-dimensional ion-migration networks with conductivities competing with those of liquids. The structure of LISICON-type,

NASICON-type, perovskite-type, sulfide-based, and garnet-type materials exhibits diverse frameworks for Li-ion conduction, each defined by distinct lattice polarizability, defect chemistries, and conduction topologies. Among the growing class of ceramic SSEs, garnet-type $Li_7La_3Zr_2O_{12}$ (LLZO) has emerged as a compelling SSE material for next-generation solid-state lithium-ion batteries. LLZO offers a unique combination of high ionic conductivity (~10^{-4} Scm^{-1}) in its cubic phase, exceptional stability against lithium metal, and a wide electrochemical window extending beyond 5 V. In contrast, the tetragonal polymorph exhibits ordered Li-site occupation, higher activation energy, and substantially reduced conductivity. Despite its intrinsic advantages, LLZO still has scientific challenges, such as high-temperature sintering, which exacerbates lithium volatilization, leading to impurity phases like $La_2Zr_2O_7$ or other oxides that impede ionic transport. The tendency of LLZO to react with atmospheric CO_2 and H_2O forms resistive Li_2CO_3 surface layers that degrade interfacial conductivity. Hence, to obtain high-density microstructures, there is an essential requirement of careful optimization of sintering schedules, dopant chemistry, and powder-processing routes.

Similar to the garnet-type SSEs, phosphate-based solid electrolytes such as $LiTa_2PO_8$ (LTPO) represent a structurally robust family of materials with excellent thermal stability, versatile cation substitution, and favorable electrochemical behavior. The LTPO and Zr doping in LTPO, abbreviated as LTZPO, introduces controlled lattice strain, modifies grain-boundary behaviour, and affects the sintering behaviour, resulting in improved densification and transport pathways. These characteristics also render LTZPO an effective sintering additive for garnet electrolytes, enabling microstructure refinement

and grain-boundary engineering in composite systems. Therefore, the convergence of these scientific insights motivates a comprehensive investigation of solid-state electrolytes: phosphate-based $LiTa_2PO_8$, Zr-doped $LiTa_2PO_8$ ($Li_{1+x}Ta_{2-x}Zr_xPO_8$), and oxide-based Ce-doped $Li_7La_3Zr_2O_{12}$ ($Li_7La_3Zr_{2-x}Ce_xO_{12}$), and finally the LLZCO–LTZPO composite electrolytes. Hence, each system offers a distinct window into the interplay between composition, structure, microstructure, and ionic transport.

This research work also aims to deepen the scientific understanding of how structural heterogeneity, grain-boundary effects, dopant incorporation, and composite design govern ionic transport in solid-state electrolytes. By establishing clear correlations between structural, microstructural, and electrochemical performances. This research contributes to the rational design of next-generation SSEs capable of enabling safe, high-energy density, and durable all-solid-state rechargeable Li-ion batteries.

The findings of the present research have been organized into seven chapters within the thesis, each outlined briefly as follows:

Chapter 1 introduces the motivation behind developing solid-state electrolytes for next-generation rechargeable lithium-ion batteries. It outlines the limitations of conventional liquid electrolytes and explains how solid-state electrolytes offer better safety, wider electrochemical stability, and compatibility with lithium metal along with the detailed literature review on solid state electrolytes developed so far.

Chapter 2 covers the synthesis approach and characterization techniques to prepare SSEs. All solid-state electrolytes are prepared through the conventional solid-state

reaction route. Thermal behavior has been examined using Thermogravimetric Analysis and Differential Scanning Calorimetry (TGA/DSC), while structural analysis and phase identification have been performed using X-ray diffraction (XRD) patterns. The microstructural feature study and dielectric properties investigation are carried out using Scanning Electron Microscopy (SEM), Transmission Electron Microscopy (TEM), and an LCR meter, respectively. The electrochemical performance for symmetric and full-cell testing has been performed using a potentiostat and galvanostatic battery cycling system.

Chapter 3 investigates the synthesis, structural evolution, and ionic transport behaviour of the $LiTa_2PO_8$ (LTPO) solid-state electrolyte. LTPO has been synthesized via a solid-state reaction route. The thermal analysis (TGA/DSC) up to a temperature of 1100 °C guided the selection of a multi-step sintering profile. XRD measurement confirmed monoclinic LTPO as the primary phase with traces of trigonal $LiTaO_3$ phase, while microstructural characterization revealed highly dense and heterogeneous grain distribution, particularly under step-sintering conditions. Dielectric studies indicate Maxwell–Wagner relaxation with clear frequency-dependent dispersion, and impedance spectroscopy identified distinct grain and grain-boundary contributions to ion transport. The electrochemical performance of LTPO has been investigated using a buffer layer at the electrolyte/electrode interface in a quasi-solid-state cell.

Chapter 4 focuses on enhancing the ionic conductivity of LTPO through zirconium substitution doping at the Ta site to prepare Zr-doped LTZPO solid electrolytes

30

synthesized via the solid-state reaction route. X-ray diffraction confirmed the formation of monoclinic phase LTZPO with the appearance of a secondary $LiTa_3O_8$ phase upon Zr incorporation. Pre-sintering particle size reduction indicates a significant role in modifying the structural characteristics, while finer particles induced compressive stresses in the pellet. An electrochemical study has been performed using symmetric Li|LTZPO|Li cells across different temperatures, showing remarkable stability, maintaining continuous cycling for up to 1500 hours.

Chapter 5 includes the structural and impedance analysis of Ce-doped $Li_7La_3Zr_2O_{12}$ (LLZCO) solid electrolyte synthesized through the solid-state reaction method. X-ray diffraction confirmed the stabilization of the cubic garnet phase upon Ce substitution, accompanied by a minor $Ce_{0.8}La_{0.2}O_{1.9}$ impurity phase. The detailed impedance deconvolution has been carried out to separate bulk, grain-boundary, and electrode interface contributions, allowing a clearer interpretation of relaxation processes influencing lithium-ion conduction. Electrochemical analysis the electrolytes has been measured in both symmetric and full solid-state cell configurations.

Chapter 6 investigates the electrochemical performance of LLZCO–LTZPO composite solid-state electrolytes designed to improve densification, grain-boundary characteristics, and overall ionic transport of the composite electrolyte system. The composite electrolytes were synthesized using a conventional sintering approach, where LTZPO is incorporated as a sintering additive into LLZCO. XRD analysis confirmed the successful composite formation for samples containing variable weight percentage (0-

25%) LTZPO in LLZCO. Complementary SEM and DRT analyses revealed the distribution of LTZPO predominantly along grain boundaries. The electrochemical behaviour of these composite electrolytes has been measured in both symmetric and full solid-state cell configurations.

Chapter 7 summarizes the major outcomes of the research work conducted in the thesis research~~,~~. The chapter highlights the successful synthesis and characterization of LTPO, LTZPO, LLZCO, and LLZCO-LTZPO, composite electrolytes, along with insights into their structural evolution, densification mechanisms, ionic transport pathways, and electrochemical performance. This chapter also outlines the future directions for improving ion kinetics in solid-state batteries, such as microstructure refinement, interface surface engineering, advanced sintering strategies, in-situ diagnostic studies, scalable fabrication routes and the further incorporation of these ceramic solid electrolytes in polymer membranes for polymer-ceramic hybrid solid state electrolyte development and long-term cycling assessments for pre-commercial readiness along with the broader societal relevance of solid-state electrolytes, particularly their role in enabling safer, non-flammable batteries, extending storage lifetimes for electric vehicles, and renewable-energy systems, reducing environmental footprint, strengthening energy security, and supporting technological leadership in next-generation energy-storage technologies.

LIST OF PUBLICATIONS

1. Sharad Singh Jadaun, Amrish K. Panwar*, Geetanjali, "Quantitative Resolution of Grain Boundary Impedance in Ce-doped $Li_7La_3Zr_2O_{12}$ solid state electrolyte through Distribution of Relaxation Time Analysis and Electrochemical performance in quasi solid-state batteries", AIP- Applied Physics Letters, 128(2), (2026) **(Impact Factor: 3.6)**

2. Sharad Singh Jadaun, Amrish K. Panwar*, Geetanjali, "Effects of heterogeneous structure on conduction mechanism and electrochemical performance of $LiTa_2PO_8$-fast lithium-ion conductor in quasi-solid-state lithium-ion batteries". *Journal of Energy Storage*, *115*, 116030, (2025) (**Impact Factor: 9.8**)

3. Sharad Singh Jadaun, Amrish K. Panwar*, Geetanjali, "The Effect of Multi-step Sintering on the density of $Li_7La_3Zr_{1.75}Ce_{0.25}O_{12}$ as Solid State Electrolyte Material". Indian Journal of Pure & Applied Physics (IJPAP), 62(2), 116-123, (2024) **(Impact Factor:1.1)**

4. Sharad Singh Jadaun, Puneet Kumar, Amrish k. Panwar*, Geetanjali. "Influence of Zr substitution on ionic transport and temperature dependent electrochemical performance of $Li_{1+x}Ta_{2-x}Zr_xPO_8$ solid state electrolyte". **(ready to be communicated)**

5. Sharad Singh Jadaun, Satyam Singh, Amrish K. Panwar* and Geetanjali ,"Time-Resolved Impedance Analysis of LLZCO@ LTZPO Composite Li Ion Conductor for All Solid State Lithium Batteries",. **(ready to be communicated)**

List of Research Publications not included in thesis

1. Bittu Singh, Anshu Tamta, Bhuwan Chandra, N.D. Kandpal, Sharad S. Jadaun, Amrish K. Panwar, K. Vijaya Babu, Ponniah Justin, H. Seshagiri Rao, Chandra Sekhar,"Structural, Optical, Electrical, and Electrochemical properties of $ZnMoO_4$ microspheres synthesized by the twin crystal method. Ceramics International", 49(23), 38047-38057, (2023). **(Impact Factor: 5.6)**

2. Sweta Mehra, Sharad Singh Jadaun, Anil Kumar, Amrish K. Panwar "Study of Lithium-Ion Diffusion Coefficients Through Analysis of CV and EIS for $NiMn_2O_4$ Alternate Anode Material in Lithium-Ion Batteries", Journal of Electronic Materials, 54(10), 8439-8447, (2025). **(Impact Factor: 2.5)**

Research Work Presented at International Conferences

41

1. Presented poster at in International Conference on Thin Films and Nanotechnology-Knowledge, Leadership and Commercialization (ICTN-KLC -2023) on the topic, "Investigation of Ho doped LLZO and its polymer hybrid PEO/LLZHO as solid state electrolyte for rechargeable batteries"in Indian Institute of Technology, Madras.

2. Presented Poster at “International Conference on Advanced Materials for Emerging Technologies (ICAMET -2023)” on the topic, “Effects of Sintering temperature on density of $Li_7La_3Zr_{1.75}Ce_{0.25}O_{12}$ solid state electrolyte in NSUT, New Delhi.

3. Presented poster at “International Meeting on Energy storage Devices, IMESD-2023” on the topic, “Impact of Sn based alloy as interlayer on Li/solid electrolyte interface for solid state batteries in IIT Roorkee, Uttarakhand

4. Presented poster at “International Conference on Energy Materials and Rechargeable Batteries (ICEMRB-2023)” on the topic, “Investigation of structural, Morphological and dielectric properties of Ce doped LLZO solid state electrolyte in Manav Rachna University, Faridabad. **(Best Poster Award)**

5. Presented poster at “Advances in Sustainable Solution for Energy Transitions (ASSET-2025)on the topic, “Enhancing Stability in Solid-State Lithium Batteries: The Role of Metallic Interlayers in Preventing Dendrite Growth” in IIT Guwahati, Assam.

LIST OF PATENTS

1. Patent no. **586830**, Title: ADVANCED STEP SINTERING METHOD FOR THE SYNTHESIS OF CERAMIC SOLID-STATE ELECTROLYTE AND USE THEREOF. (**Granted**)

   Inventors: Sharad Singh Jadaun, Puneet Kumar, Amrish K. Panwar, Geetanjali

2. Patent application no. **202511056290**, Title: A NASICON-TYPE SOLID-STATE ELECTROLYTE FOR ALL-SOLID-STATE SODIUM-ION BATTERIES, AND A METHOD OF PREPARING THE SAME. (**Published**)

   Inventors: Sharad Singh Jadaun, Puneet Kumar, Amrish K. Panwar, Geetanjali

3. Patent application no. **202511076422**, Title: SYSTEM AND METHOD FOR LITHIUM/SODIUM MELTING FOR ENHANCED ELECTRODE–ELECTROLYTE INTERFACE ENGINEERING. (**Published**)

   Inventors: Sharad Singh Jadaun, Amrish K. Panwar, Geetanjali

4. Patent application no. **202511120746,** Title: A PORTABLE DEVICE AND METHOD FOR PERFORMANCE TESTING OF AT LEAST ONE RECHARGEABLE BATTERY (**Published**)

   Inventors: Sharad Singh Jadaun, Amrish K. Panwar

22

LIST OF FIGURES

LIST OF TABLES

Table of Contents

Chapter 1

Introduction and Literature Review

This chapter introduces the motivation behind developing solid-state electrolytes for next-generation rechargeable lithium-ion batteries. It outlines the limitations of conventional liquid electrolytes and explains how solid-state electrolytes offer better safety. Moreover, brief literature reviews of different classes of solid electrolytes, including polymer, ceramic, and composite systems, are explored. The detailed description of the material of interest of the present study, like garnet-type LLZO and phosphate-based materials such as LTPO and LTZPO are also extensively reviewed.

1.1 Background

The global energy economy has been under severe stress due to the rapid depletion of fossil fuel reserves and the escalating environmental consequences associated with their consumption. The extensive use of fossil fuels in power generation, industrial operations, and transportation has resulted in the large-scale emission of greenhouse gases that significantly accelerates global warming and induces irreversible climatic changes. The increasing atmospheric concentration of CO_2 has intensified concerns regarding environmental sustainability and energy security, necessitating an urgent transition toward cleaner and renewable energy technologies [1,2]. To mitigate these environmental challenges, the integration of green and sustainable energy sources such as wind, solar, geothermal, and bioenergy has become a global priority [3-4]. However, renewable energy systems are inherently intermittent and require efficient energy storage technologies to ensure a stable power supply and grid reliability. It has been predicted that, assuming the current rate of fossil fuel consumption, global energy demand could nearly double by 2050. Hence, emphasizing the critical need for clean, sustainable, and cost-effective next-generation energy storage devices [5-6]. Among various energy storage technologies, rechargeable batteries have emerged as the most promising candidates due to their high efficiency, portability, and scalability. In particular, lithium-ion batteries (LIBs) have revolutionized modern energy storage owing to their superior energy density, long cycle life, and excellent electrochemical performance [7-8]. LIBs have been extensively adopted in a wide spectrum of applications ranging from portable electronic devices such as mobile phones, cameras, and laptops to large-scale systems

including electric vehicles (EVs), hybrid electric vehicles (HEVs), aerospace systems, and marine technologies [9-11]. Despite their widespread commercial success and decades of technological refinement, conventional LIBs remain constrained by intrinsic limitations associated with their liquid-electrolyte-based architecture [12]. Organic carbonate electrolytes containing lithium salts like $LiPF_6$, $LiClO_4$ etc. provide high ionic conductivity; however, their volatility, flammability, and electrochemical instability toward both high-voltage cathodes and lithium metal anodes impose serious safety and durability concerns [12-14]. These fundamental limitations have stimulated intensive research efforts toward the development of solid-state electrolytes (SSEs) by eliminating the flammable liquid component and introducing solid ion-conducting frameworks capable of enhanced thermal stability, wider electrochemical windows, and improved interfacial compatibility [15-16]. Therefore solid-state batteries are considered to be a transformative technology capable of delivering safer, high-energy-density, and long-cycle-life energy storage systems suitable for future transportation and grid-scale applications [17-18].

1.2 History

The evolution of electrochemical energy storage systems dates back to the late eighteenth century. The first electrochemical battery, known as the Voltaic pile, was invented by Italian physicist Alessandro Volta in 1798. This early device consists of alternating zinc and copper plates separated by a brine-soaked cloth that acts as the electrolyte. The Voltaic pile provides the feasibility of sustained electric current

generation. Though it suffered from significant drawbacks like short operational lifespan, electrolyte leakage, and corrosion of zinc plates [19]. William Cruickshank introduced subsequent improvements. He proposed arranging the plates horizontally in a trough configuration to mitigate electrolyte leakage, leading to the development of the trough battery [20,21]. However, hydrogen bubble formation on the copper electrode and zinc degradation continued to limit battery efficiency. In 1836, John Frederick Daniell addressed this issue by introducing a second electrolyte system, resulting in the Daniell cell, which effectively minimized hydrogen polarization and provided improved voltage stability [22]. The advancement of rechargeable battery systems began with the pioneering work of Gaston Planté in 1859, with the development of the first rechargeable lead–acid battery. This invention marked a significant milestone in electrochemical storage technology, and improved versions of lead–acid batteries are still widely used in variable applications. The continuous development of electrochemical systems led to the introduction of alkaline batteries and subsequently, to nickel-based rechargeable systems such as Ni-Cd and Ni-MH batteries [23,24]. However, increasing technological demands for higher energy density and higher power density devices important for the development of next-generation rechargeable systems.

Lithium emerged as a highly attractive candidate for battery chemistry due to its electrochemical potential equals to -3.04 V vs. SHE and high theoretical capacity. Early lithium metal batteries offered high energy density but were plagued by safety concerns related to dendrite formation and short-circuiting while long term cycling. To overcome these limitations, researchers began exploring lithium intercalation compounds as safer

alternatives to metallic lithium electrodes. Between 1974, Besenhard proposed the concept of reversible lithium intercalation in graphite anodes [25,26]. A breakthrough occurred in 1979 when John B. Goodenough and co-workers discovered lithium cobalt oxide as a high-voltage cathode material [27]. Initial rechargeable configurations utilized $LiCoO_2$ as the positive electrode and lithium metal as the negative electrode. This discovery demonstrated that lithium could be reversibly inserted and extracted from layered oxide structures, eliminating the need for metallic lithium in practical systems. Further the advancements followed rapidly. In the year 1981 Bell Laboratories, demonstrated reversible lithium intercalation into graphite, leading to the development of the LiC_6 electrode structure [28]. In the year 1983, manganese based spinel ($LiMn_2O_4$) was investigated as a cathode material offering improved thermal stability and cost effectiveness [29]. Various layered and spinel compounds like $LiNiO_2$ and Li_2MnO_3 were also explored to enhance electrochemical performance. Akira Yoshino achieved the commercialization milestone by developing a prototype lithium-ion battery employing $LiCoO_2$ as the cathode and a carbon-based anode, replacing metallic lithium and significantly improving safety concerns [30]. This configuration became the foundation of modern lithium-ion batteries, which were later commercialized in the early 1990s. Despite of their commercial success, conventional lithium-ion batteries continued to rely on liquid electrolytes leading to issues in intrinsic safety and stability [12-14]. As energy density requirements increased, particularly with the growing interest in lithium metal anodes and high-voltage cathodes, the focus of research gradually shifted towards SSEs capable of offering enhanced safety, wider electrochemical

windows, and improved interfacial stability [15-18]. The development of solid ion conductors progressed in parallel with the evolution of lithium-ion battery technology. Early lithium superionic conductors (LISICON) material demonstrated promising ionic conductivities [31]. A significant advancement was taken place with the discovery of high-conductivity garnet-type, $Li_7La_3Zr_2O_{12}$ (LLZO), which exhibited superior chemical stability against lithium metal [32]. More recently, phosphate-based solid electrolytes such as $LiTa_2PO_8$ (LTPO) have emerged as structurally stable frameworks with tunable defect chemistry and promising electrochemical behavior [33].

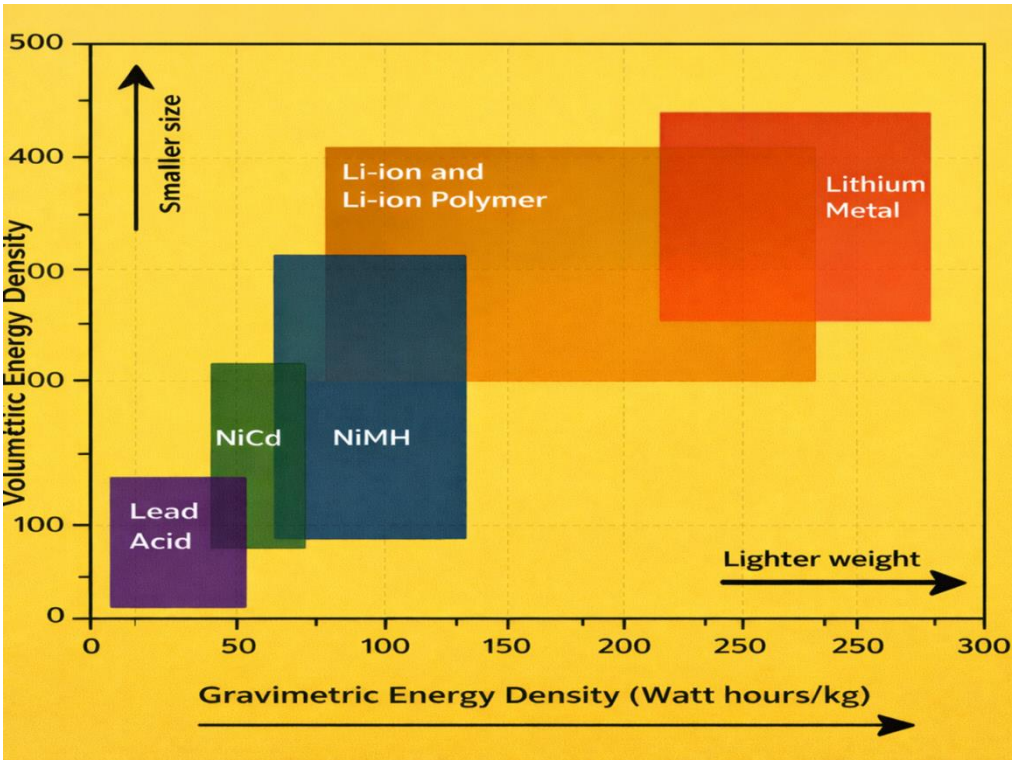

Figure 1.1: Graph between the volumetric and gravimetric energy density of different battery technologies

Thus, the historical progression from primary batteries to rechargeable lead–acid systems, nickel-based batteries, lithium metal systems, and finally lithium-ion intercalation chemistry reflects continuous efforts to improve energy density, safety, and cycling stability. The current transition toward solid-state lithium-ion batteries represents the next evolutionary stage in electrochemical energy storage, aiming to overcome the limitations of liquid electrolytes while enabling high-performance and intrinsically safe battery architectures. Figure 1.1 shows the graph between the volumetric and gravimetric energy of different battery technologies.

1.3 Basics of Lithium-ion Batteries (LIBs)

A lithium-ion battery is an electrochemical device that produces electrical energy via an electrochemical reaction. A basic Li-ion cell consists of four fundamental components: an anode, a cathode, a separator, and an electrolyte. The cathode and anode are the charge carriers providing the storage and release of electrochemical energy. The separator is a microporous membrane that enables the movement of Li-ions between the cathode and anode while obstructing the flow of electrons, thus averts short circuits. The electrolyte consists of Li-ions. The cathode serves as the positive electrode, and the anode as the negative electrode. The designation of cathode and anode is determined by the direction of the current flow [34,35].

Commercial cathodes are mainly lithium transition metal oxides or phosphates, and at the anode side, and graphite is used at the cathode side[36-39]. During charging, Li-ions move from the cathode to the anode, moving through the electrolyte and separator

before intercalating within the anode, transforming electrical energy into chemical energy. During discharging Li-ions travel back towards the cathode, releasing stored chemical energy and producing electrical energy [40-41]. The schematic of the working mechanism of LIB is shown in Fig. 1.2. The electrochemical mechanism occurring in a LIB can be expressed as:

At cathode: $$Li_{1-x}CoO_2 + xLi^+ + xe^- \leftrightarrow LiCoO_2 \quad (1.1)$$

At anode: $$Li_xC_6 \leftrightarrow 6C + xLi^+ + xe^- \quad (1.2)$$

Overall reaction: $$Li_xC_6 + Li_{1-x}CoO_2 \leftrightarrow LiCoO_2 + 6C \quad (1.3)$$

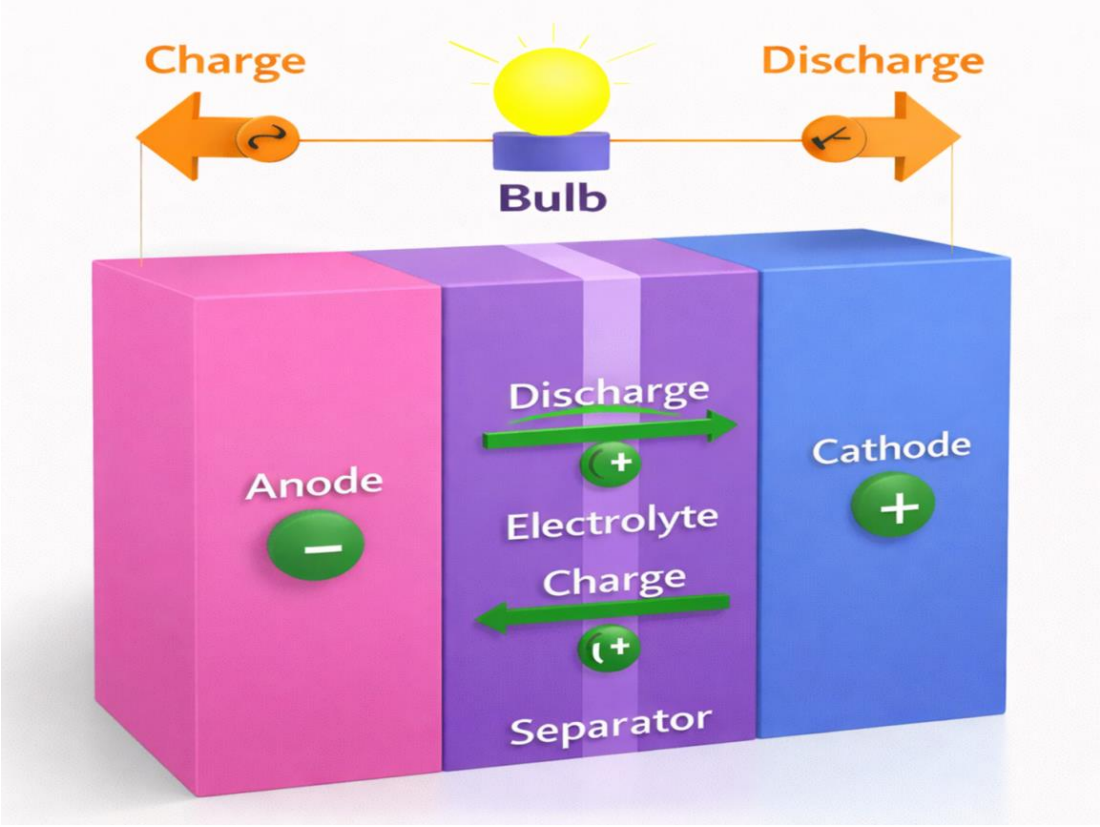

Figure 1.2: Schematic representation of the working mechanism of LIBs

1.4 Components of LIBs

1.4.1 Anode

A battery's anode or negative electrode gets oxidized during an electrochemical process that results into the release of electrons in the external circuit. This process contributes significantly to the overall electrochemical performance of a battery. There are a variety of anode materials in LIBs, including graphite, silicon (Si), intermetallic and alloying materials. In addition to producing stable and reversible gravimetric and volumetric capacity, an ideal anode material must have a low density that can hold more Li-ions in its crystal structure, and its potential must be close to that of Li metal, and it must be chemically stable in the presence of different electrolytes [42-44].

25

1.4.2 Cathode

The cathode is the positive electrode that absorbs electrons from the external circuit during the discharge mechanism. It serves as the active source for all of the Li-ions and is another crucial and significant part of a battery. The ideal lithium battery should have a cathode material with a high discharge capacity, long cycle life, low self-discharge, and high voltage. The first cathode $LiCoO_2$ was discovered by John B. Goodenough as the first layered transition metal oxide cathode to satisfy the requirements of high capacity and high energy density [46-47]. Still, it is a standard component of most commercial Li-ion batteries. The other cathodes like $LiMn_2O_4$, $LiFePO_4$, vanadium oxide are also being employed in modern LIBs [48].

1.4.3 Electrolyte

The electrolyte is a component of a lithium-ion battery that serves as the medium for the conduction of Li-ions and facilitates ion transport between the cathode and anode. An ideal electrolyte must satisfy several requirements, like high ionic conductivity, negligible electronic conductivity, wide electrochemical stability window, chemical compatibility with electrode materials, thermal stability, and mechanical integrity [49]. In general, the electrolytes come in three different forms: liquid, solid, and polymeric. Liquid and polymer electrolytes are the most commonly used electrolytes in LIBs. The primary component of liquid electrolytes is a lithium salt dissolved in an organic solvent. Organic solvents used in electrolytes include ethylene carbonate, dimethyl carbonate, and diethyl carbonate. The most common electrolyte in commercial LIBs is $LiPF_6$ salt distributed in ethylene and dimethyl carbonates [49-51].

Liquid electrolytes have a significant drawback in rechargeable batteries that use the lithium metal as anodes. Uneven lithium deposition in a liquid electrolyte environment promotes dendritic growth, despite of lithium metal having the lowest reduction potential and a very high theoretical capacity (~3000 mAh g^{-1}). Hence, the penetration of these dendrites to the separator may result in short circuits and thermal runaway [12-14]. Consequently, the practical implementation of lithium metal batteries is severely limited by safety considerations related to liquid electrolytes. Solid-state electrolytes (SSEs) have become a viable solution to overcome these restrictions [15-18]. SSEs improve thermal stability and lower leakage hazards by substituting a solid ion-conducting

medium for a liquid electrolyte. Therefore the, lithium metal anode integration can be made safer by using solid electrolytes that may offer better mechanical resistance to dendritic penetration.

1.4.4 Separator

The separator, combined with a liquid electrolyte permits the Li-ion flow while limiting electron flow between the anode and cathode. Separators are crucial in keeping the two electrodes apart while allowing Li-ions to move through the electrolyte. The separator is not involved in the electrochemical reactions taking place inside the battery and is not necessary for batteries with solid or polymer electrolytes. In LIBs, a microporous polymer sheet is typically employed as a separator. Electrochemical stability, surface wettability, thickness <25 μm, pore size <1 μm, porosity (40–60%), mechanical integrity, etc., are the fundamental requirements for a separator. Polyethylene (PE), polypropylene (PP), polyethylene terephthalate (PET), and other polymers has been used as microporous separators in LIBs [52-53]. All components of LIBs play a crucial role in determining the battery's overall performance as well as its cyclability. The performance of LIBs encompasses many aspects such as energy density, charge/discharge rates, and thermal stability, that are influenced by these components.

The primary focus in this research investigation is specifically on solid-state electrolyte materials for LIBs. Electrolyte materials are a critical component in the battery's architecture as they govern the Li-ion conduction in the battery, thereby directly influencing the ionic conductivity of the total battery system. By comprehensively

studying and optimizing these solid electrolyte materials, the study aims to enhance ionic transport pathways, making them more reliable and effective for all solid-state battery applications. This focus includes exploring new materials, improving existing ones, and understanding the underlying mechanisms that contribute to the performance of the solid-state electrolyte in the LIBs system.

1.5 Types of Electrolyte

1.5.1 Liquid Electrolyte

The most essential ionic conducting medium in traditional Li-ion batteries is a liquid electrolyte. They usually include a lithium salt such as lithium bis(trifluoromethanesulfonyl)imide (LiTFSI), lithium hexafluorophosphate ($LiPF_6$) or lithium perchlorate ($LiClO_4$) dissolved in a blend of organic carbonate solvents such as propylene carbonate (PC), ethylene carbonate (EC), diethyl carbonate (DEC), and dimethyl carbonate (DMC) in a certain ratios [54-55]. These organic solvents promote salt dissociation and effective lithium-ion transport due to their high dielectric constants. The high ionic conductivity of liquid electrolytes (~ 10^{-2} S cm^{-1}) at room temperature allows rapid charge/discharge rates and good rate capability [56-57]. Interfacial resistance decreases due to increased wettability and uniform ion diffusion across the electrode/electrolyte interface. It is possible due to the liquid nature of the electrolyte that guarantees intimate wetting of electrode surfaces and porous separators. Liquid electrolytes have intrinsic thermodynamic and safety constraints as they are unstable against the metal anode and cause dendtric growth, resulting in short-circuiting [12-14].

1.5.2 Solid Electrolyte

To overcome the drawbacks of liquid electrolytes solid electrolytes are employed. Benefits of solid-state electrolyte:

- SSEs have wide range of electrochemical windows. It employs a high-voltage cathode and metallic anode for high-energy-density rechargeable batteries that is useful for various applications [58].
- Overcoming the safety issues in case of liquid electrolyte, particularly in the large-format battery packs used in EVs, where explosions and fires are severe issues [59].
- SSE offers higher operating temperatures, longer cycle life, and longer shelf life. SSE has greater stability than liquid electrolyte [60-61].
- Lithium metal as an anode may be feasible by suppressing the dendrite formation on the metal surface [62].

On the basis of chemical composition, physical structure and conduction mechanisms electrolyte are classified into three types as polymer, ceramic and composite electrolytes.

1.5.3 Classification of solid-state electrolytes

1.5.3.1 Polymer Electrolytes

Li-ion conducting polymer electrolytes have been extensively studied since the discovery of ion transport in poly(ethylene oxide) (PEO) based systems in the 1970s. In these kind of materials, Li salts are dissolved in a polymer matrix (host matrix) and ion

conduction occurs through them with the segmental motion of polymer chains. Among various polymer electrolytes, PEO remains the most studied polymer electrolyte due to the presence of the ether oxygen group that supports the solvating ability of the material, facilitating Li-ion conduction and transport. However, its high room temperature crystallinity limits the ionic conductivity (~10^{-5} S cm^{-1}), restricting its broad range applications [63]. Various other polymeric electrolytes had also been developed such as polyacrylonitrile (PAN) [64], polymethyl methacrylate (PMMA) [65], polypropylene carbonate (PPC) [66], polyvinyl chloride (PVC) [67], polyvinylidene fluoride (PVDF) [68], and its copolymer PVDF-HFP [69]. Polymer electrolytes do not have serious interfacial problems [71] and offer good mechanical properties. The main advantage of polymer electrolytes over the traditional inorganic electrolyte system is their soft nature that ensures the maximum interfacial contact with cathode and anode. Hence, reducing the interfacial resistance thereby suppressing the interfacial degradation and improving cycling stability. Furthermore, polymer electrolytes exhibit good flexibility and inherent safety. However, they have low room temperature ionic conductivity and variable temperature stability as compare to ceramic electrolyte/ hybrid polymer electrolyte system [72].

1.5.3.2 Ceramic Electrolytes

Ceramic-based Li-ion solid-state electrolytes materials have attracted significant attention due to their high ionic conductivity (~10^{-4} S cm^{-1}) and good thermal stability compared to the polymer electrolytes as discussed in previous section 1.5.3.1. These

ceramic materials are further classified into several families based on their crystal structures such as Garnet, Lithium Super ionic conductor (LISICON), perovskite, sulphide-type electrolyte materials. Among these LISICON-type structures are based on 3D frameworks that provide interconnected pathways for fast metal-ion migration in these systems providing the high bulk ionic conductivity (~10^{-4}–10^{-3} S cm^{-1}) [73-74]. Hence the, Garnet type electrolytes $Li_7La_3Zr_2O_{12}$ (LLZO) and its daughter variants like $Li_{6.4}La_3Zr_{1.4}Ta_{0.6}O_{12}$ (LLZTO), $Li_{6.75}La_3Zr_{1.75}Nb_{0.25}O_{12}$ (LLZNO) etc. are widely studied owing to their high ionic conductivity (~10^{-3} S cm^{-1}), wide electrochemical window stability (~5 V) and stability with lithium metal anodes [75]. Perovskite-type electrolyte family exhibits good bulk ionic conductivity due to the presence of vacancies at A-site, facilitating fast Li-ion transport. However, poor grain boundary conductivity and instability with Li (reduction of Ti^{4+} to Ti^{3+} while coming in direct contact with Li metal) hinders their practical application [76]. Sulphide-based electrolytes, $Li_{10}GeP_2S_{12}$ (LGPS) and argyrodites or halides like Li_6PS_5X (X=Cl, Br, I) have emerged as the promising candidates due to their exceptionally high ionic conductivity (~10^{-2} S cm^{-1}) that is comparable to that of liquid electrolyte systems, relatively soft mechanically enabling lower interfacial resistance. However, they are chemically instable in ambient conditions and are moisture sensitive leading to harmful (H_2S) gas evolution, these demerits limits the electrochemical usage of these sulphide based electrolytes [77]. The most important advantage of ceramic electrolytes is that they can be compressed into a highly dense crystal and morphological structures via different processing routes that gives them ability to suppress lithium dendritic growth due to their high mechanical modulus and

dense structure, enabling battery safety. Though, these materials indicate poor mechanical properties in terms of brittleness and fragility. The poor interfacial compatibility with electrodes is also another issue [78].

1.5.2.3 Composite/hybrid polymer electrolytes

Composite electrolytes are the advanced version of the solid state electrolyte materials that are developed by the addition of fillers (organic and inorganic) to the polymeric matrices. This overcomes the disadvantages of both polymeric and ceramic electrolytes and enhances the stability interfacial property and conductivity [79]. However, the proper composition management and processing, one can get desired results as they show acceptable ionic conductivity, ideal mechanical strength, extended electrochemical window, improved Li-ion transfer number, low interfacial resistance, and dendrite suppression capability [80].

Based on their role in metal ion transport mechanisms inorganic ceramic fillers are categorized into two types: (i) passive and (ii) active fillers. The passive fillers modifies the polymer structure, interfacial properties that enhances the ionic conductivity indirectly but they are not the ion conducting materials. The passive fillers used so far include Al_2O_3 [81], $LiAlO_2$ [82], TiO_2 [83], SiO_2 [84], Y_2O_3 [85], ZrO_2 [86]. These materials improve ionic conductivity by reducing polymer crystallinity and promotes the dissociation of Li salts through surface interactions.

In contrast, the active fillers are Li-ion conducting materials directly participating in ion transport, including the ceramic solid electrolyte materials like LISICON-type,

NASICON-type, garnet-type, perovskite-type, sulphide electrolyte based systems [73-77]. When they are incorporated into polymer matrices, active fillers not only improve the overall ionic conductivity but also contribute to the formation of interconnected fast-ion conduction pathways. Hence, enhance the transference number and reduce the concentration polarization during battery operation. Despite of these advantages that composite electrolyte possess some challenges remains in achieving uniform distribution of the fillers, controlling filler/polymer interfacial interactions, and optimizing the filler concentration to get the optimum ionic conductivity and mechanical integrity. Figure 1.3 shows the various types of electrolytes and their classification.

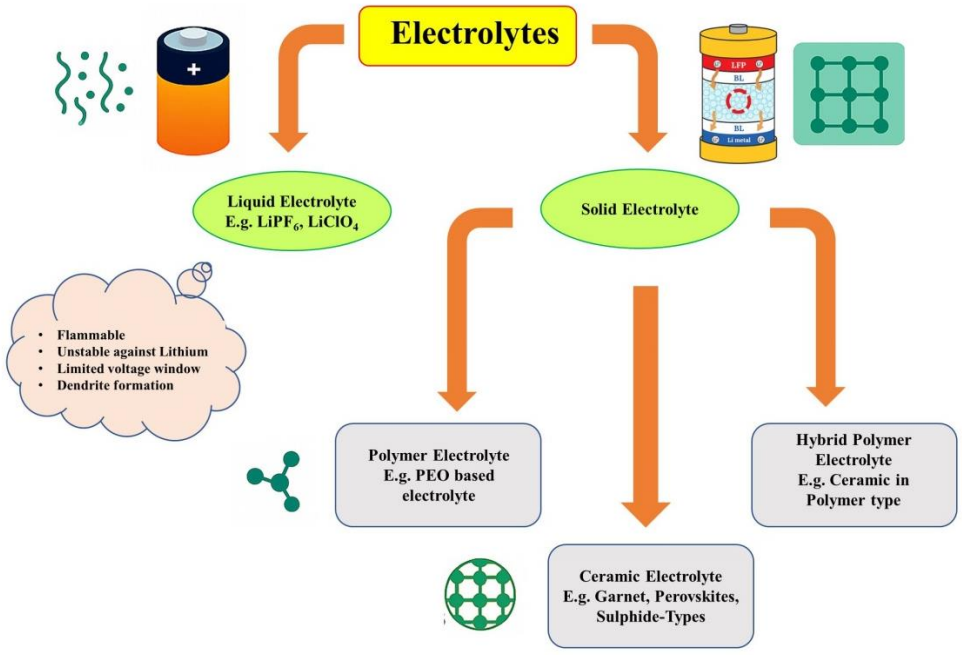

Figure 1.3: Schematic representation of the classification of electrolyte material used in LIBs.

1.6 Material Investigated:

Ceramic electrolytes exhibit superior mechanical strength, electrochemical performance, and thermal stability. Hence, it becomes a more attractive substitute for traditional liquid electrolytes. The necessity to overcome the safety, stability, and energy density constraints inherent in liquid-based lithium-ion battery systems is the primary driver behind the shift toward ceramic electrolytes. Figure 1.4 shows the qualities possessed by a ceramic solid-state electrolyte.

Figure 1.4: Representation of the number of qualities possessed by a ceramic solid state electrolyte.

1.6.1 Oxide and Phosphate based ceramic electrolyte

After the literature review and scope of investigation oxide based LLZO and phosphate based LTPO and their composites has been considered for rigorous investigation for this research work.

1.6.1.1 $Li_7La_3Zr_2O_{12}$

Garnet structure solid electrolyte is a promising electrolyte material for Li ion batteries. Garnet electrolytes exhibit the general chemical formula of $A_3B_2(XO_4)_3$, where A is an eight-fold coordinated site, X is a tetrahedral coordinated site, and B is an octahedral site, showing an FCC structure with space group Ia-3d space group [88]. In the year 2003, Thangadurai et al. developed garnet-type Li oxide with the generalized chemical formula $Li_5La_3M_2O_{12}$, M = Nb, Ta. It has ionic conductivity approximately 10^{-6} S cm^{-1} at room temperature [89].

Murugan et al. synthesized the $Li_7La_3Zr_2O_{12}$(LLZO) with a highly conductive cubic phase of garnet structure[90]. A less conductive tetragonal phase was synthesized by Awaka et al. in 2009 [91]. The primary difference between the two structures is Li-ion occupancy. In tetragonal garnet, 3 lithium sites are present, which occupy (8a) tetrahedral site, (16f) octahedral sites, and (32g) octahedral site. In cubic phase of LLZO, two types of Li sites are present: (24d) tetrahedral site and (96h) distorted octahedral site. In the cubic LLZO, the Li-Li bond length is short, which results in high ionic conductivity [92].

Advantages of the LLZO solid electrolyte among all garnet-type:

- It has reasonable ionic conductivity (~10^{-4} S cm^{-1}) [93-94].
- Highly stable against metallic lithium, which allows us to use lithium as an anode in an all-solid-state battery [95].
- Wide electrochemical window (~5V), leads to the use of high-voltage cathode for high-energy-density application [96-97].
- High thermal and mechanical strength.

1.6.1.2 $LiTa_2PO_8$

$LiTa_2PO_8$ (LTPO) is a solid electrolyte based on phosphate that has a strong polyanionic framework and a monoclinic crystal structure [33]. While lithium ions move through interconnected channels inside the lattice, PO_4 tetrahedra help to maintain structural stability and thermal robustness. The advantages of the LTPO solid electrolyte are:

- Structural and high-density.
- High ionic conductivity.
- Atmospheric stability.
- Tunable lattice through aliovalent substitution.
- Potential role as sintering additive in composite systems.

1.7 Motivation of current Research

The practical implementation of high-performance ceramic electrolytes for lithium-ion batteries is still limited by issues like interfacial instability with lithium metal,

incomplete densification, grain-boundary resistance, and lithium volatilization during sintering. Despite of the strong bulk ionic conductivity and chemical stability of garnet-type LLZO, the overall performance is constrained by the predominance of grain-boundary impedance and the emergence of secondary phases. Similarly, the phosphate-based electrolyte such as LTPO provide structurally sound frameworks. There is still a lack of systematic knowledge regarding the interplay between ionic transport, dopant incorporation, and structural heterogeneity.

In order to improve densification, decrease grain-boundary resistance, and increase interfacial stability, the current study focuses on optimizing oxide and phosphate-based ceramic electrolytes through doping, step-sintering techniques, and composite design. The goal of the current reasearch work is to clearly correlate microstructure and ionic transport behavior by combining structural analysis, impedance deconvolution, and electrochemical validation.

1.8 Objective of the Thesis

This study aims to synthesize solid electrolytes as an alternate to existing liquid electrolytes for rechargeable Li-ion batteries. Hence, the following are the objectives of the present investigation:

1. Synthesis and physiochemical characterizations of ceramics (oxides/ phosphates) solid state electrolyte/s for rechargeable solid-state batteries.

2. Improvement in the ionic conductivity through doping/substitution of transition/inner-transition elements in the synthesized solid-state electrolyte/s.
3. Investigation of Dielectric responses of developed solid-state electrolytic material/s.
4. Investigation of the electrochemical performance, such as GCD, EIS, cyclic performance, etc., of developed solid-state electrolytic material/s.

Chapter 2

Experimental and Characterization Techniques

This chapter focuses on the solid-state reaction route for synthesizing ceramic-based solid-state electrolytes, along with their relevant structural, morphological, electrical, and electrochemical characterization techniques.

2.1 Synthesis Technique

This section deals with the details of the synthesis techniques used to synthesize the ceramic and composite ceramic materials in this study. The specific techniques and precursor materials utilized for synthesis are: outlined below.

2.1.1 Solid State Route

Solid state method using a ball mill is a prevalent choice in both academic research, industrial, and development laboratories (R&D). Cost efficiency and simplicity make it suitable for synthesizing various materials in bulk amounts for various applications, resulting its widespread adoption. This method involves mixing and grinding of precursors over a specified period to ensure thorough blending and synthesis of the final compound. Thereafter, the prepared mixed product undergoes calcination to yield the desired solid-state electrolyte materials. $LiTa_2PO_8$, $Li_{1+x}Ta_{2-x}Zr_xPO_8$, $Li_7La_3Zr_{2-x}Ce_xO_{12}$, LTZPO@LLZCO composite were synthesized using a solid-state route. All chemicals utilized in this research were of high purity (98% to 99.9%) and analytical grade.

2.1.1.1 Preparation of $LiTa_2PO_8$ ceramic

LTPO was synthesized using a solid-state reaction route. All precursors (Li_2CO_3, Ta_2O_5, and $(NH_4)H_2PO_4$), each with purity greater than 99% were dried in an oven at 100 ºC overnight to remove residual moisture in the oven to remove moisture. A scheme of the synthesis of LTPO is shown in Figure 1. The raw powder was prepared via ball milling of all the precursors in a zirconia jar. The raw powder was then calcined for 12 hours at

temperature ranging from 800 ºC to 1050 ºC in a box furnace, followed by pressing into pellets using a hydraulic press. The pellets were placed in a furnace for the step sintering process, starting with heating a pellet at 1100 ºC for 2 hours and heating at a lower temperature of 1050 ºC for 2, 4, 6, and 8 hours. Samples are marked as T1, T2, T3, T4, T5, respectively. Schematic representation of the synthesis of LTPO is shown in Fig. 2.1.

Figure 2.5 Schematic representation of the synthesis of LTPO

2.1.1.2 Preparation of $Li_{1+x}Ta_{2-x}Zr_xPO_8$ ceramic

Zirconium-doped lithium tantalum phosphate $Li_{1+x}Ta_{2-x}Zr_xPO_8$ (LTZPO) solid electrolyte was synthesized via a conventional solid-state reaction route. Li_2CO_3, Ta_2O_5, ZrO_2, and $(NH_4)H_2PO_4$ were used as starting precursors. Stoichiometric amounts of the precursors were weighed according to the required compositions and thoroughly mixed by planetary ball milling using a zirconia jar in isopropanol medium for 24 h to ensure

homogeneous mixing. The as-milled powders were dried and subsequently calcined at 1050 °C for 12 h in air. The calcined powder was then pressed into pellets using a hydraulic press. The pellets were sintered at 1050 °C for 12 h. The concentration of Zr in LTPO is increased gradually with the general formula of $Li_{1+x}Ta_{2-x}Zr_xPO_8$ (x= 0, 0.1, 0.2, 0.3), and samples are marked as LTPO, LTZPO-0.1, LTZPO-0.2, LTZPO-0.3.

2.1.1.3 Preparation of $Li_7La_3Zr_{2-x}Ce_xO_{12}$ ceramic

$Li_7La_3Zr_{2-x}Ce_xO_{12}$ was synthesized via a conventional solid-state reaction route. Starting precursors are Li_2CO_3, CeO_2, ZrO_2, and La_2O_3. The dried precursors were ball-milled in a zirconia jar using ethanol as the milling medium to ensure homogeneous mixing. The milled powder was calcined at 900 °C for 10 hours. The concentration of Ce in LLZO is increased gradually at a step size of 0.125, making makes a general formula of $Li_7La_3Zr_{2-x}Ce_xO_{12}$ (x = 0,0.125, 0.25, 0.75, 0.5) and samples are marked as T1, T2, T3, T4, T5 with increasing concentration. The resulting calcined powder was then uniaxially pressed into pellets. Pellets are subjected to sintering as per two schedules; (i) Schedule-1, an initial temperature at 1150 °C for 2 hours followed by holding at 1100 °C for 2, 4, 6, 8 hours and sample are coded as Q1, Q2, Q3, Q4, and 1100 °C for 0.16 (10 mins) hour with sample coding as Q5 respectively and (ii) Schedule-2 with initial temperature at 1200 °C for 2 hours followed by holding at 1170 °C for 0, 2, 4, 6, 8 hours with sample ID as Q6, Q7, Q8, Q9, Q10, respectively. Schematic representation of the synthesis of LLZCO is shown in Fig. 2.2.

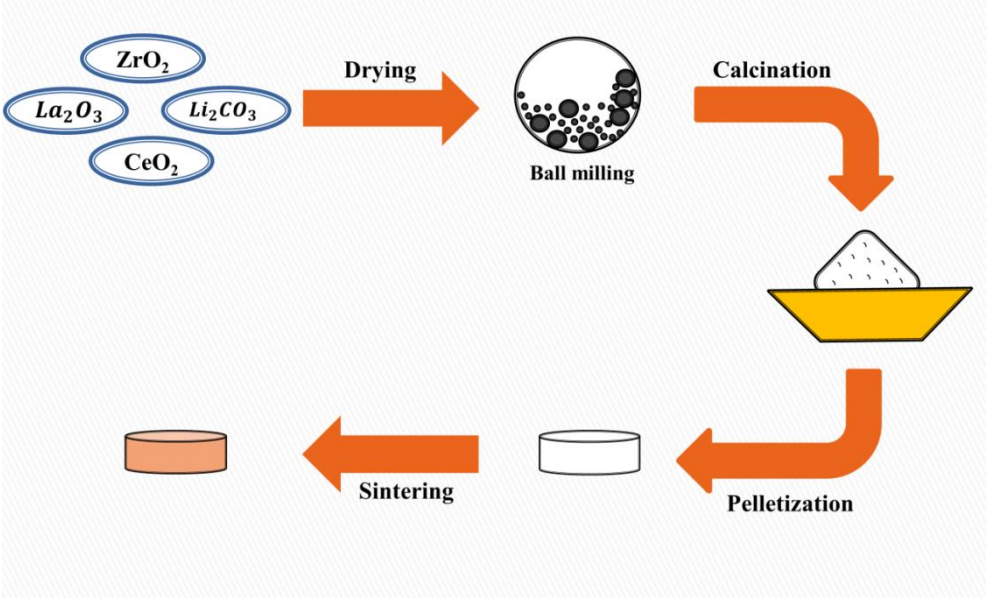

Figure 2.2 Schematic representation of the synthesis of LLZCO

2.1.1.4 Preparation of LLZCO@LTZPO composite

Crystalline $Li_{1.1}Ta_{1.9}Zr_{0.1}PO_8$ and $Li_7La_3Zr_{1.75}Ce_{0.25}O_{12}$ were mixed according to weight percentage of 0%, 5%, 10%, 15%, 20%, 25%, of LTZPO in LLZCO and then pressed into a pellet and sintered at 800 ºC for 12 hours in argon/N_2 environment. Composite samples with varying weight percentage from 0%, 5%, 10%, 15%, 20%, 25% are marked as C0, C1, C2, C3, C4, and C5 respectively.

2.2 Pellet Formation and Finishing

After calcination, the obtained powder was re-ground with a pestle and mortar, and then the homogeneous powder was passed through a fine mesh sieve to obtain the approximately constant particle size distribution prior to pelletization. The homogeneous powder was then processed into pellets with a diameter of ~10-13 mm and a thickness of

~1 mm with polyvinyl alcohol as a binder using a conventional uniaxial pressing technique via a hydraulic press maintained at 2 ton pressure. After sintering, these pellets were polished with SiC abrasive paper with different grit sizes (400, 800, 1200, 1600, and 2000 grit) to obtain fine, smooth, and parallel surfaces. Before any characterization, these pellets were ultrasonically cleaned in ethanol medium and dried at 100 °C.

2.3 Density Measurement

The relative density of sintered pellets was measured using both the theoretical density of the material and experimental bulk density measured using Archimedes' principle. Theoretical density of the material is calculated using ~~the~~ Equation 2.1

$$\rho(theo.) = \frac{n \times M}{N \times V} \tag{2.1}$$

24 Where ρ(theo), n, M, N, V are theoretical density, number of formula units per unit cell, molecular weight, Avogadro number, and volume of unit cell, respectively. Bulk density of the material is calculated using Archimedes' method using equation (2.2),

$$d = \frac{m_a . d_e}{m_a - m_e} \tag{2.2}$$

Where d is the density of the sample, m_a is the mass of the sample in air, d_e is the density of ethanol, and m_e is the mass of the sample in ethanol.

2.4 Characterization Techniques

To analyze the various properties of the materials before and after the synthesis, multiple characterization techniques are employed to study the structural, morphological, surface, electrical, and electrochemical characteristics. This section provides an introduction, operational principles, and an overview of these characterization methods.

2.4.1 Thermal Characterization

2.4.1.1 Thermogravimetric Analysis (TGA) and Differential Scanning Calorimetry (DSC)

Thermogravimetric analysis (TGA) and Differential Scanning Calorimetry (DSC) are thermal characterization techniques used to evaluate the chemical stability and thermal behaviour of materials during both heating and cooling.

TGA provides valuable insights into how the mass of a material changes with temperature and time, enabling the study of physical properties, such as adsorption, phase transitions, decomposition temperature, purity, and absorption, as well as chemical processess including oxidation, reduction, and decomposition.

In contrast, DSC monitors the temperature difference between the reference sample and the material. This technique offers insights into exothermic or endothermic reactions, thereby revealing the crystallization, glass transition, melting, and sublimation points of materials. The combined TGA-DSC studies provide the stable framework for determining the optimal synthesis temperature, sintering conditions and crystal structure stability conditions.

In this study, a PerkinElmer TGA analyzer Model: TGA 4000 was used for TGA and DSC analysis, with the heating rate of 10 ºC/min, with a maximum temperature of 1200º C for all samples.

2.4.2 Structural and Morphological Characterization

2.4.2.1 X-ray Diffraction (XRD)

XRD is a reliable characterization used for the crystal structure analysis of crystalline and amorphous solids. XRD was carried out using RIGAKU make ULTIMA IV, employing Cu $K_{\alpha 1}$ as incident radiation with a wavelength of 1.540 Å in conjunction with Ni filters to filter out the wanted radiation, and the data were collected in the range of 10-70° with a 0.02° step size. The scattered radiation interferes constructively or destructively in a specific direction., Analysis of the pattern 'd' spacing, lattice structure, and arrangement of atoms can be elucidated. Rietveld refinement has been employed to analyze the lattice constant and the structural parameters of the material using 'X'pert HighScore plus software. These reflections are governed by Bragg's law as follows:

$$n\lambda = 2d \sin\theta \tag{2.3}$$

where "θ" denotes the angle of incidence, "d" signifies the lattice spacing, "λ" stands for the wavelength of the X-rays, and "n" represents the order of the reflecting plane. Considering ceramic solid state electrolytes as an imperfect finite crystal with crystallite size equals to or less than 1 µm, the average crystallite size of materials is calculated using, Scherrer's formula using the particle size peak broadening given by equation (2.4). Compressive or tensile microstrain induced in the crystal structure during the

calcination or sintering process is calculated via the Williamson-Hall (W-H) plot using the total peak broadening of particular XRD peaks governed by the equation (2.5).

$$D = \frac{K\lambda}{\beta Cos\theta} \qquad (2.4)$$

$$\beta_t = \frac{K\lambda}{DCos\theta} + 4\varepsilon tan\theta \qquad (2.5)$$

βt(radians), β(radians), ε, D, and K are the total peak broadening, full width at half maxima, micro-strain, crystallite size, and shape factor (0.9), respectively. Figure 2.3 shows the schematic representation of Bragg's law.

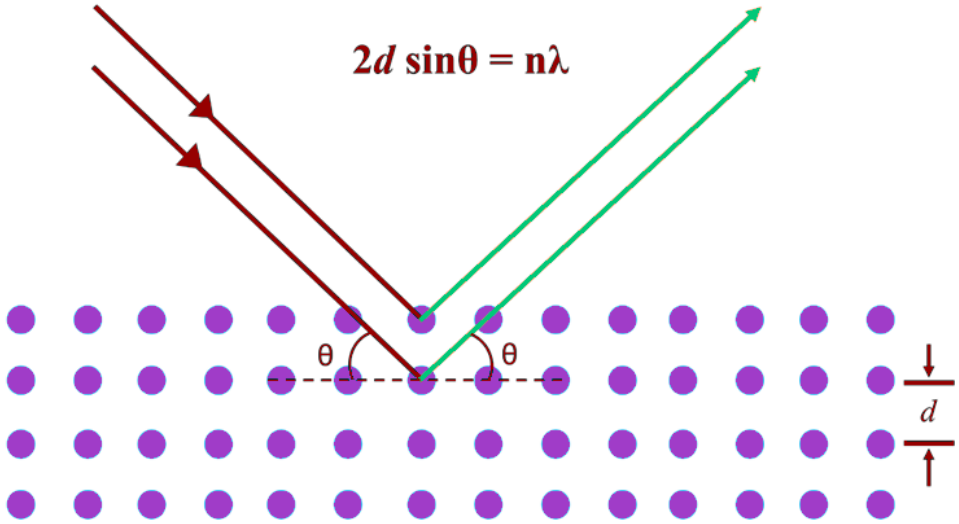

Figure 2.3 Schematic of X-ray diffraction using Bragg's law

23

2.4.2.2 Scanning Electron Microscopy (SEM)

A scanning electron microscope (SEM) is a surface characterization technique which that uses an electron beam to scan the surface of a sample/material and generates the

microstructural image of the specimen. Interactions between the incident electron and the atoms in the sample produce multiple observable signals that unveil the details about the specimen's composition and surface texture. These signals offer valuable observations about the sample's morphology and chemical composition. Generally, a 2-D image of a selected portion is constructed to depict a spatial view. In this study, the FEI model 'Quanta 200F' scanning electron microscope was used for the SEM analysis of the synthesized specimens using the electron gun working at an acceleration voltage of 15 KV at 40 nA probe current with the working distance of 10 mm. The average grain size of the synthesized samples was determined using "ImageJ software".

2.4.2.3 Transmission Electron Microscopy (TEM)

The transmission electron microscopy (TEM) technique is employed to examine the size, morphology, and shape of materials at higher magnifications higher than those achievable with SEM. TEM comprises a high-energy, high-voltage electron beam incident on the sample surface. TEM uses a transmitted beam of electrons through the material to create an image. The sample is prepared by making its suspension and coating it onto the grid in the form of a film with an approximate thickness of 10 μm. A fluorescent screen coupled to a charge-coupled device is employed to focus and magnify the resulting image.

In this study, the FEI make model 'FEI Tecnai G220 s-Twin' TEM machine operated at 300 KV was used to examine the synthesized samples using carbon-coated grids (CF200-Cu).

2.4.2.4 Energy-Dispersive X-ray Spectroscopy (EDX)

Quantitative analysis of various elements present in synthesized materials was done using Energy-Dispersive X-ray Spectroscopy (EDX). Generally, EDX is integrated with SEM or TEM microscopes. EDX functions by incidenting a high-energy electron beam on the specimen that energizes the atoms of the specimen, resulting in the excitation and ejection of inner shell electrons. Corresponding to this action, outer shell's electrons fill the vacancy of the ejected electron, thus emitting the characteristic X-rays. These characteristic X-rays facilitate element identification as they are specific to the atomic structure of the element. In this study, EDX results are coupled with SEM and TEM microscopy analysis. Figure 2.4 shows the representation of SEM, TEM, and EDX during sample analysis.

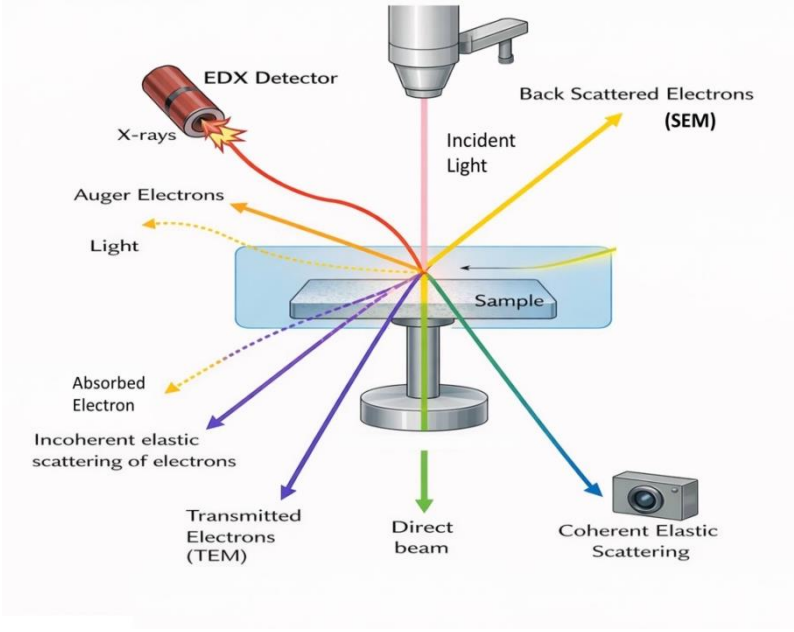

Figure 2.4 Representation of SEM, TEM and EDX during sample analysis

2.4.2.5 Atomic Force Microscopy

In the present study, surface roughness analysis of Ce-doped Li7La3Zr2O12 sample at micron and sub-micron range before and after Al coating was carried out using the Park make model XE 100 Atomic Force Microscope(AFM). AFM images were analysed using the SPM Lab software. The measuring probe of AFM comprises a gold-coated Si tip supported by a cantilever beam, and the tip was kept at 21.04 nm. AFM data was collected in non-contact mode with a scan rate of 2Hz.

2.4.3 Dielectric and Impedance Characterization

2.4.3.1 Dielectric Spectroscopy

Dielectric Spectroscopy was employed to investigate the frequency-dependent electrical and polarization behavior of the synthesized materials in the frequency range of 8-1 MHz to 4 Hz. To facilitate measurements, sintered pellets were coated with Au on both sides thereby ensuring electrically conductivity and establishing a parallel-plate capacitor configuration. The dielectric response is based on the concept of energy storage and the relaxation that occurs when each component of the system releases its stored energy. Dielectric measurements provide valuable insights into the temperature and frequency dependence of the relaxation mechanism within the material. It offers details on two crucial physical characteristics: (a) dielectric constant, and (b) dielectric loss.

The charge carriers generate heat when an alternating field is applied due to a lag in polarization known as dielectric loss. Temperature, frequency, orientation, pressure, and material molecular structure all affect the total dielectric constant of a material. The total dielectric constant, also known as electric permittivity (ε*), is computed using the

following formulas given in equations (11-14), which yield its real (ε′) and imaginary (ε″) dielectric components with dielectric loss tangent (D):

$$\varepsilon^* = \varepsilon' - j\varepsilon'' \tag{2.6}$$

$$\varepsilon' = |\varepsilon^*| cos\delta = |\varepsilon^*| sin\theta \tag{2.7}$$

$$\varepsilon'' = |\varepsilon^*| sin\delta = |\varepsilon^*| cos\theta \tag{2.8}$$

$$D = tan\delta = \frac{\varepsilon''}{\varepsilon'} \tag{2.9}$$

Where δ = (90°-θ), θ represents the phase difference between the measured current and the applied alternating voltage. Taking into account how temperature affects dielectric materials, at higher temperatures charge carriers, successfully hop in the direction of the applied field to create a piling up of charges towards a high energy barrier side from the lower energy barrier side, which results in the stacking up of charges, correspondingly leading to an increase in polarisation and permittivity. The relaxation behaviour within the material, triggered by thermal processes, is evidenced by the shift of the loss peak towards higher temperatures. The peak's maxima position met the requirement ωτ = 1, where ω = 2πf, described as angular frequency, and τ denotes the charge carriers' relaxation time. The activation energy of relaxation time can be calculated using the Arrhenius equation given by the equation.

$$\tau = \tau_0 e^{E_r / K_b T} \tag{2.10}$$

In this case, E_r is the activation energy of relaxation, and τ_o is the characteristic relaxation time of the order of the atom's vibrational period. In the present study, dielectric spectroscopy was done using the HIOKI MAKE IM 3536 LCR METER at the perturbation voltage of 100 mV.

The electrical conduction in an a material placed in an alternating field arises from the free and bound charge carriers present in the material. The frequency response of the conductivity justifies the contribution of the charge carriers, respectively. Decrement in the conductivity with increasing frequency corresponds to the dominance of free charge contribution in the total conductivity, whereas increment in it justifies the dominance of bound charge carrier contribution. The AC field across the parallel plate capacitor with material as a dielectric inside it induces the charge carrier to hop from one defect state to another in the crystal structure. The conductivity is governed by the relation

$$\sigma = \omega \varepsilon_0 \varepsilon' \tan \delta \tag{2.11}$$

Frequency dependence of ac conductivity is fitted using Jonscher's power law given in equation (2.12)

$$\sigma = \sigma_{dc} + A\omega^s \tag{2.12}$$

where σ_{dc} is the d.c. contribution which is frequency independent, and $A\omega^s$ is the frequency-dependent factor, the frequency exponent 's' represents the interaction between the mobile ions and lattice, depending on the applied field's frequency and sample temperature. 'A' represents the degree or strength of polarization.

The sort of conduction mechanism used in conductivity is revealed by the temperature dependency of the s parameter as: (a) when s is either slightly increased with temperature or nearly constant about 0.8, the quantum mechanical tunneling is the conduction mechanism followed. (b) when the value of s decreases linearly with an increase in temperature, Correlated Barrier Hopping (CBH) conduction mechanism is followed. (c) When s increases with an increase in temperature Non-overlapping Small Polaron Tunnelling (NSPT) conduction model is used. (d) When s first decreases, then increases with increase in temperature, Over-lapping Large Polaron Tunnelling (OLPT) conduction model is used.

From the well-fitted data activation energy of the DC conductivity is calculated using the Arrhenius equation given in equation (2.13)

$$\sigma_{dc} = \sigma_0 e^{\frac{E_a}{K_b T}} \tag{2.13}$$

Where σ_{dc} is the dc conductivity, σ_o is the pre-exponential factor, E_a is the activation energy, K_b is the Boltzmann constant and T is the temperature of the sample.

2.4.3.2 Impedance Spectroscopy

Complex impedance spectroscopy (CIS) is a powerful analytical method used to investigate the contributions of the relaxation process of various microscopic areas in polycrystalline ceramics, such as the grain, grain boundary, and electrode interface. Impedance includes both resistive and capacitive/inductive parts that can be resolved by placing the sample in an AC potential field (V), shown in equation (2.14)

$$V = V_o exp(i\omega t) \tag{2.14}$$

Where V_o is the amplitude and ω is the angular frequency. The sinusoidal current response to the input illustrates the phase difference between voltage and current, as well as the total complex impedance (Z), which incorporates both the real and imaginary parts. The following equations provide the real Z' and imaginary Z″ parts of complex impedance:

$$Z' = \frac{R1}{[1 + (\omega R1C1)^2]} + \frac{R2}{[1 + (\omega R2C2)^2]} \tag{2.15}$$

$$Z'' = \frac{\omega R1^2 C1}{[1 + (\omega R1C1)^2]} + \frac{\omega R2^2 C2}{[1 + (\omega R2C2)^2]} \tag{2.16}$$

The electrical behaviour of the ceramic is shown by the semi-circular arcs and the size of their intercepts on the real axis. The values of the contributions of the grain boundary and grain resistance are found at the intercept of each semicircle on the real Z' axis. The Maxima of each arc are provided by ω_{max} for every -RC- element and given by equation (2.17):

$$\omega_{max} = 2\pi f_{max} = \frac{1}{RC} = \frac{1}{\tau} \tag{2.17}$$

$$C = CPE^{\frac{1}{n}} * R^{\frac{1-n}{n}} \tag{2.18}$$

Where f_{max} and τ are the intrinsic properties of the RC element, independent of sample geometry. The value of capacitance is calculated using equation (2.18). CPE, R, and n are the values of constant phase element, resistance, and empirical constant, respectively. '1' for an ideal capacitor and '0' for an ideal resistor is the reported value for n, which denotes the divergence from perfect Debye behaviour. The influence of temperature on relaxation time (τ), which is determined by using the relaxation frequency derived from the fitting results of the complex impedance plots as a function of frequency, is shown in Figure 9(a, b). The Arrhenius relation is followed in this plot, given by equation (2.19),

$$\tau = \tau_0 e^{E_a/K_b T} \tag{2.19}$$

Where T is the absolute temperature, E_a is the activation energy of the relaxation process, as determined by the slope of ln τ vs. 1000/T, K_b is the Boltzmann constant, and τ_o is the pre-exponential factor known as the typical relaxation time.

The value of the conductivity calculated using the value of the X intercept of the semicircular arcs is shown in the equation

$$\sigma = \frac{l}{R \times A} \tag{2.20}$$

Here σ is the conductivity, R is the resistance, l is the thickness, and A is the area of the pellet.

Impedance spectroscopy offers a powerful method to probe ionic transport across bulk and grain boundaries, but traditional equivalent circuit fitting often conflates overlapping processes and limits its interpretive power. The Distribution of Relaxation Times (DRT)

approach addresses this limitation by deconvoluting impedance data into distinct relaxation processes. Each process includes a specific characteristic time constant and resistance contribution, thereby providing a physically meaningful analysis of ionic transport pathways. DRT enables direct assignment of bulk conduction, grain boundary resistance, space-charge layer impedance, and electrode-interface polarization, offering critical insight into how microstructural heterogeneity translates into electrochemical performance. The area under the curve of the DRT peak gives a more accurate value of the resistance regarding that particular process. The DRT equation is described in the equation (2.16).

$$Z(\omega) = R_{\infty} + \int_{0}^{\infty} \frac{\gamma(\tau)}{1 + j\omega\tau} dln\tau \tag{2.21}$$

Where Z(ω) is the complex impedance at the particular frequency, R_{∞} is the high-frequency ohmic resistance, the γ(τ) is the distribution of relaxation times function.

2.5 Electrical Characterizations

2.5.1 Chronoamperometry

Electrical conductivity is the crucial parameter that defines the performance of any electrolyte material for rechargeable batteries. The chronoamperometry curve of the Au-coated pellet is used to calculate the electronic conductivity of the electrolyte using equation (2.22):

$$\sigma_e = \frac{I_{SS} \times L}{V \times A} \quad (2.22)$$

Here, σ_e, I_{SS}, L, V, and A stand for electronic conductivity, steady state current, pellet thickness, polarisation voltage, and pellet area, respectively. Biologic make VMP3 potentiostat is used for chronoamperometry with the applied voltage of 100 mV for 2 hours.

Electrochemical Characterization

2.6.1 Electrode Preparation

For electrochemical investigations, the cathode ($LiFePO_4$) materials were mixed with conductive carbon (Super P) and polyvinylidene difluoride (PVDF: binder) in a weight ratio of 80:10:10 in *N*-methyl-2-pyrrolidinone (NMP) solvent. The resulting slurry was then spread on a thin Al sheet working as a current collector using the automatic coating unit. After drying, the electrode sheet was pressed between two rollers to improve the contact between active material and current collector while decreasing the roughness of the sheet, and then the circular electrodes of 16-6 mm diameter were punched out from the coated sheet. The schematic diagram for slurry and electrode preparation has been shown in Fig. 2.5.

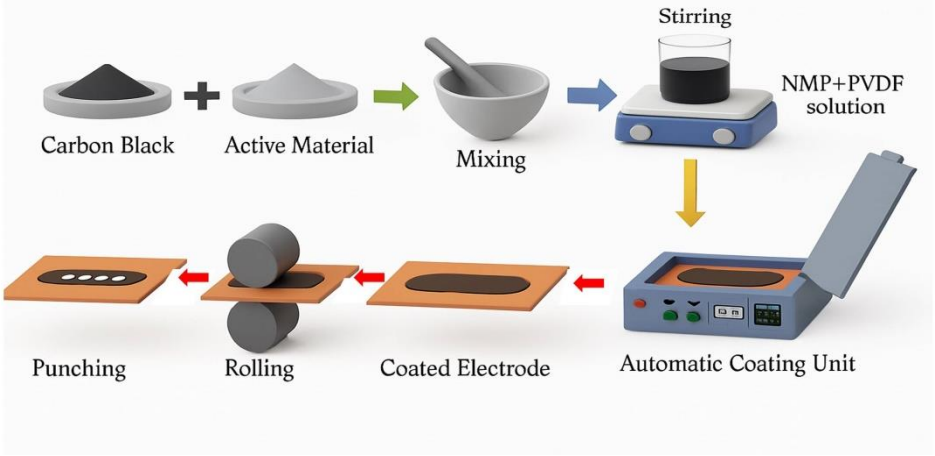

Figure 2.5 Schematic for the slurry and electrode preparation.

2.6.2 Electrochemical Cell Fabrication and Analysis

2.6.2.1 Interlayer Deposition

Polished pellets were attached to the sample holder inside the glove box and then transferred to the HINDHI Make thermal evaporation unit for Al layer deposition at 30 A current for varying time until the desired thickness of Al coating is reached (~30nm). This process is repeated to coat the Al layer on the other side of the pellet for symmetric cell formation. A similar process was employed to make the symmetric cell with non-polarisable Au electrodes for ionic conductivity testing.

2.6.2.2 Electrochemical Cell Fabrication

A symmetric cell (Li|Electrolyte|Li) with or without a metallic Al interlayer and $LiPF_6$ liquid electrolyte layer is assembled. Al-coated pellets are placed in the glove box. Then, Li chips are placed on both sides of the ceramic electrolyte. This assembly is placed

inside the lithium melting unit (Lab-designed) and heated up to 200 °C for metal (Al)-Li alloy formation. After cooling, Li|Al|Electrolyte|Al|Li is packed in a coin cell and Full cell configuration (Li metal battery) using $LiFePO_4$ (LFP) as a cathode, and Li metal as an anode (LFP|Electrolyte|Li) was fabricated in a CR2032 coin cell assembly. All the processing of coin cell fabrication is done inside the MBraun make Ar-filled Glove Box workstation (O_2, H_2O < 0.5ppm). A schematic representation of coin cell assembly is shown in Figure 2.6.

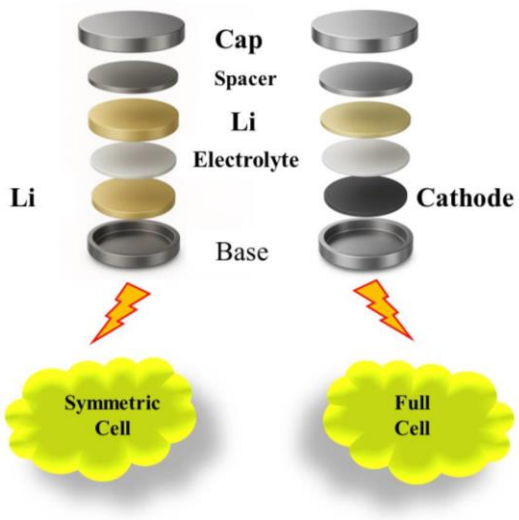

Figure 2.6 Representation of coin cell assembly.

2.6.2.3 Electrochemical Impedance Spectroscopy (EIS)

EIS is used for analyzing the impedance of complex electrochemical systems. This characterization gauges the impedance across a spectrum of frequencies, relying on the frequency-dependent nature of electrochemical cell impedance. EIS data is expressed as

a combination of real and imaginary parts. Plotting the real part on x-axis and imaginary part on the y-axis yields the phaser diagram known as the Nyquist plot. The Nyquist plot is interpreted on the basis of equivalent electrical circuits that provide the kinetic behavior and diffusion parameters within an electrochemical system. In this present work, the electrochemical impedance of symmetric and full cells has been measured in the frequency range of 1 MHz to 100 mHz using the Biologic VMP3 potentiostat.

2.6.2.4 Galvanostatic Charge-Discharge (GCD)

Lithium ion stripping/plating process in lithium symmetric cell (Li|Electrolyte|Li) has been studied to study the stability of lithium ion dynamics, critical current density, and evolution of resistance during long-term cyclability. Symmetric cells are subjected to galvanostatic charge and discharge at a constant current density of 100 uA cm^{-2} with 1-hour hold for each step to calculate the value of overpotential after several cycles. GCD profile of full cell (LFP|Electrolyte|Li) has been studied using LFP as a working electrode and Li as reference and counter to elucidate the specific charge/discharge capacity, coulombic efficiency, and capacity retention during cycling. Symmetric and full cells are tested using a VMP3 multichannel potentiostat supplied by Biologic and Neware Battery Testing System.

Chapter 3

Structural Heterogeneity and Ionic Transport in $LiTa_2PO_8$ Solid State Electrolyte

This chapter examines the synthesis, structural evolution, and ionic transport behavior of $LiTa_2PO_8$ (LTPO) solid-state electrolytes synthesized via a solid-state reaction route. Yielding dense LTPO with monoclinic structure and minor $LiTaO_3$ secondary phase. Dielectric and impedance studies revealed Maxwell–Wagner relaxation with distinct grain and grain-boundary conduction. Electrochemical performance has been evaluated in solid-state cells.

3.1 Introduction

11 $LiTa_2PO_8$ (LTPO) is a recently developed novel solid electrolyte material that exhibits a total conductivity of 2.5×10^{-4} S cm^{-1} and grain conductivity of 1.6×10^{-3} S cm^{-1} at room temperature [98]. Zhang et. al. found that an extra 20% Li encourages the formation of LTPO crystals after looking into the impact of excessive lithium on the conductivity of LTPO [99]. Huang et al. showed that the conductivity of hot-pressed sintering-prepared LTPO samples was twice as high as conventional sintering and had high stability against moisture, another aqueous environment [100]. Fiaz et al., through theoretical computations, proved that lithium is present at three positions, namely a severely distorted tetrahedron [Li(2)O4], a square planar [Li(3)O4], and a distorted trigonal bipyramid [Li(1)O5]. Li-ion conduction through these structures forms a 2D-honeycomb-like structure possessing very high conductivity along the c-axis with moderate and low conductivity of Li-ion along the b and c axes respectively [101].

5 Complex impedance spectroscopy (CIS) is a non-destructive technique that can correlate the electrical and structural properties of solid electrolytes over a broad frequency range as a function of temperature [102]. Hence, to characterize the electrical processes that are taking place in a system and aid in separating the contributions of electro-active regions such as bulk effects, grain boundaries, interfacial resistance, and electrode polarisation effect [103]. Further, AC electrical conductivity demonstrates that the formation of space charge, dipole reorientation, and charge displacement are all phenomena responsible for the transport of charges inside the solid electrolyte. Under an

AC field, these charge transport processes lead to a variety of polarization mechanisms that generate frequency dispersion or dielectric relaxation in the materials [104]. Therefore, the combination of electrical conductivity analysis and complex impedance may further correlate the electrical characteristics and microstructure of defined solid-state electrolytes.

In this chapter, monoclinic phase LTPO has been synthesized via a solid-state reaction route and sintered using a multi-step sintering technique. The anomalous frequency and temperature response of LTPO solid electrolytes have been investigated to understand the various reasons for different conduction mechanisms occurring at the grain and grain boundary counterparts of the material and electronic conductivity using chronoamperometry. Further, LTPO electrochemical performance as a Li-ion solid-state electrolyte using the protective buffer layer (BF) has been studied in quasi-solid-state batteries.

Synthesis of $LiTa_2PO_8$ ceramics was carried out via a solid-state route as mentioned in Chapter 2, Section 2.1.1.1. Moreover, physiochemical, electrical and electrochemical characterizations of $LiTa_2PO_8$ material are performed, and explained in Chapter 2 Section 2.4-2.5.

3.2 Results and Discussion

3.2.1 Thermo-gravimetric and Differential Scanning Calorimetry (TGA and DSC) Analysis

TGA/DSC and the first derivative of the mass loss curve of ball-milled powder have been carried out from room temperature to 1100 ºC in the air to understand the thermal stability and calcination temperature of the LTPO, as shown in Figure 3.1. TGA and the first derivative of mass loss results show multiple loss stages with increasing temperature initially 3.7% of mass loss in the TGA curve is accompanied by endothermic peaks at ~90 ºC (Point-A) in the DSC curve, and shows the maximum rate of the first stage of mass loss in the first derivative can be attributed to the moisture desorption from the sample. The endothermic peak at ~204 ºC (Point-B) is due to the decomposition of $NH_4H_2PO_4$ into H_3PO_4 shown in equation 3.1 [105], broad peak with maxima at ~346 ºC (Point-C) shows the further transformation of H_3PO_4 into polyphosphates ($H_{n+2}P_nO_n$) as shown in equation 3.2 [106] corresponding to the total mass loss of 4.3% during these reactions. In the last stage (450 ºC- 1100 ºC) with 0.4% weight loss, accompanied by the formation of P_2O_5 from the polyphosphates at ~550 ºC (Point-D), decomposition of Li_2CO_3 and its further reaction with P_2O_5 and Ta_2O_5 to form intermediate products at ~714 ºC and 768 ºC (Point- E, F) shown in equation 3.3-3.7 [107-108] and exo/endothermic peaks at ~950 ºC corresponds to the initiation of final reaction between the products to form the stable crystal structure as minimum mass loss is observed upto 1100 ºC. Since the conventional solid-state method typically requires high temperatures to ensure thorough chemical reactions during calcination and enhanced densification during sintering, ceramics are often processed at temperatures well above the lithium volatilization point. Point-H in the derivative curve shows some fluctuation (~1100 ºC) in the rate of mass loss, which can be considered for the lithium

loss at high temperature and secondary phase formation [109]. Based on the thermal analysis, the calcination temperature for LTPO ceramics can be concluded to lie above ~800°C, ensuring the completion of intermediate reactions and the formation of stable phases. The sintering temperature, however, must be carefully optimized to avoid significant lithium volatilization and dense grain growth, with the ideal range extending up to ~1100°C, where the stable crystal structure is achieved with minimal mass loss.

$$NH_4H_2PO_4 \rightarrow NH_3 + H_3PO_4 \quad (3.1)$$

$$nH_3PO_4 \rightarrow H_{n+2}P_nO_n + (n-1)H_2O \quad (3.2)$$

$$2H_{n+2}P_nO_{3n-1} \rightarrow P_2O_5 + H_{n+2}O \quad (3.3)$$

$$Li_2CO_3 \rightarrow Li_2O + CO_2 \quad (3.4)$$

$$Li_2O + P_2O_5 \rightarrow 2Li_3PO_4 \quad (3.5)$$

$$Li_2O + Ta_2O_5 \rightarrow 2LiTaO_3 \quad (3.6)$$

$$Ta_2O_5 + LiTaO_3 + Li_3PO_4 \rightarrow 2LiTa_2PO_8 \quad (3.7)$$

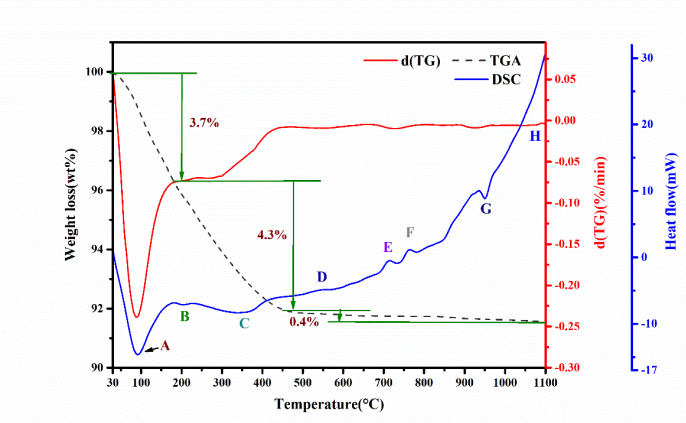

Fig. 3.1 TGA/DSC curve of ball-milled sample of LTPO from RT (30 ºC) to 1100 ºC in an air atmosphere

3.2.2 Structure and Morphological Analysis

3.2.2.1 X-ray Diffraction (XRD) Analysis

Figure 3.2 shows the X-ray diffraction (XRD) pattern of ball-milled powder sample calcined at a different temperature ranging from 800 ºC to 1050 ºC for 12 hours at a temperature difference of 50 ºC for crystal structure formation as analyzed from the TGA/DSC curve shown in the previous section.

The XRD curve shows a crystalline structure at 1050 ºC. Crystal structure formation of LTPO at 1050 °C is driven by the balance between thermodynamic stability and kinetic factors. TGA/DSC curve shows that above 1000 °C, there is no mass loss in the system, and an increase in heat flow shows the probability of stable phase formation. At the optimal temperature, atoms or ions arrange into the most stable crystal phase by minimizing the system's Gibbs free energy. The monoclinic phase with the C2/c space group (ICDD 04–025–5910) is found to match the XRD peaks of LTPO according to the XRD pattern shown in previously reported data [110]. The Rietveld refinement analysis has been performed to get quantitative information on the crystal structure of the sample calcinated at 1050 ºC, as shown in Fig. 3.3. FWHM of sharp and intense XRD peaks is modelled using the Pseudo-Voigt function with reliable refinement parameters (χ^2= 2.48, R_{WP}= 7.56%, R_P= 4.83%) and lattice parameters (a= 9.71 Å, b= 11.52 Å, c= 10.69 Å, α= 90.00^0, β= 90.04^0, γ= 90.00^0, vol.= 1196.88 Å^3). The site occupancies and fractional parameters are shown in Table 3.1. Considering LTPO as an imperfect finite crystal having a crystallite size less than 1 µm range then the average crystallite size of LTPO is

calculated using Scherrer's formula, and it uses particle size peak broadening given by equation 2.4 (chapter 2, section 2.4.2.1). Figure 3.4 shows the Williamson-Hall (W-H) plot used to determine the compressive or tensile microstrain experienced by the crystal using the total peak broadening of XRD peaks as stated in equation 2.5 (chapter 2, section 2.4.2.1). High intense peaks indexed to the planes (111), (021), (200), (112), (202), (130), (221), (222), (223), (042), (330), (225) in XRD pattern of LTPO are used to calculate 'β' for average crystallite size calculation. Broadening in the peaks due to stress originating during calcination is related to residual strain in the system. The micro-strain (ε) is the slope of the fitted plot between 'βcosθ' and '4sinθ'. The average crystallite size calculated from Scherrer's formula and micro-strain in the crystal system from the W-H plots is ~170 nm and -1.04×10^{-4}, respectively. The negative strain from the W-H plot can be attributed to the shrinkage of the crystal structure [111]. It is evident that altering the sintering schedule significantly affects the ionic conductivity, density, and grain structure of ceramics [112]. Herein, in this chapter multistep sintering process has been undertaken to prepare high-density LTPO pellets, this process involves rapidly heating the LTPO pellet to a high temperature (1100 ºC) and holding it there for a short duration (2 hours) then quickly cooled down to a lower temperature (1050 ºC) for longer duration (2, 4, 6, 8, 10 hours). The Archimedes principle, as stated in equation 2.2 (Chapter 2, section 2.3), has been used to calculate the relative density of the LTPO sintered pellet. Table 3.2 shows the relative density of the material sintered at different sintering temperature schedules. From this table, it can be concluded that sample T2 sintered at 1100 ºC for 2 hours and 1050 ºC for 4 hours shows the highest relative

density of 82.4%. Figure 3.5 shows XRD patterns of samples sintered at different step sintering schedules. It can be seen that the pellets have a similar diffraction pattern to that of the LTPO monoclinic phase; however, the secondary phase of $LiTaO_3$ could be observed in the sample sintered for a longer time duration at 1050 ºC.

The formation of the $LiTaO_3$ impurity phase can be attributed to the lithium loss at high sintering temperatures, as indicated by the first derivative curve of mass loss around ~1100 °C. heterogeneous crystal structure of LTPO, a secondary phase formation phenomenon, is commonly reported in LTPO samples during other sintering processes in previous studies [113]. The density of the sample T2 was relatively high compared with the density of the pellets obtained via other step sintering schedules. This phenomenon is thought to be related to the behavior of particles, secondary phase formation, and the extent of lithium losses during sintering.

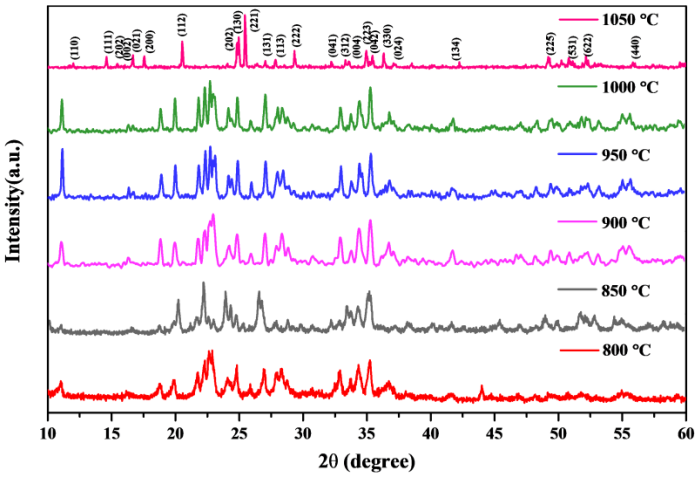

Fig. 3.2 XRD pattern of LTPO synthesized in a range from 800 ºC to 1100 ºC at a temperature step of 50 ºC of the ball milled LTPO sample.

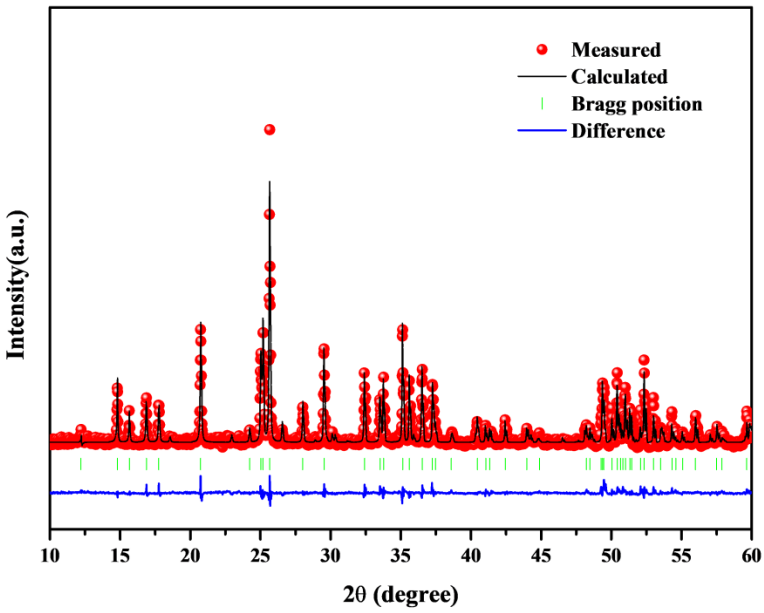

Fig. 3.3 Rietveld refinement of the LTPO sample sintered at 1050 ºC for 12 hours.

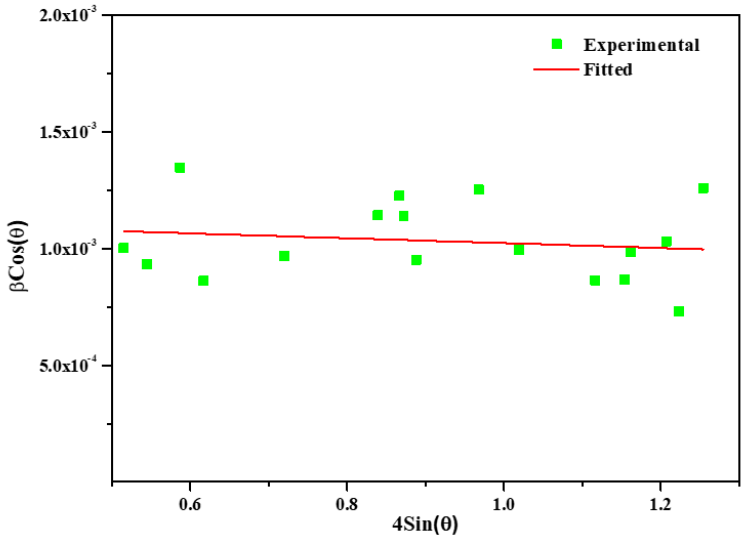

Fig. 3.4. Williamson-Hall plot of the LTPO sample synthesized at 1050 ºC for 12 hours.

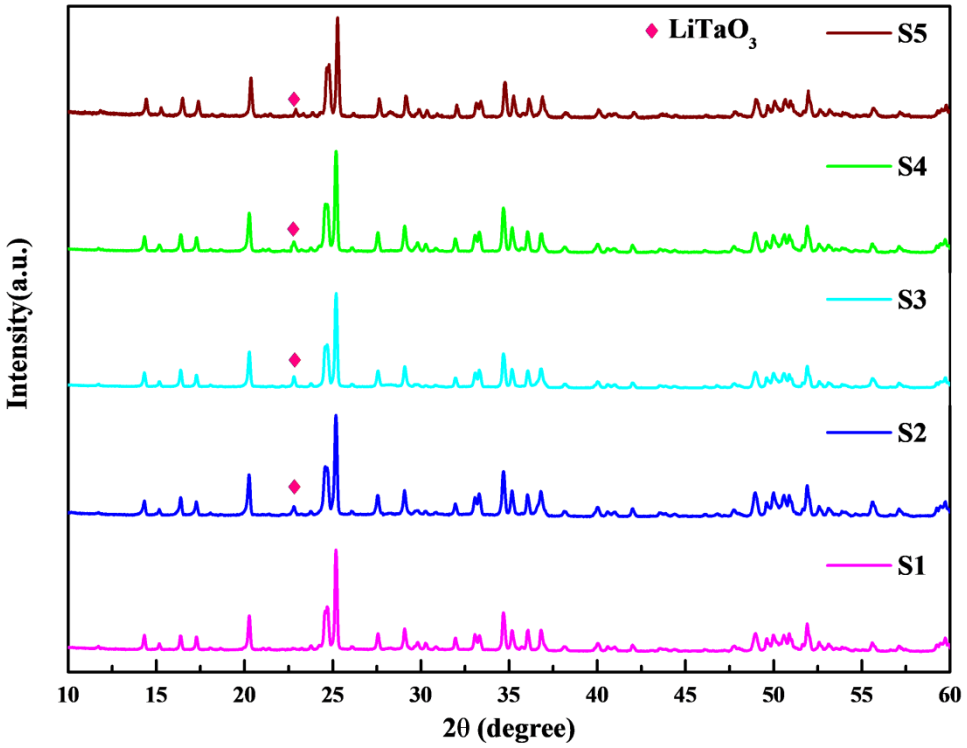

Fig. 3.5 XRD pattern of the LTPO sample calcined at 1050 ºC and further exposed to different sintering temperature schedules (1100 ºC for 2 hours and then holding at lower temperature-1050 ºC for 2, 4, 6, 8, 10 hours respectively for different step sintering schedules) as shown in Table 1 for sintering.

Table 3.1. Rietveld Refinement results of Wyckoff positions and Occupation factor of sample T2 LTPO

Element	x	y	z	Occupancy
Ta1	0.2429	0.0933	0.2452	0.66
Ta2	0.0000	0.3472	0.2500	0.68
Ta3	0.0000	0.0000	0.0000	0.66
P	0.494	0.209	0.047	1.00
O1	0.011	0.371	0.070	0.91
O2	0.387	0.132	0.412	1.00

O3	0.220	0.518	0.054	0.89
O4	0.153	0.157	0.544	1.00
O5	0.205	0.273	0.367	1.00
O6	0.139	0.046	0.115	1.00
O7	0.445	0.258	0.170	1.00
O8	0.109	0.490	0.244	0.59
Li1	0.337	0.355	0.290	0.33
Li2	0.441	0.120	0.830	0.33
Li3	0.500	0.000	0.000	0.33

Table 3.2 Multi-step sintering schedule and Relative density of LTPO samples

S.no	**Sample ID**	**Sintering Temperature**	**Measured Density ($g.cm^{-3}$)**	**Relative Density (%)**
1.	T1	1100 ºC for 2 hours and 1050 ºC for 2 hours	4.63	79.3
2.	T2	1100 ºC for 2 hours and 1050 ºC for 4 hours	4.81	82.4
3.	T3	1100 ºC for 2 hours and 1050 ºC for 6 hours	4.73	80.9
4.	T4	1100 ºC for 2 hours and 1050 ºC for 8 hours	4.50	77.1
5.	T5	1100 ºC for 2 hours and 1050 ºC for 10 hours	4.54	77.8

3.2.2.2 Scanning Electron Microscopy (SEM)-Energy Dispersive X-ray Spectroscopy (EDX) and Tunneling Electron Microscopy (SEM) Analysis

Grain size typically increases and porosity generally reduces during scheduled step sintering between 900 ºC and 1200 ºC for different ceramic materials, leading to an increase in relative density [114]. Fig. 3.6 shows the cross-section SEM images of as-prepared LTPO pellets. As shown in Fig. 3.6 (a-e), pellets have a dense microstructure with a heterogeneous grain structure; smaller grains are distributed around large grains [115]. The heterogeneous grains in sample T2 were well-connected, resulting in a higher density than in other samples. The extent of porosity increases after T2, resulting in a low density of the pellet, and low density can reduce the ionic conductivity of the samples. Figure 3.7 (a-e) shows the elemental mapping of T2, which confirms the homogeneous distribution of Ta, P, and O, respectively, throughout the sample and weight percentage analysis using mass sum spectrum analysis. Figure 3.8 shows the HRTEM images of sample T2, revealing good particle contact and the presence of an amorphous phase between the LTPO particles. This suggests that during the sintering of sample T2, the particle surfaces dissolved, forming an amorphous phase at the boundaries [116]. Combined with the XRD pattern of T2, it is evident that the intermediate amorphous phases recrystallized into a $LiTaO_3$ trigonal structure. The amorphous phase was composed of Li, Ta, and O elements [112]. Optimizing the sintering schedule significantly influences the crystal structure, density, and microstructure of LTPO ceramics. Formation and recrystallization of intermediate amorphous phases into $LiTaO_3$ were observed, highlighting the impact of lithium loss at

high temperatures and formation of heterogeneous crystal structure after the sintering process. These factors collectively enhance densification and lower the sintering temperature, which is crucial for analyzing the LTPO sample T2 electrical properties.

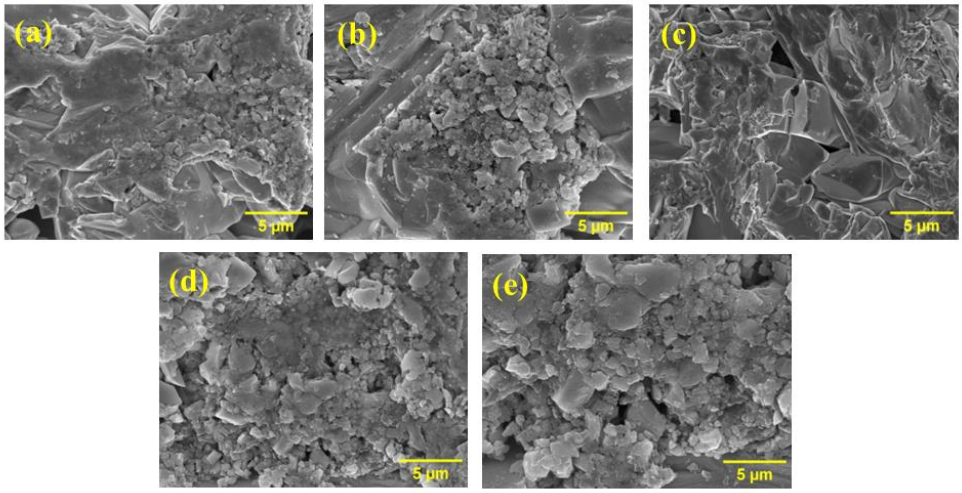

Fig. 3.6 SEM micrograph of the sample (a) T1, (b) T2, (c) T3, (d) T4, (e) T5 pellet at 10 KX.

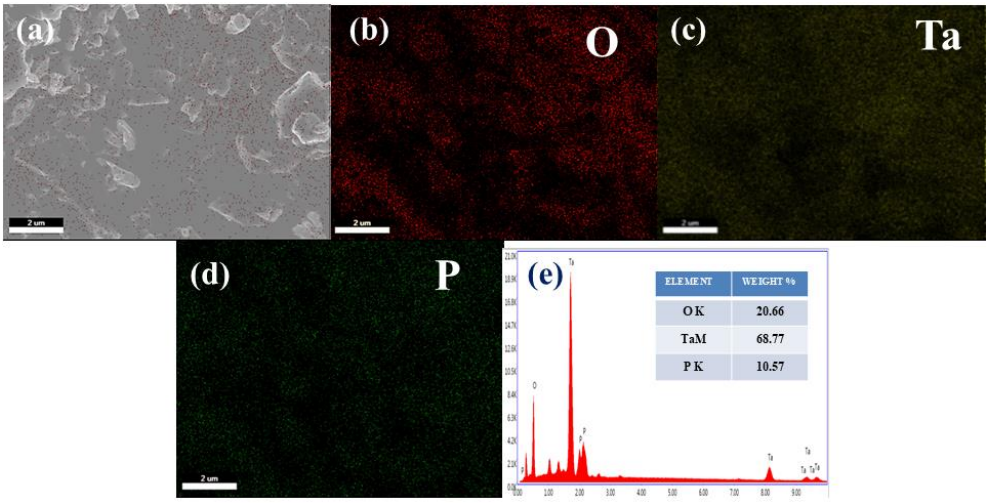

Fig. 3.7 (a) Elemental mapping images of (b) O(red), (c) Ta(yellow), (d) P(green) of LTPO, (e) Result of EDS analysis and mass sum spectrum of LTPO.

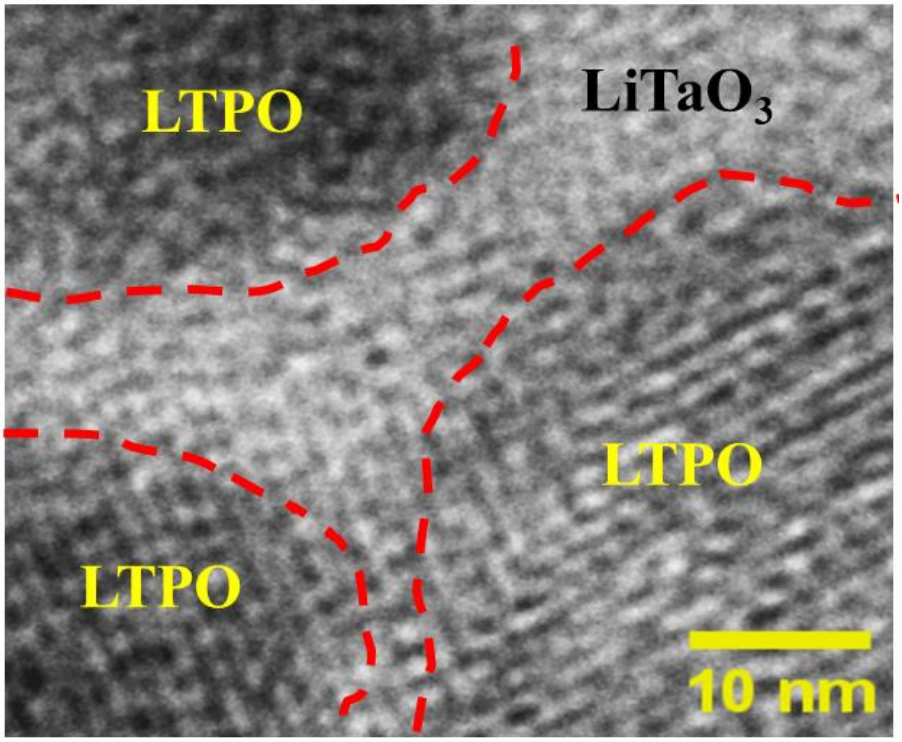

Fig. 3.8 HRTEM image of the T2 sample

3.2.3 Dielectric and Impedance Characterization

3.2.3.1 Dielectric Spectroscopy

Variation of ε' and ε'' with frequency at different temperatures is given in Fig. 3.9, 3.10. Lower frequencies reveal the highly dispersed region with higher permittivity values, which suggests the presence of the Maxwell-Wagner relaxation model and space charge polarisation arises from the heterogeneous crystal structure of ceramics [117]. The higher values of permittivity at lower frequencies can be thought of as a combination of

a larger number of well-conducting grains separated by areas with lower grain boundary conductivity. The charge carriers readily travel through the grains and gather at grain boundaries under the influence of the externally applied field [118-119]. Figure 3.11 (a) displays the dielectric loss variation with temperature at different frequencies. The temperature and charge carrier mobility are the primary determinants of the dielectric loss, temperature-dependent variations in charge carrier mobility lead to higher dielectric losses. When the frequency of the applied field equals the hopping frequency of charge carriers, it results in the appearance of a dielectric loss peak. The shift of the dielectric loss peak towards the higher temperature can be attributed to the increment in the charge carrier hopping frequency with temperature [120]. The two relaxation peaks at high and intermediate to low frequencies represent the processes of grain relaxation and grain boundary relaxation. In general, the sample's ionic conductivity decreases with a longer relaxation time. Both relaxation peaks move towards higher frequencies with increasing temperature. As a result, we get higher conductivity values at higher temperatures since their relaxation durations are short. The relaxation behaviour of LTPO due to thermal process inside the bulk is shown by the shift of the loss peak towards higher temperatures. The peak's maxima position met the requirement $\omega\tau = 1$, and the activation energy of relaxation time was thus calculated using the Arrhenius equation described by equation 2.10 (chapter 2 section 2.4.3.1).

Equation 2.10 yields the curve between ln (τ) vs 1000/T(K) shown in fig. 3.11(b) which reveals the relaxation activation energy (~0.21 eV) and intercept shows the characteristic relaxation time(τ_o) ~5.78 × 10^{-10}s. Shorter relaxation time and low

activation energy suggest that ions can move and rearrange themselves faster when an external field is applied, and a lower energy barrier for ionic movement indicates fast ionic motion resulting in higher room temperature ionic conductivity of ceramics, and it additionally shows the possibility that ionic conductivity will increase as the temperature rises.

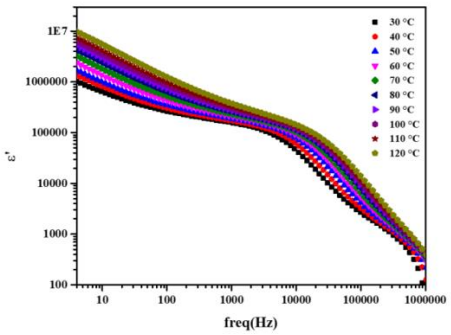

Fig. 3.9 Variation of ε' with respect to frequency in the temperature range of 30 ºC to 120 ºC of sample T2.

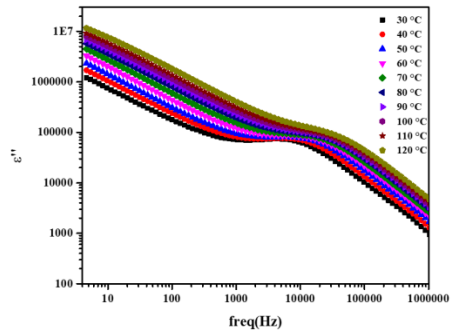

Fig 3.10 Variation of ε'' with respect to frequency in the temperature range of 30 ºC to 120 ºC of sample T2.

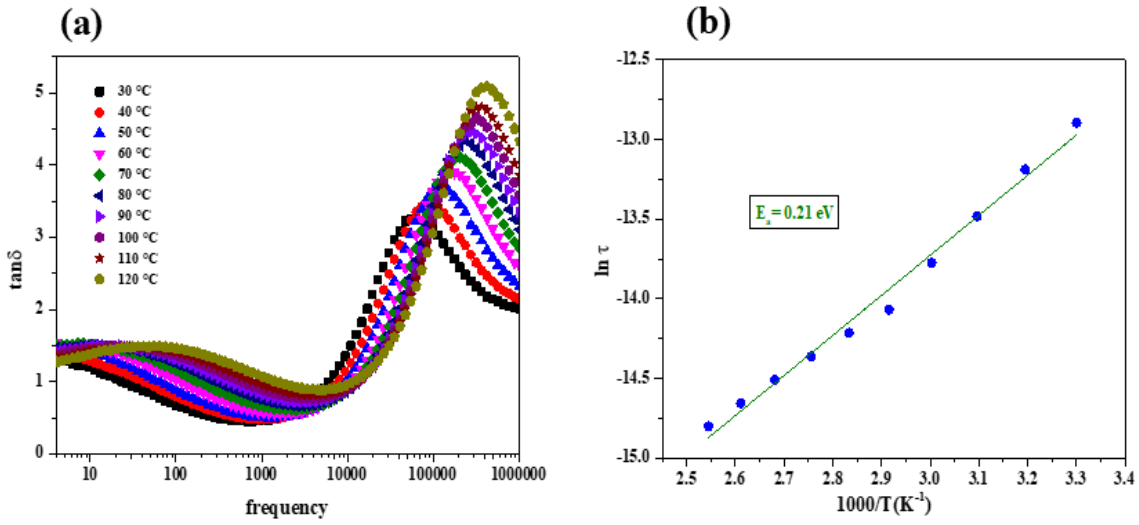

Fig. 3.11 Variation of: (a) tan δ with respect to frequency in the temperature range of 30 ºC to 120 ºC (b) Arrhenius plot of relaxation time vs temperature of sample T2.

3.2.4.2 Impedance Spectroscopy

Figure 3.12 illustrates how the real part (Z') and imaginary part (Z") of the impedance vary with frequency at different temperatures ranging from 30 ºC to 120 ºC. The values of Z' are observed to drop as temperature and frequency rise, as seen in Figure 3.12 (a), implying a negative temperature coefficient of resistance (NTCR), hence increasing the sample's ac conductivity, which was expected from the lower dielectric relaxation activation energy discussed in the previous section [121]. Furthermore, at high frequencies, the curves start to merge together, indicating the potential release of space charge and a decrease in the sample's barrier height [122]. One relaxation peak when the temperature is less than 50 ºC may be seen in Figure 3.12 (b) at a higher frequency and two relatively separate temperature-dependent peaks at a particular frequency are seen

for temperatures more than 50 ºC, and these peaks shift to the higher frequency side as the temperature rises. This behaviour indicates a thermally triggered relaxation phenomenon in the sample, and 50 ºC is a point where a decrease in the mobile charge carriers' relaxation times with rising temperatures [123]. Figure 3.13 displays the Z' vs Z″ complex impedance graphs (Nyquist plots) of the LTPO ceramics at different temperatures. Two depressed semi -circular arcs merging with a tail at low frequency make up the Z' vs. Z″ curves for the sample at all of the selected temperatures. These can be expressed as an equivalent circuit of a parallel combination of resistance and constant phase element connected in series (-RQ-RQ-Q), as shown in the inset of Fig 3.13. This suggests that the conduction mechanisms in the LTPO ceramics have two distinct origins. From a microstructural perspective, the LTPO sample has the presence of $LiTaO_3$ secondary phase on the grain boundary, resulting in distinct resistivity and dielectric permittivity. While the low frequency tail and merged semicircle (intermediate frequency) with high Z values is attributed to the grain boundary resistance and electrode polarization effect, the high frequency semicircle with low Z values illustrates the LTPO grain resistance. The equations 2.15-2.16 (chapter 2, section 2.4.3.2) provide the real Z' and imaginary Z″ parts of complex impedance [115]. The electrical behaviour of the ceramic is shown by the semi-circular arcs and the size of their intercepts on the real axis. Equative RC circuit fitting of complex impedance semicircles at various temperatures yields the resistance and capacitance values of the bulk, grain boundaries, and electrode resistance, fitted parameters values calculated using equations 2.17-2.18 (chapter 2, section 2.4.3.2) are shown in Table 3.3, the value total grain

conductivity calculated using fitting data is 5.1×10^{-4} Scm^{-1} and grain boundary conductivity is 5.36×10^{-6} Scm^{-1}. The behaviour of the negative temperature coefficient of resistivity (NTCR), which is similar to that of semiconductors, is confirmed by the clear reduction in R1 and R2 values with increasing temperature. Further, the complex impedance measurement gives a convincing justification for the Maxwell-Wagner type of relaxation, specifically the contributions from the grain and grain-boundary regions, which is in line with the previous section's dielectric analysis. The influence of temperature on relaxation time (τ) calculated from the relaxation frequency derived from the fitting results of the impedance plots are shown in Figure 3.14 (a, b). The Arrhenius relation is followed in this plot, given by equation 2.19(chapter 2, section 2.4.3.2). The grain section of the LTPO ceramic has Ea values of 0.22 eV, while the intergranular part is 0.40 eV as shown in Fig. 3.14 (a,b), respectively. The grain activation energies are approximately the same as calculated from the dielectric. This consistency shows that both techniques are capturing similar underlying processes related to charge carrier dynamics inside the material**.** Furthermore, to investigate the ion conduction mechanism due to heterogeneity in the crystal structure of LTPO sample T2, AC conductivity analysis has been employed in the temperature and frequency range of 30 ºC to 120 ºC and 1 MHz to 4 Hz, respectively, as shown in Fig. 3.15. Figure 3.15 shows the step-like feature, so for analysis purposes, we divided it into two portions: (i) Region 1 (low to intermediate frequency) and (ii) Region 2 (intermediate to high frequency). At moderate frequencies, the second plateau region became visible. When the temperature rises, the second plateau's area shrinks. This step-like feature showing two plateaus is attributed to

the difference in conductivity due to heterogeneous crystal structure (amorphous $LiTaO_3$ phase at grain boundary), formerly reported heterogeneous structure also shows this kind of conduction mechanism [125].

Increased electrical conductivity of LTPO with temperature may be due to thermally driven charge carriers' increased drift mobility [126]. Frequency dependence of ac conductivity is fitted using Jonscher's power law given in equation 2.12 (chapter 2, section 2.4.3.1). Both the regions (1 and 2) are fitted solely using equation (21) in the Origin software; fitted parameter values are shown in Table 3.4. Maxwell-Wagner effect, which is typically found in heterogeneous systems where there is a significant difference in conductivity values for two counterparts, is demonstrated by the presence of a second plateau in the mid-to-high-frequency region, as shown by our heterogeneous structure of LTPO. The conduction mechanism used is revealed by the temperature dependency of the s parameter [127], it can easily be seen in table 3.4 that the value of s for region 1 decreases linearly with an increase in temperature so it can be explained using the CBH conduction mechanism model and for region 2 value of s first decreases then increases with an increase in temperature, here mechanism is followed by OLPT model. From the well-fitted data, activation energy of the conductivity is calculated using the Arrhenius equation given in equation 2.13 (Chapter 2, section 2.4.3.1). Figure 3.16 (a, b) shows the Arrhenius plot of regions 1 and 2, respectively, which concludes that the activation energy for region 1 and region 2 is 0.42 eV and 0.18 eV, respectively. Additionally, it is verified that the activation energy values derived from conductivity fitting analysis and impedance fitting analysis are extremely similar, confirming that the same type of charge

carriers may be responsible for both the relaxation process and electrical conductivity [128-130].

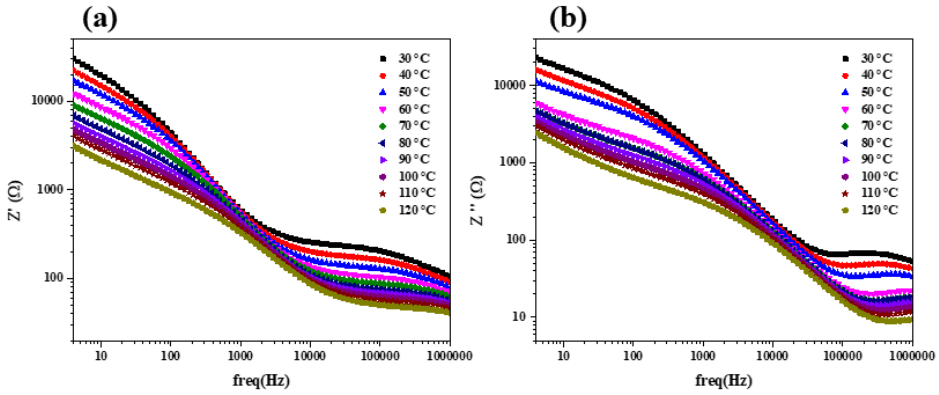

Fig 3.12 (a) Variation of Z' (b) Z'' with respect to frequency in temperature range of 30ºC to 120 ºC of LTPO sample T2 solid electrolyte

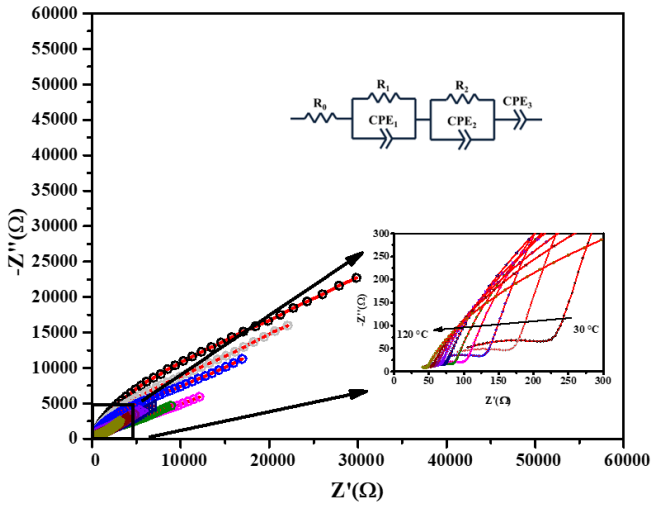

Fig. 3.13 Nyquist plot of the LTPO sample T2 in the temperature range of 30 ºC to 120 ºC.

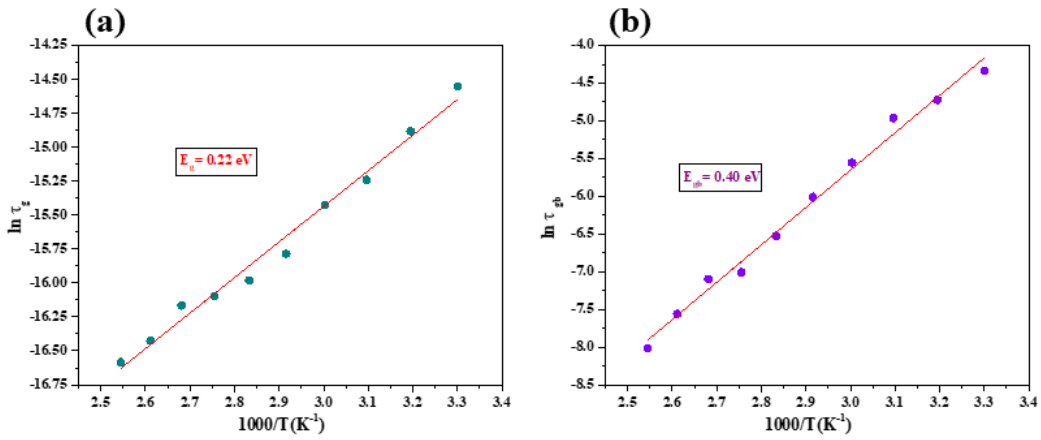

Fig. 3.14 Arrhenius plot of the relaxation time of (a) grain, (b) grain boundary region of the LTPO sample T2.

Table 3.3 Value of significant parameters calculated from the circuit fitting of the Nyquist plot of LTPO sample T2.

S.no		Higher Frequency				Intermediate Frequency				Lower Frequency	
	Temp	R1	P1	n1	C1	R2	P2	n2	C2	P3	n3
1.	30°C	2.73E+02	6.06E-06	0.44	1.75E-09	2.60E+04	1.85E-06	0.7	5.04E-07	6.73E-06	0.62
2.	40°C	2.38E+02	6.98E-06	0.43	1.44E-09	1.63E+04	2.47E-06	0.68	5.45E-07	9.35E-06	0.6
3.	50°C	2.00E+02	8.30E-06	0.42	1.20E-09	1.16E+04	2.94E-06	0.68	6.01E-07	1.36E-05	0.57
4.	60°C	1.99E+02	7.70E-06	0.42	1.00E-09	9.71E+03	2.23E-06	0.69	3.99E-07	2.98E-05	0.31
5.	70°C	1.46E+03	1.06E-06	0.41	9.56E-11	6.05E+03	2.95E-06	0.67	4.06E-07	3.70E-05	0.33
6.	80°C	1.22E+02	9.98E-06	0.42	9.41E-10	3.53E+03	4.07E-06	0.65	4.14E-07	3.54E-05	0.38
7.	90°C	1.12E+02	7.50E-06	0.44	9.12E-10	3.87E+03	2.91E-06	0.64	2.33E-07	4.27E-05	0.38

8.	**100°C**	1.04E+02	1.08E-05	0.42	9.15E-10	2.79E+03	3.81E-06	0.64	2.96E-07	4.81E-05	0.4
9.	**110°C**	9.16E+01	1.53E-05	0.4	8.03E-10	1.76E+03	4.85E-06	0.63	2.96E-07	5.35E-05	0.42
10.	**120°C**	7.55E+01	3.99E-05	0.35	8.30E-10	1.54E+03	4.50E-06	0.62	2.14E-07	6.31E-05	0.45

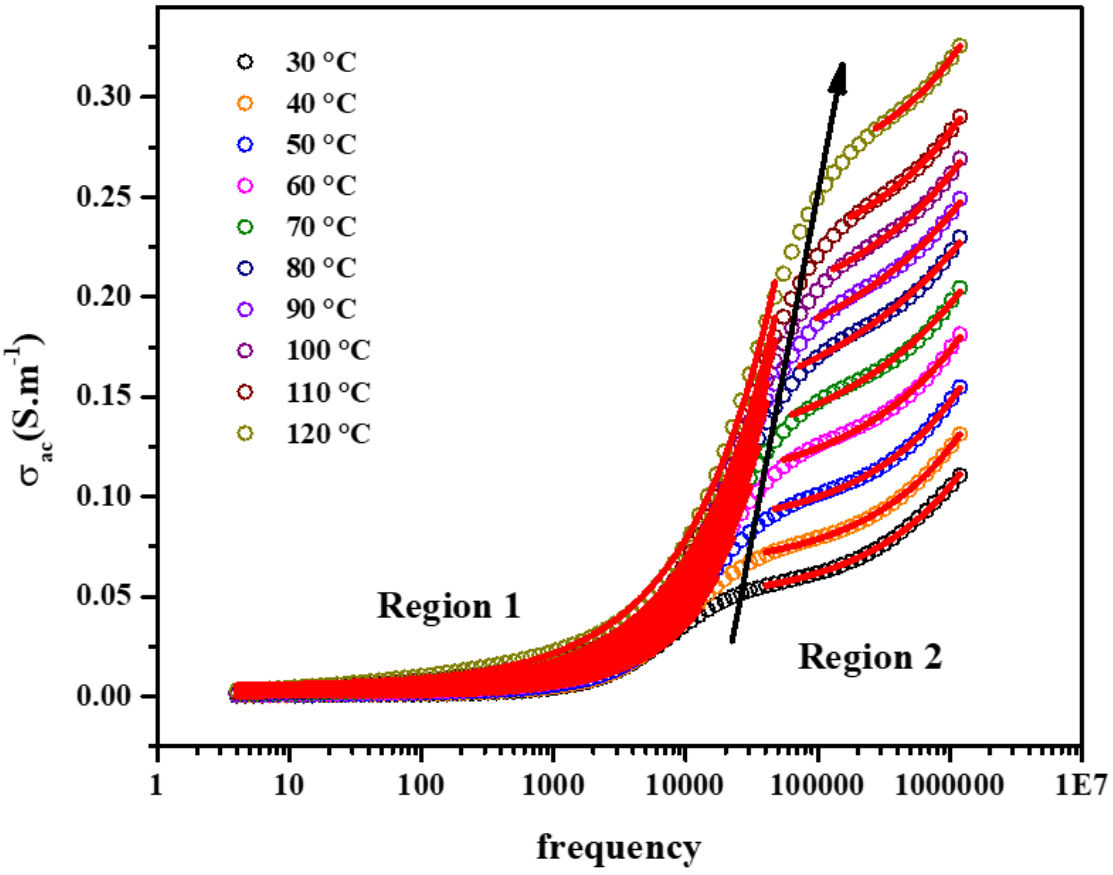

Fig.3.15 AC conductivity vs frequency plot of LTPO sample T2 describing the step-like feature in a temperature range of 30ºC to 120ºC.

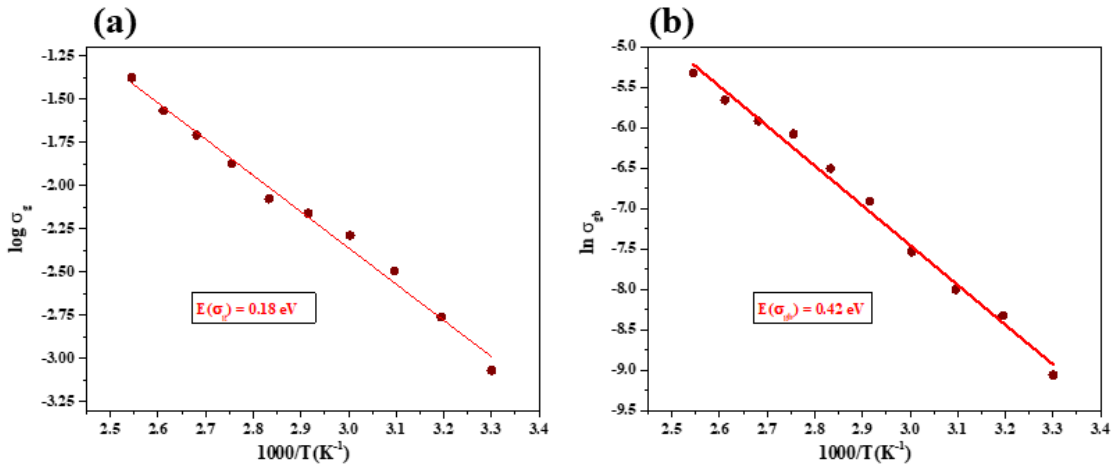

Fig.3.16 Arrhenius plot of the DC conductivity of (a) region 1 (b) region 2 of LTPO sample T2.

Table 3.4 Value of parameters calculated from the Jonscher power law fitting in region 1 and region 2 of LTPO sample T2.

		Region 1			**Region 2**		
S.no	**Temp**	**σ_{dc}**	**A**	**s**	**σ_{dc}**	**A**	**s**
1.	30 ºC	1.16E-04	2.53E-06	0.86	0.04648	6.00E-06	0.58679
2.	40 ºC	2.42E-04	3.29E-06	0.84	0.06326	5.13E-06	0.59971
3.	50 ºC	3.35E-04	4.77E-06	0.81	0.08263	7.87E-06	0.5759
4.	60 ºC	5.34E-04	8.57E-06	0.77	0.10143	3.01E-05	0.49669
5.	70 ºC	1.00E-03	1.20E-05	0.75	0.1153	1.18E-04	0.41719
6.	80 ºC	1.50E-03	1.81E-05	0.72	0.12542	4.99E-04	0.33588
7.	90 ºC	2.30E-03	2.00E-05	0.71	0.15368	2.06E-04	0.38649
8.	100 ºC	2.70E-03	3.78E-05	0.68	0.18113	8.16E-05	0.44002

9.	110 ºC	3.50E-03	3.78E-05	0.67	0.20874	3.24E-05	0.49396
10.	120 ºC	4.90E-03	5.56E-05	0.65	0.2525	9.39E-06	0.56605

3.2.4 Electrical Characterizations

3.2.4.1 Chronoamperometry

The chronoamperometry curve of the LTPO pellet is displayed in fig. 3.17, and it is used to calculate the electronic conductivity of the electrolyte using equation 2.22 (chapter 2, section 2.5.1). After two hours of constant voltage input, the LTPO ceramic sample exhibits a very low I_{SS} of 8.67×10^{-6} mA, which results in a negligible electronic conductivity (σ_e) of 1.22×10^{-8} S cm^{-1} for the LTPO ceramic solid-state electrolyte. The dielectric, impedance, and conductivity results of sample T2 show a strong correlation in the mechanisms governing charge carrier dynamics. Dielectric studies highlight Maxwell-Wagner relaxation and temperature-dependent polarization due to the $LiTaO_3$ secondary phase at grain boundaries. Impedance and conductivity analysis confirm distinct grain and grain boundary contributions with different conduction models, respectively, with consistent activation energies across all techniques. These findings establish LTPO as a promising solid-state electrolyte with high ionic conductivity, low electronic conductivity, and stable dielectric properties, making it ideal for electrochemical applications as a solid-state electrolyte.

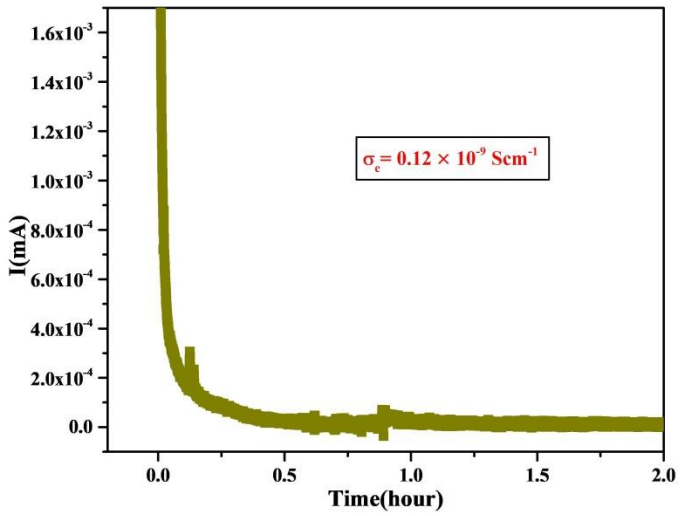

Fig 3.17 Chronoamperometry curve of LTPO sample T2 at a applied voltage of 0.1 V for 4 hours.

3.2.5 Electrochemical Performance Analysis of $LiTa_2PO_8$ Solid State Electrolyte

3.2.5.1 Electrochemical Impedance Spectroscopy (EIS) Analysis

The stability of LTPO ceramic pellets as a solid-state electrolyte in Li-ion batteries has been tested in symmetric cells assembled in CR2032 coin cells. Symmetric cells with an LTPO electrolyte were assembled by stacking lithium chips on both sides of the LTPO pellet with and without a $LiPF_6$-soaked polypropylene buffer layer at the interface. The Electrochemical Impedance Spectroscopy (EIS) curve of the symmetric cell is presented in Fig. 3.18. The impedance measurements, using lithium electrodes (ion non-blocking), generally show a semicircle, which represents the total resistance of the ceramic electrolyte with a small tail in the lower frequency region indicating lithium-ion diffusion. When Li electrodes are used, an additional semicircle is expected in the

impedance spectrum due to the reversible incorporation of lithium ions at the electrolyte-electrode interface. This additional semicircle corresponds to charge transfer resistance and electrode capacitance, which explains the disappearance of the low-frequency tail in favor of the second semicircle [131]. By fitting the impedance data with the equivalent circuit shown in the inset of figure 3.18, the resistance of the pristine cell was calculated to be approximately 27 kΩ, showing high resistance, which gets reduced by 10 times after applying the buffer layer for Li-ion migration.

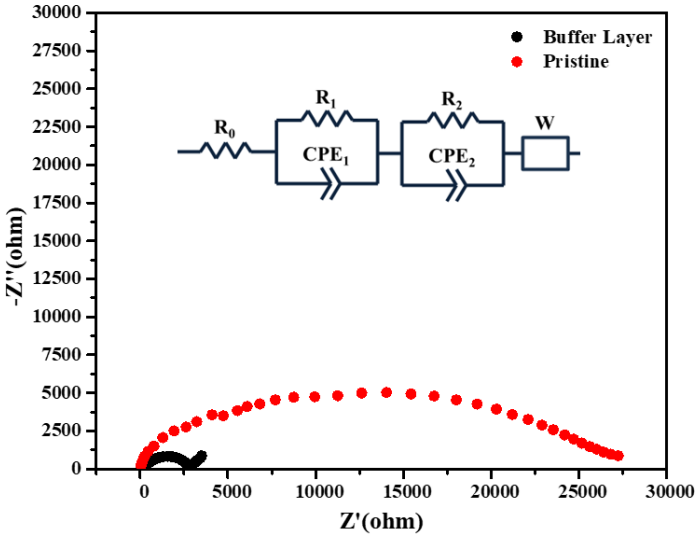

Fig,3.18 Electrochemical impedance spectroscopy curve for pristine symmetric cell and buffer layer used symmetric cell.

3.2.5.2 Galvanostatic Charge-Discharge (GCD) Analysis

Figure 3.19 shows the Li-ion stripping/plating in Li|LTPO|Li cell operated consistently at a current density of 0.1 mA cm^{-2}, which describes that the ionic transport over the Li/LTPO interface was anomalously stable, with a high over-potential value of ~2.4 V for 10 hours, arising from high resistance derived from the EIS plot. This anomalous

ionic transport across the Li/LTPO interface is thought to be caused by the liquid-like ionic conduction found in LTPO and its derivatives [132].

The dielectric, impedance, and AC conductivity studies conducted earlier provide a foundational understanding of the ionic transport behaviour observed here. The activation energy derived from the AC conductivity and impedance spectroscopy reflects the energy barrier for lithium-ion migration through the bulk and grain boundaries of the LTPO electrolyte; a higher grain boundary energy barrier hinders the Li-ion conduction in symmetric cells. Additionally, the cycled symmetric cell was dismantled, and images of the cycled electrolyte are shown in the inset of Fig 3.19. Fig 3.19 (a) reveals that the pellet darkens to black after cycling, indicating the formation of an electrically conductive product that expanded into the LTPO pellet from the Li|LTPO interface .To mitigate the reduction effects on the LTPO electrolyte, a $LiPF_6$ buffer layer at the Li/LTPO interfaces is introduced. This buffer layer can protect the electrolyte from reduction and enhance the cyclability via minimizing the side reaction [133]. The modified cell configuration, Li|BL|LTPO|BL|Li, exhibited a huge reduction in cell resistance contributed by conductivity enhancement of LTPO solid electrolyte via $LiPF_6$ absorption and reduction in interfacial resistance with the ionically conductive interlayer as seen in the previous section [134]. This configuration was cycled at a current density of 0.1 mA cm^{-2}, resulting in significantly reduced polarization voltage (~0.56 V) sustained over 120 hours. As shown in fig 3.19 (b), after 120 hours of cycling, dismantling the symmetric cells revealed that the LTPO pellet with the buffer layer exhibited much less degradation. A quasi-solid-state battery is assembled in a CR2032

coin cell using a $LiFePO_4$ cathode, lithium metal anode, and buffer layer on both interfaces of the solid electrolyte. Lithium metal foil, and the LTPO with $LiFePO_4$ cathode slurry on the other side, shown in Fig 3.20 (c). The coin cell was operated at a constant current of C/10, ranging from 2.4 V to 3.9 V. Figure 3.20 (a) shows the voltage vs specific capacity curve of a full cell, charging-discharging capacities calculated are 118 $mAhg^{-1}$ and 92 $mAhg^{-1}$, respectively, and figure 3.20 (b) shows that after 10 cycles cell shows the stable charge capacity of 71 $mAhg^{-1}$ and discharge capacity of 65 $mAhg^{-1}$ with the efficiency of 92%. Figure 3.20(d) shows the working example of the cell, powering an LED.

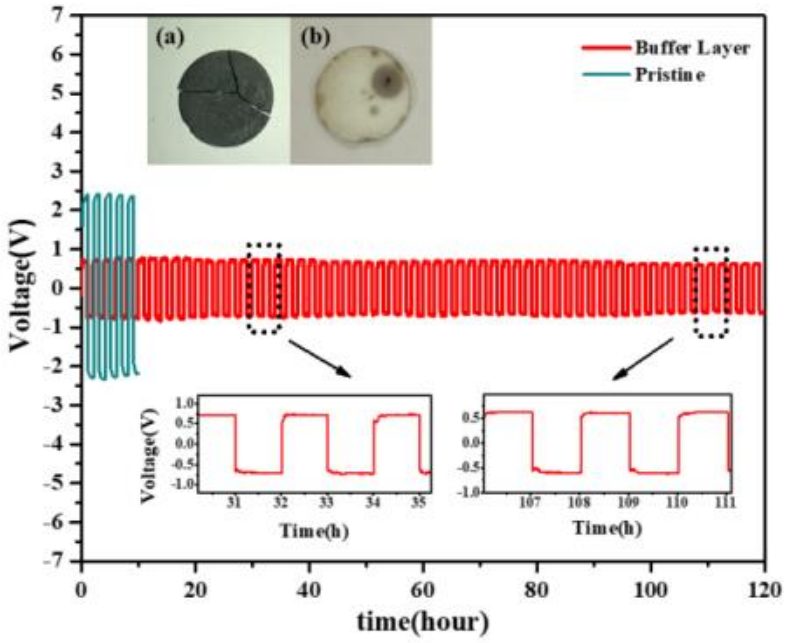

Fig.3.19 Charge-discharge profile of buffer layer and pristine symmetric cell at a current density of 0.1mAcm^{-2}.

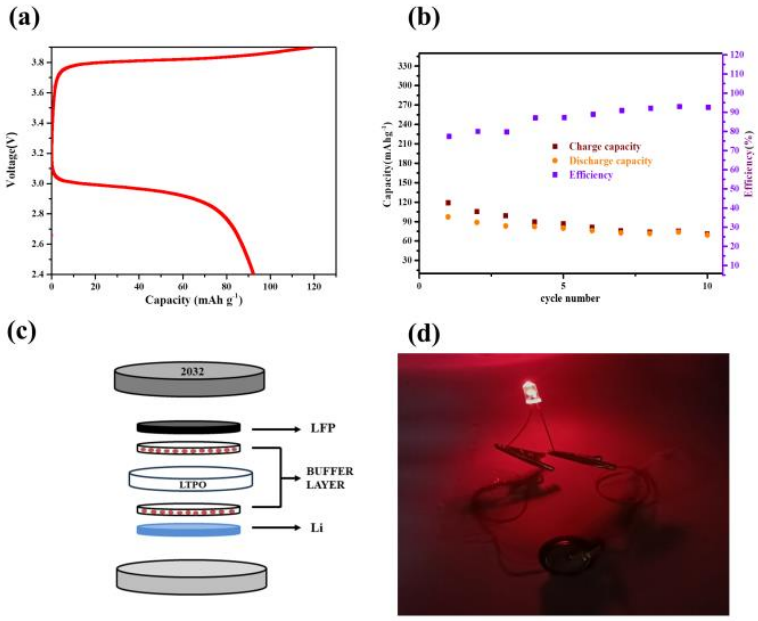

Fig.3.20 (a) Charge/discharge profile of quasi-solid-state battery (b) Capacity, efficiency vs. cycle number of quasi-solid-state battery (c) Schematic representation of components of quasi-solid state battery (d) LED powered via working quasi-solid-state.

In summary, LTPO solid electrolyte was synthesized using the solid-state reaction method. Thermogravimetric (TGA) and differential scanning calorimetry (DSC) analyses up to 1100 °C were conducted to determine the optimal temperature range for phase formation, stepwise sintering, and mass loss assessment utilizing the first derivative of mass loss. The TGA results indicate an 8.4% total mass loss up to 1100°C. Thus, for multi-step simpering, temperatures 1100 °C and 1050 °C have been utilized.

XRD analysis confirmed the formation of the monoclinic LTPO and secondary trigonal LiTaO3 phase during different step sintering schedules, while the resulting material exhibited high relative density, a dense microstructure, heterogeneous grain distribution when subjected to high temperature step sintering at 1100°C for 2 hours and 1050°C for 4 hours and presence of $LiTaO_3$ secondary phase at the grain boundary after step sintering is confirmed using TEM. Dielectric studies revealed Maxwell-Wagner relaxation, with the dielectric dispersion of ε′ and ε″ characterized by frequency. Impedance analysis identified two distinct semi-circular arcs, correlating grain and grain boundary contributions to relaxation processes, further validating the Maxwell-Wagner relaxation mechanism. The AC conductivity study indicated two conduction mechanisms, governed by the CBH and OLPT models, clarifying the role of grains and grain boundaries in charge transport. To enhance electrochemical performance, a buffer layer was introduced at the electrolyte/electrode interface, improving contact and preventing electrically conductive phase in LTPO. A quasi-solid-state battery demonstrated an initial discharge capacity of 92 $mAhg^{-1}$, retaining 65 $mAhg^{-1}$, with a efficiency of 92%.

Chapter 4

Tailoring the Ionic Conductivity of Zr doped $LiTa_2PO_8$

This chapter focuses on enhancing the ionic conductivity of LTPO through Zr substitution doping at the Ta site. The effect of pre-sintering particle size reduction indicates a significant role in modifying the structural characteristics. Dielectric studies revealed Maxwell–Wagner relaxation. An electrochemical study has been performed using symmetric Li|LTZPO|Li cells showing remarkable stability, maintaining continuous cycling for up to 1500 hours.

4.1 Introduction

Compositional engineering (doping/substitution) has emerged to improve LTPO performance. Substituting cations on the Ta or P sites can modify lattice polarizability and introduce beneficial defects that tune the migration barriers for Li-ions. Several substitutional dopants such as Hf, Sc, Te, etc., have been explored with promising outcomes. Recently, Zr substitution for Ta in LTPO was reported to produce a notable improvement in ionic conductivity and make grain boundaries more conductive. Incorporating such dopants thus represents a practical route to move LTPO closer to its theoretical performance [135-137].

In this chapter, Zr-doped LTPO ($Li_{1+x}Ta_{2-x}Zr_xPO_8$; LTZPO) has been synthesized via solid-state reaction route, and the effect of uniform particle size prior to sintering has been tested using XRD, SEM, and EDS analyses, respectively. The frequency and temperature response of LTZPO-0.1 solid electrolytes has been investigated to estimate using various conduction mechanisms. Further, LTZPO electrochemical performance as a Li-ion solid-state electrolyte using the protective buffer layer (BF) has been studied in a quasi-solid-state symmetric cell and full cell. Synthesis of LTZPO ceramics was carried out via a solid-state route as mentioned in Chapter 2, Section 2.1.1.2. Moreover, physiochemical, electrical, and electrochemical characterizations of LTZPO ceramic are performed and explained in Chapter 2 Section 2.4-2.5.

4.2 Results and Discussion

4.2.1 Structure and Morphological Analysis

XRD patterns of pristine LTPO and Zr-doped compositions with varying concentration of zirconium from 0.1 to 0.3 are ~~is~~ shown in Fig. 4.1.(a) LTZPO-0.1 crystallises in the monoclinic phase with C2/c space group, confirming that Zr incorporation at Ta sites into the LTPO lattice with some peaks of $LiTa_3O_8$ secondary phases [132]. However, higher Zr concentrations ($x > 0.1$) lead to more pronounced changes in peak intensity and multiplicity, likely reflecting increased disorder and secondary phases. The LTZPO-0.1 sample exhibits the most balanced profile. Figure 4.2 shows the impedance plot of LTPO, LTZPO-0.1, LTZPO-0.2, and LTZPO-0.3, revealing that the sample LTZPO-0.1 shows the lowest x-intercept values, concluding the lowest possible resistance for Li ion conduction. Hence, LTZPO-0.1 quantitative analysis is further required to test its performance as Li-ion conducting ceramics. FWHM of sharp and intense XRD peaks is modelled using the Pseudo-Voigt function with reliable refinement parameters (χ^2= 5.02, R_{WP}= 7.56%, R_P= 4.83%) and lattice parameters (a= 9.73 Å, b= 11.55 Å, c= 10.71 Å, α= 90.00^0, β= 89.90^0, γ= 90.00^0, vol.= 1204.84 $Å^3$) shown in Fig. 4.1 (b). The site occupancies and fractional parameters are shown in Table 4.1

Dopant strategy and calcinated powder particle size, are the crucial parameters for lowering the sintering temperature and high density of the ceramic. LTPO ceramic sintered at ~1100 °C yields a high density ceramic but with less ionic conductivity and lithium losses at high temperature, as discussed in Chapter 3. Hence, the lower temperature 1050 °C has been taken as the sintering temperature, as substitutional doping reduces the sintering temperature and ionic conductivity, as documented in the previous literature [114,135]. To further analyse the effect of particle size prior to the

sintering, ball milling of the calcinated powder before sintering has been performed as (a) High rpm ball milling (500 rpm), (b) Low rpm milling (100 rpm). Figure 3 (c), 3 (e) shows the effect of milling speed on particle size as particle size gets reduced after milling at 500 rpm, evaluated to be 24.14 um and 50.98 um, respectively, for 500 rpm and 100 rpm milling. Figure 4.3 (d), 4.3 (f) shows the cross-sectional SEM images of the sintered pellets after milling at 500 rpm and 100 rpm, Fig. 4.3(d) shows that the pellet derived from the 500 rpm milled powder has a more dense and compact microstructure with minimal grain boundary cracks and reduced. In contrast, the pellet obtained from 100 rpm milling shows relatively less dense grain packing with noticeable intergranular defects. The relative densities of the pellets were 87% and 84% for the 500 rpm and 100 rpm samples, respectively, measured using the Archimedes' principal, confirming enhanced densification at 500 rpm milling speed. The improved microstructural integrity in the high rpm processed pellet is expected to promote stable lithium cycling and suppress dendritic growth by providing uniform ionic transport pathways and better mechanical robustness. Figure 4.3 (a) and 4.3 (b) show the structural evolution of the LTZPO-0.1 after two different approaches, justifying the presence of crystalline structure after sintering. However, the shifting of 2 theta values is different in each case after sintering. The 500 rpm milled sample shows a shift of the dominant diffraction peak toward higher the 2θ values after sintering, indicating lattice contraction and the development of compressive stress that can enhance the particle packing during densification [138]. Whereas, 100 rpm milled sample, possessing a larger particle size shows a peak shift towards lower 2θ values after sintering, suggesting lattice expansion

associated with tensile strain [138]. To further validate the strain in the crystal structure of LTZPO-0.1 the Williamson-Hall (W-H) method was employed. The W-H plot uses the total peak broadening of the XRD peak to predict the compressive or tensile microstrain of the crystal and is given by equation 2.5 (Chapter 2, section 2.4.2.1). Figure 4.4 represents the W-H plots of LTZPO-0.1 prior to and after sintering at both rpm. Micro-strain thus calculated from the W-H plot is -0.00262 and 0.000855, respectively, for high rpm and low rpm milling. Negative sign in the micro-strain shows the presence of compressive stress in the structure, validated from the structural analysis of a 500 rpm milled sample [138]. Figure 4.5 shows the EDX images of the LTZPO-0.1, justifying the homogeneous elemental distribution over the material.

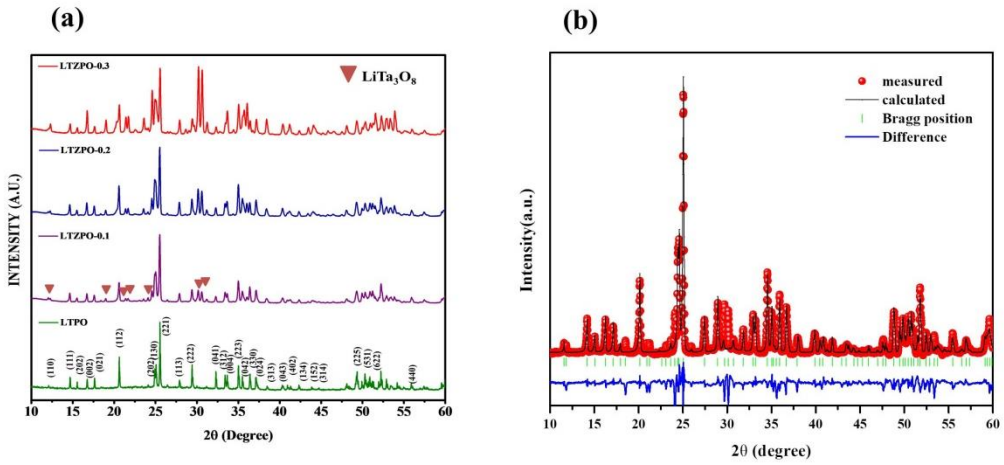

Fig 4.1. (a) XRD pattern of LTPO, LTZPO-0.1, LTZPO-0.2 and LTZPO-0.3 calcined at 1050 °C for 12 h. (b) rietveld refinement result of LTZPO-0.1

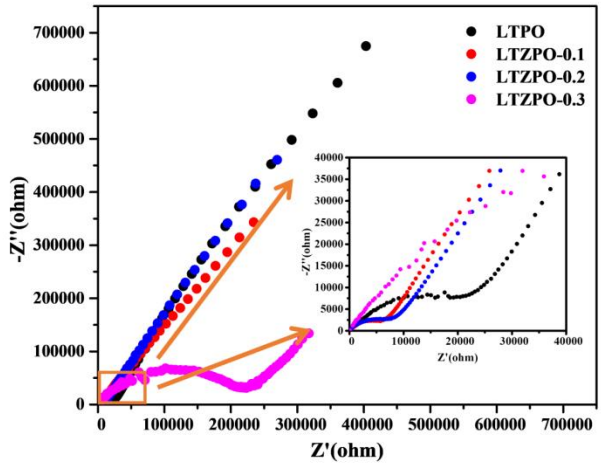

Fig 4.2 Impedance plot of LTPO(black), LTZPO-0.1 (red), LTZPO-0.2 (blue), LTZPO-0.3 (magenta)

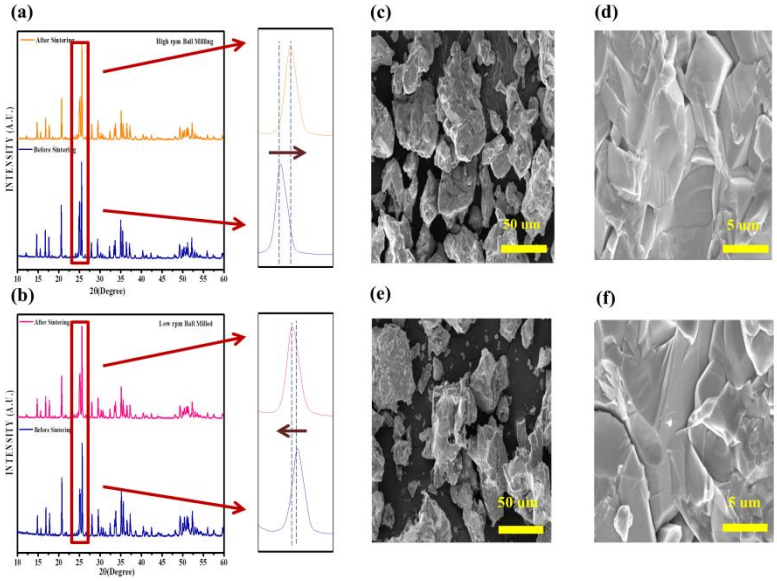

Fig 4.3 Evolution of structure (a) after high rpm milling (b) after low rpm milling, SEM micrograph of (c) after high rpm milling (d) sintered pellet after high rpm milling, (e) after low rpm milling (f) sintered pellet after low rpm milling

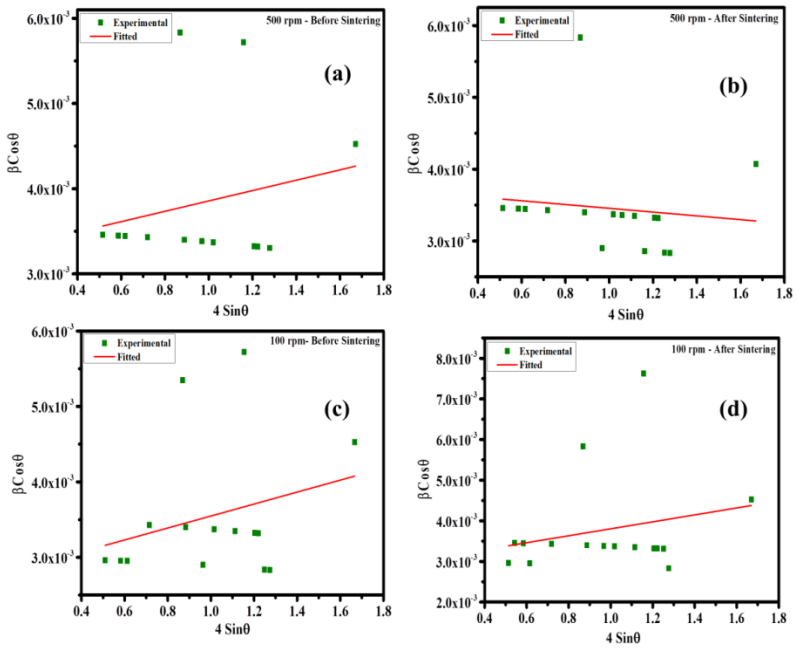

Fig 4.4 W-H plot of (a) 500 rpm LTZPO-0.1 before sintering, (b) after sintering, (c) 100 rpm LTZPO-0.1 before sintering and (d) after sintering.

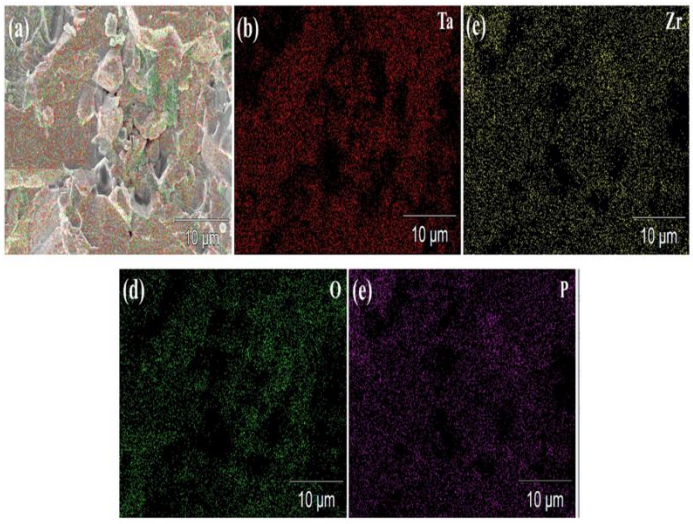

Fig 4.5 (a) Elemental mapping images of (b) Ta (red), (c) Zr (yellow), (d) O (green), (e) P (pink) of LTZPO-0.1

Table 4.1 Refined parameters of LTZPO-0.1

Element	x	y	z	Occupancy
Ta1	0.244894	0.097858	0.257922	0.68
Ta2	0.000000	0.346077	0.250000	0.68
Ta3	0.000000	0.000000	0.000000	0.60
Zr	0.000000	0.000000	0.000000	0.08
P	0.502732	0.203652	0.068732	1.00
O1	-0.025653	0.330086	0.076299	0.70
O2	0.347126	0.094708	0.477629	0.97
O3	0.385925	0.487596	0.170240	1.00
O4	0.096719	0.141334	0.566241	1.00
O5	0.137193	0.261029	0.418779	0.74
O6	0.224339	0.144595	0.103402	0.78
O7	0.400652	0.188207	0.128814	1.00
O8	0.133753	0.494033	0.286449	0.93
Li1	0.492059	0.396090	0.148949	0.41
Li2	0.921727	0.306214	0.403741	0.69
Li3	0.500000	0.000000	0.000000	0.00

4.2.2 Dielectric and Impedance Characterization

4.2.2.1 Dielectric Spectroscopy

Figure 4.6 (a, b) shows the variation of ε' and ε'' with frequency at different temperatures. Lower frequencies show a dispersed region with higher permittivity values, suggesting the presence of the Maxwell-Wagner relaxation and space charge polarisation arising from the crystal structure heterogeneity [119]. At high temperature, charge carriers successfully hop in the direction of the applied AC field, resulting in the motion of charge carriers towards the high-energy barrier side, which corresponds to an increase in polarisation and permittivity [120]. Figure 4.7 (a,b) displays the dielectric

loss variation with frequency at different temperatures and the Arrhenius plot of relaxation times. Temperature variations lead the charge carrier to increase the mobility, resulting in higher dielectric losses when the frequency of the applied field equals the hopping frequency and corresponds to the appearance of a dielectric loss peak [120]. Two relaxation peaks at high and intermediate to low frequencies show the presence of the processes of grain and grain boundaries relaxation, respectively. Both relaxation peaks seem to be moving towards higher frequencies with temperature, resulting in higher conductivity at high temperatures. The relaxation behaviour of the material due to thermally activated processes results in the shift of the dielectric loss peak towards high temperatures. Activation energy of relaxation time(τ) is calculated using the Arrhenius equation given by equation 2.10 (chapter 2, section 2.4.3.1). Figure 4.7 (b) shows the relaxation activation energy of 0.14 eV and 0.20 eV for grain and grain boundaries with the relaxation times of ~3.05×10^{-8} s and ~4.82×10^{-9} s, respectively.

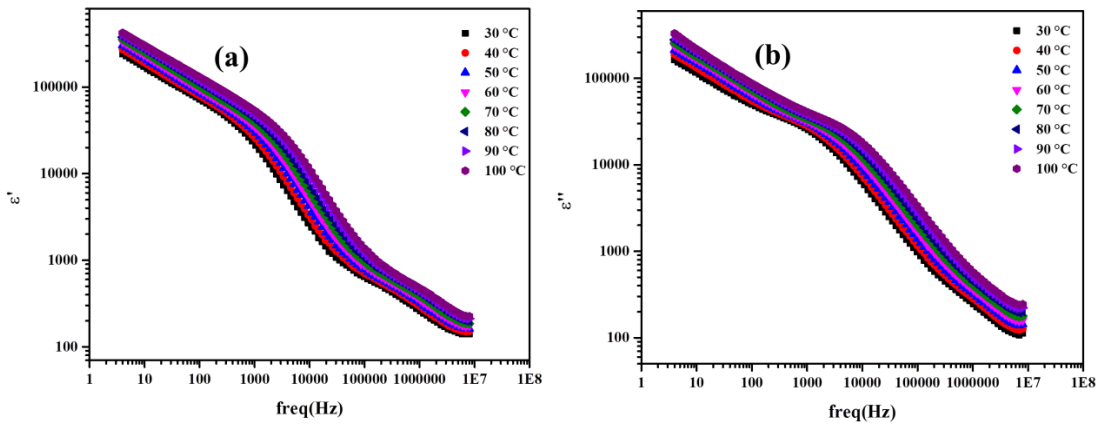

Fig 4.6 Variation of: (a) ε' (b) ε'' vs frequency in a temperature range of 30 ºC to 100 ºC of LTZPO-0.1.

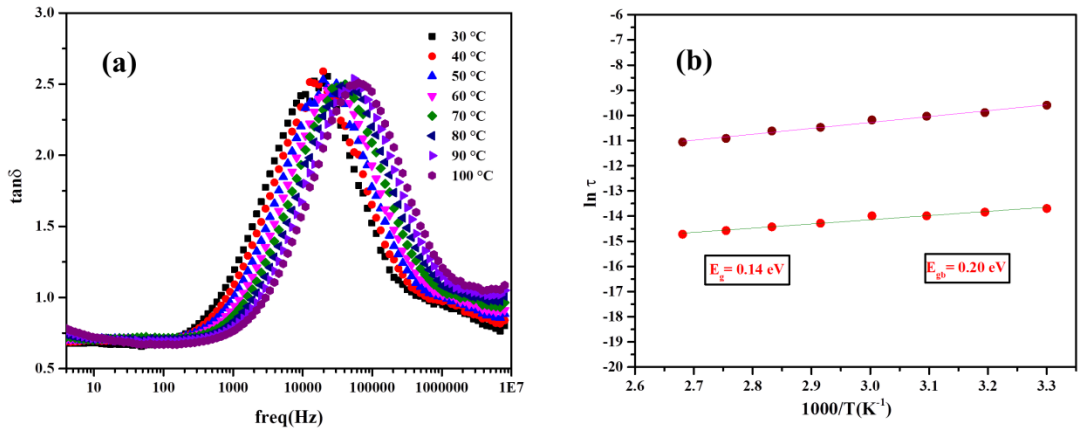

Fig 4.7 Variation of: (a) tan δ vs. frequency in a temperature range of 30 ºC to 100 ºC (b) Arrhenius plot of relaxation time vs temperature of LTZPO-0.1.

3.2.4.2 Impedance Spectroscopy

21

Figure 4.8 (a,b) shows the variation of real (Z') and imaginary (Z'') parts of the impedance with frequency at different temperatures ranging from 30 ºC to 100 ºC. Figure 4.8 (a) shows that Z' values decrease with an increment in temperature and frequency, suggesting a negative temperature coefficient of resistance (NTCR) behaviour that raises the sample conductivity [121]. The Nyquist plot (Z' vs. Z″) of the LTZPO-0.1 at various temperatures is shown in Fig 4.9, curves consist of two depressed semi-circular arcs that merge with the tail at low frequency and can be fitted using the equivalent electronic circuit shown in the inset of Fig. 4.9. Implying that there are two different sources for the conduction mechanisms in the LTZPO-0.1. According to structural analysis, the LTZPO sample exhibits the existence of $LiTa_3O_8$ secondary phase that can be segregated at grain boundary during high-temperature sintering. The high-frequency semicircle with low Z values shows the LTZPO-0.1 grain resistance, and the

low-frequency tail and merged semicircle (middle frequency) with high Z values are related to the grain boundary and electrode polarization effects. Equative RC circuit fitting of complex impedance semicircles at various temperatures yields ionic conductivity values of the bulk and grain boundaries; values are shown in Table 4.2; the total conductivity value calculated at 30 ºC is 0.24×10^{-4} S cm^{-1}. The NTCR behavior, similar to that of semiconducting materials, is confirmed by the reduction in resistance values with increasing temperature [124]. The complex impedance measurement gives a justification for the presence of the Maxwell-Wagner type of relaxation's contribution from the grain and grain boundary, which in line with the previous dielectric section analysis.

The ion conduction mechanism of LTZPO-0.1 analysis has been done in the temperature and frequency range of 30 ºC to 100 ºC and 1 MHz to 4 Hz, respectively, as shown in Figure 4.10. A step-like feature is shown in the graph that divides it into two regions: (i) Region 1- low to intermediate frequency range, and (ii) Region 2 - intermediate to high frequency range. This step-like feature showing two plateaus can be evaluated as the presence of two different conduction pathways due to heterogeneous crystal structure ($LiTa_3O_8$ impurity phase). Previously reported heterogeneous structured materials also show similar conduction mechanism pattern [125]. Increased conductivity of LTZPO-0.1 with temperature is due to the increment in the thermally driven charge carrier's mobility [126]. Frequency dependence of ac conductivity is fitted using Jonscher's power law described by the equation 2.12 (chapter 2, section 2.4.3.1). Regions (1 and 2) are fitted separately using Jonscher's power equation in the Origin software. Table 4.2

shows the values of fitted parameters. The presence of a second plateau shown by the heterogeneity in the structure of LTZPO also supports the presence of the Maxwell-Wagner effect. The conduction mechanism used in conductivity is revealed by the temperature dependency of the‘s’ parameter values [127]. It can easily be seen in Table 4.3 that the value of ‘s’ for region 1 decreases linearly with an increase in temperature corresponding to the CBH conduction mechanism model, and for region 2, the value of ‘s’ first decreases, then increases with an increase in temperature corresponding to the OLPT model. Activation energy of the conductivity is calculated using the Arrhenius equation. Figure 4.11 (a,b) shows the Arrhenius plot of regions 1 and 2, respectively, concluding that the activation energy for region 1 and region 2 is 0.18 eV and 0.13 eV, respectively. Hence, it is seen that the activation energy values derived from conductivity fitting analysis and impedance fitting analysis are extremely similar, confirming that the same type of charge carriers may be responsible for both the relaxation process and electrical conductivity [128-130].

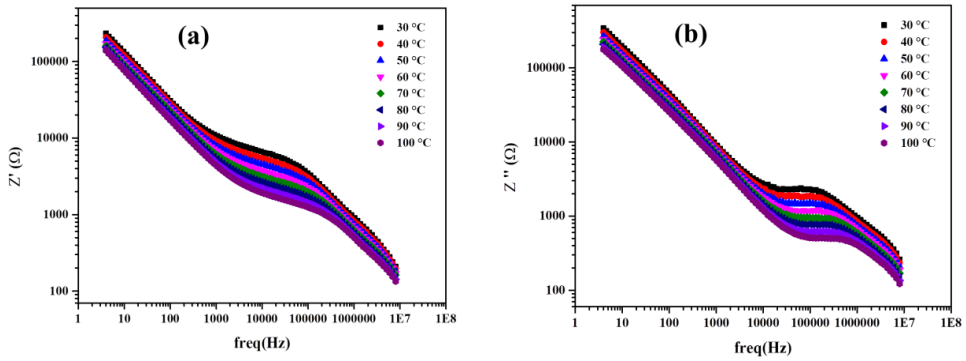

Fig 4.8 Variation of: (a) Z’ (b) Z’’ vs frequency in a temperature range of 30 ºC to 100 ºC of LTZPO-0.1.

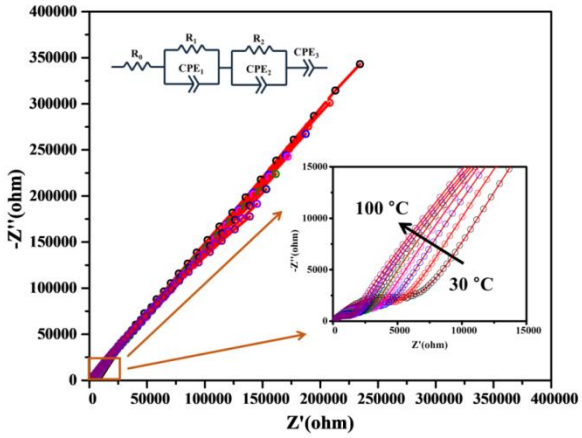

Fig 4.9 Nyquist plot of LTZPO-0.1 in a temperature range of 30ºC to 100ºC.

Table 4.2 ionic conductivity values of the bulk and grain boundaries of LTZPO-0.1

T (°C)	R_g (Ω)	R_{gb} (Ω)	σ_g (S/cm)	σ_{gb} (S/cm)	σtotal (S/cm)
30	10566.72	35647.33	1.04×10^{-4}	3.09×10^{-5}	2.38×10^{-5}
40	9861.77	31998.50	1.12×10^{-4}	3.44×10^{-5}	2.63×10^{-5}
50	9003.31	28296.65	1.22×10^{-4}	3.89×10^{-5}	2.95×10^{-5}
60	8664.00	25592.27	1.27×10^{-4}	4.30×10^{-5}	3.21×10^{-5}
70	8285.00	23257.38	1.33×10^{-4}	4.73×10^{-5}	3.49×10^{-5}
80	7535.00	21982.75	1.46×10^{-4}	5.01×10^{-5}	3.73×10^{-5}
90	7031.00	21134.45	1.56×10^{-4}	5.21×10^{-5}	3.91×10^{-5}
100	6305.00	20886.02	1.75×10^{-4}	5.27×10^{-5}	4.05×10^{-5}

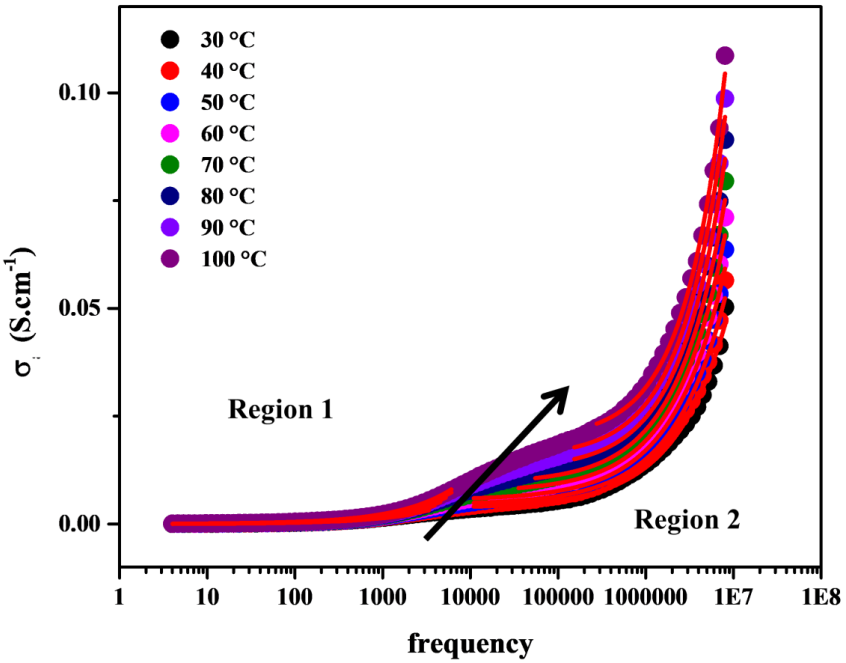

Fig 4.10 Conductivity vs frequency plot of LTZPO-0.1showing the step-like feature in a temperature range of 30 ºC to 100 ºC.

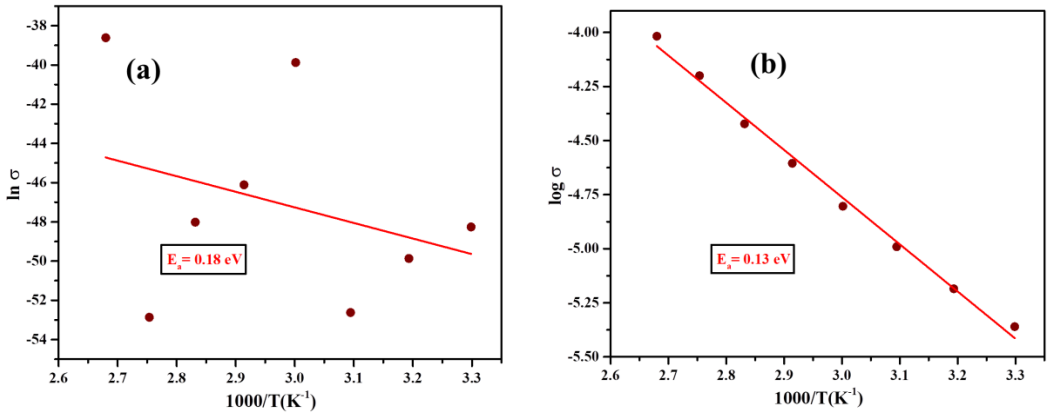

Fig 4.11 Arrhenius plot of dc conductivity of (a) region 1 (b) region 2 of LTZPO

Table 4.3 Conduction mechanism parameters of regions R1 and R2

T (°C)	σdc (R1) / S/cm	A (R1)	s (R1)	σdc (R2) / S/cm	A (R2)	s (R2)
30	1.1×10^{-21}	1.9×10^{-5}	0.65	4.7×10^{-3}	4.3×10^{-8}	0.89
40	2.2×10^{-22}	1.8×10^{-5}	0.63	5.6×10^{-3}	4.7×10^{-8}	0.88
50	1.4×10^{-23}	1.6×10^{-5}	0.61	6.8×10^{-3}	4.1×10^{-8}	0.88
60	4.8×10^{-18}	1.4×10^{-5}	0.58	8.2×10^{-3}	3.9×10^{-8}	0.82
70	9.4×10^{-21}	1.2×10^{-5}	0.56	1.0×10^{-2}	3.0×10^{-8}	0.80
80	1.4×10^{-21}	1.0×10^{-5}	0.53	1.2×10^{-2}	2.1×10^{-8}	0.85
90	1.1×10^{-23}	9.0×10^{-6}	0.51	1.5×10^{-2}	1.4×10^{-8}	0.88
100	1.7×10^{-17}	8.0×10^{-6}	0.48	1.8×10^{-2}	1.1×10^{-8}	0.89

3.2.4 Electrical Characterizations

3.2.4.1 Chrono Amperometry

Chronoamperometry plot of the LTZPO-0.1 pellet is shown in Fig. 4.12, and it is used to calculate the electronic conductivity of the electrolyte using equation 2.22 (Chapter 2, section 2.5.1). Two hours of constant voltage input on the pellets yields the steady state current of 2.48×10^{-6} mA, resulting in the total electronic conductivity of 0.3×10^{-8} S cm^{-1} for the ceramic solid-state electrolyte. Such low electronic conductivity shows the possibility of long cyclability of the electrolyte in Li|Li symmetric cells, which further motivates us to evaluate it electrochemically.

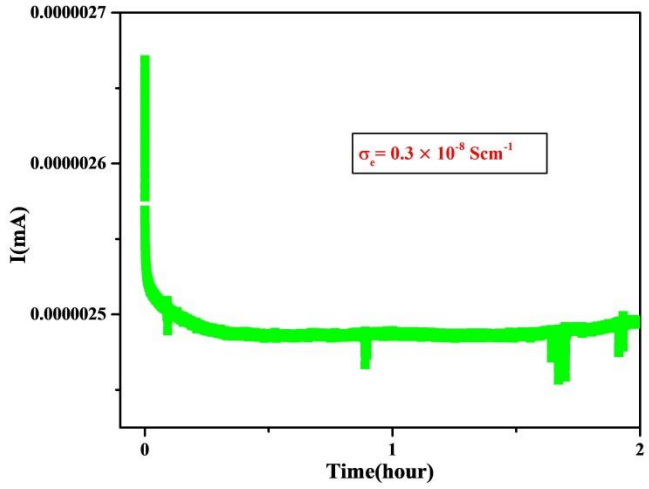

Fig 4.12 Chronoamperometry curve of LTZPO-0.1 sample at a applied voltage of 0.1 V for 2 hours.

3.2.5 Electrochemical Performance Analysis of $LiTa_2PO_8$ Solid State Electrolyte

3.2.5.1 Electrochemical Impedance Spectroscopy (EIS) Analysis

Li|Li symmetric cell had been assembled in a CR2032 coin cell by employing polypropylene soaked $LiPF_6$ buffer layer (BF) at electrode/electrolyte interface, this configuration enhances the charge transfer dynamics and overall conductivity of the symmetric cell as discussed in the previous chapter 3 section 3.2.5.1. Figure 4.13 shows the Electrochemical impedance spectroscopy (EIS) spectra of Li|BF|LTZPO-0.1|BF|Li symmetric cells before and after cycling for 1500 h. The buffer layer serves as a bridge between LTZPO and Li metal, and also minimises the chemical reduction of LTZPO, and improving wettability and contact. EIS spectra show the variation of the total impedance of the symmetric cell before and after cycling. EIS profile shows that the total impedance of the cells increases from ~200 ohms to ~300 ohms after cycling for

1500h, accompanied by a moderate increase in the overpotential after cycling of 1500 h. Such behavior is consistent with reports for decomposition of $LiPF_6$ liquid electrolyte present at the interface and the formation of a highly resistive layer and formation of LiF/Li_3PO_4 that hinders the Li-ion motion in the symmetric system LiF or Li_3PO_4 composite phases [139].

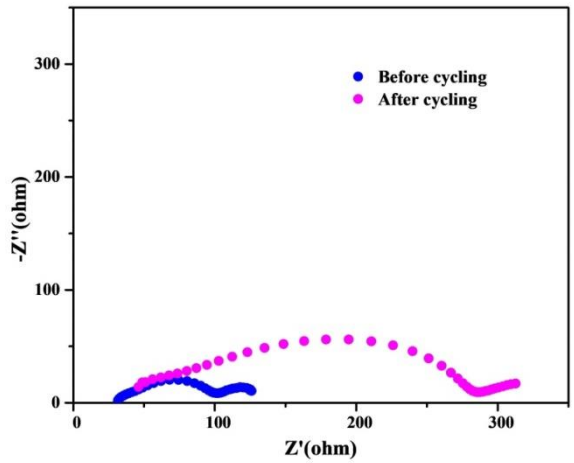

Fig,4.13 Electrochemical impedance spectroscopy curve LTZPO-0.1symmetric cell.

3.2.5.2 Galvanostatic Charge-Discharge (GCD) Analysis

Figure 4.14 shows the Li-ion stripping/plating in Li|LTZPO|Li cell operated at a current density of 100 uA cm^{-2} shows that the ionic transport over the Li/LTZPO interface was little unstable resulting into stable interface formation and then it cycled upto 1500 h with minimal overpotential of ~0.04 V. This type of ionic transport across the interface caused by the fast ionic conduction found in LTZPO-0.1 sample stabilized with liquid electrolyte buffer layer.

The LTZPO-0.1 quasi-solid-state battery is assembled in a CR2032 coin cell using the buffer layer on the interfaces of the solid-state electrolyte. Figure 4.15 shows the voltage

vs specific capacity curve quasi-solid state cell; its charging/discharging capacities calculated are 120 mAh g^{-1} and 88 mAh g^{-1}, respectively. Figure 4.16 shows that after 20 cycles, the cell shows a stable charge capacity of mAh g^{-1} and discharge capacity of 81 mAh g^{-1} with the efficiency of ~99%.

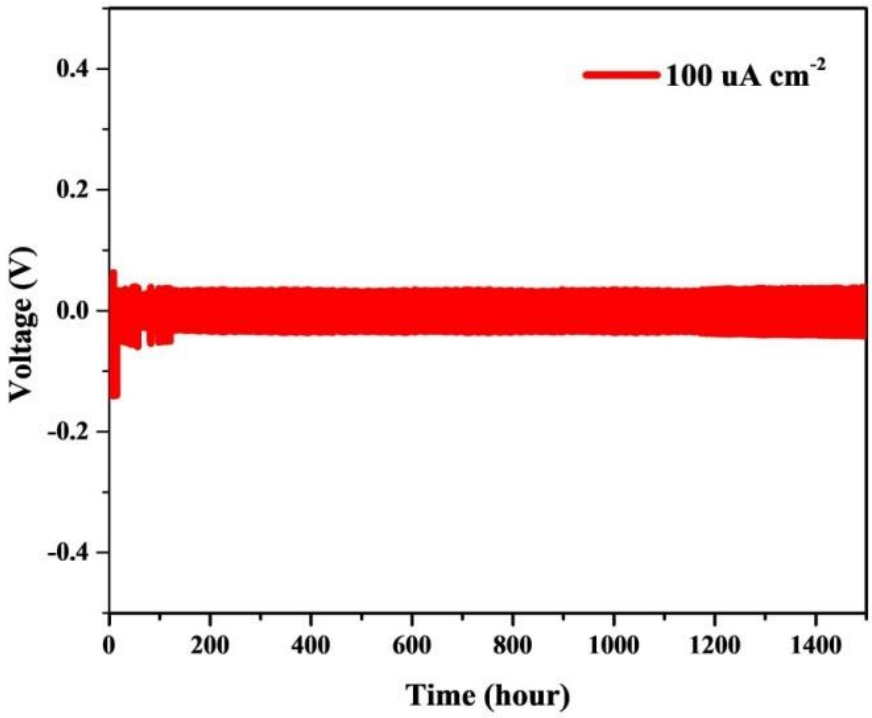

Fig 4.14 Charge-discharge profile of LTZPO-0.1 symmetric cell at a current density of 0.1mAcm^{-2}.for 1500 h

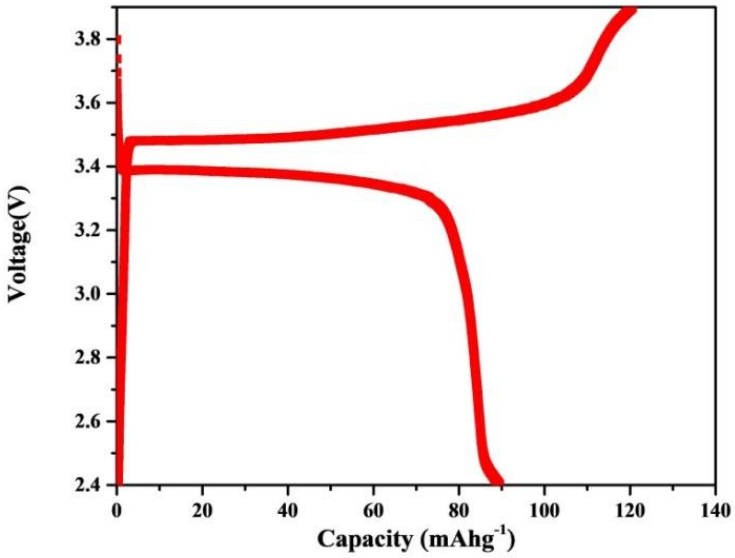

Fig 4.15 Charge/discharge profile of LTZPO-0.1 quasi-solid-state battery

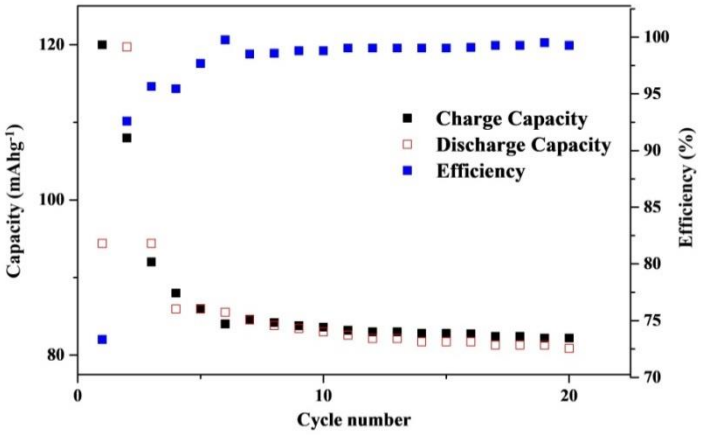

Fig 4.16 capacity, efficiency vs. cycle number of LTZPO-0.1 quasi-solid-state battery

In summary, LTZPO solid electrolyte was synthesized via solid-state reaction route with Zr concentration varying as 0, 0.1, 0.2, 0.3 at Ta site in LTPO. XRD analysis confirmed

the formation of the monoclinic LTZPO and secondary $LiTa_3O_8$ phase. LTZPO exhibited high relative density ~87% with dense microstructure, heterogeneous grain distribution when subjected 500 rpm milling prior to sintering. Dielectric studies revealed Maxwell-Wagner relaxation. Impedance analysis identified two distinct relaxation process corresponds to two different semi-circular arcs originating from grain and grain boundary contributions, further validating the Maxwell-Wagner relaxation mechanism. The conductivity study indicated two conduction mechanisms, governed by the CBH and OLPT models, clarifying the role of grains and grain boundaries in charge transport with the value of ionic conductivity as 0.24×10^{-4} S cm^{-1}. A quasi-solid-state battery demonstrated an initial discharge capacity of 88 $mAhg^{-1}$, retaining 81 $mAhg^{-1}$, with a efficiency of 99%.

Chapter 5

Structural and Grain Boundary Impedance Analysis of Ce doped $Li_7La_3Zr_2O_{12}$ Solid Electrolyte

This chapter includes the structural and impedance analysis of Ce-doped Li7La3Zr2O12 (LLZCO) solid electrolyte. The detailed impedance deconvolution has been carried out to separate bulk, grain-boundary, and electrode interface contributions, allowing a clearer interpretation of relaxation processes influencing lithium-ion conduction. Electrochemical analysis revealed that the symmetric cell and full cell show the stability of potential for 700 hours and discharge capacity of ~119 mAh g^{-1}after 20 cycles.

5.1 Introduction

28

$Li_7La_3Zr_2O_{12}$ (LLZO) has attracted significant attention due to its relatively high room-temperature ionic conductivity and excellent chemical stability. However, the practical deployment of LLZO-based electrolytes remains constrained by challenges such as high grain-boundary resistance, interfacial polarization, and processing-induced secondary phase formation, all of which critically influence the overall ionic transport and electrochemical performance [140-143]. Doping strategies and optimized sintering protocols have been widely employed to stabilize the highly conductive cubic phase of LLZO and to improve its densification behavior. In particular, isovalent Ce^{4+} substitution at the Zr^{4+} site has been shown to induce lattice expansion and local structural distortions, suppressing long-range lithium ordering and favoring fast Li-ion transport. In our earlier work, a multi-step sintering approach was demonstrated to be effective in enhancing the density, microstructural uniformity, and ionic conductivity of Ce-doped LLZO (LLZCO). Although such processing optimization improves bulk transport properties, grain boundaries and interfacial regions often remain dominant resistive components, limiting the achievable performance in solid-state and quasi-solid-state battery configurations [144].

Electrochemical impedance spectroscopy (EIS) is a powerful tool for probing ion transport in solid electrolytes; however, conventional equivalent circuit fitting frequently suffers from ambiguity due to overlapping relaxation processes and non-unique circuit solutions. To overcome these limitations, the distribution of relaxation times (DRT) method has emerged as a robust, model-independent approach that enables

deconvolution of impedance spectra into distinct relaxation processes associated with bulk conduction, grain-boundary transport, space-charge effects, and electrode/electrolyte interfacial polarization. By providing a direct link between microstructural features and specific impedance contributions, DRT analysis offers deeper mechanistic insight into ionic transport pathways in complex ceramic electrolytes.

This chapter builds upon the optimized synthesis and processing framework of Ce-doped LLZO and focuses on a quantitative resolution of grain-boundary and interfacial impedance using DRT analysis. By correlating structural (XRD), microstructural (SEM), and electrochemical characteristics with DRT-resolved relaxation processes, this chapter aims to establish a comprehensive structure-transport-performance relationship for LLZCO.

Synthesis of Ce-doped $Li_7La_3Zr_2O_{12}$ ceramics was carried out via a solid-state route as mentioned in Chapter 2, Section 2.1.1.3. Moreover, physiochemical, electrical, and electrochemical characterizations of Ce-doped $Li_7La_3Zr_2O_{12}$ material are performed and explained in Chapter 2, Section 2.4-2.5.

5.2 Result and Discussions

5.2.1 Thermogravimetric Analysis (TGA) and Differential Scanning Calorimetry (DSC) Analysis

The Phase formation and sintering temperature of the LLZCO ball-milled product of the precursors was examined via TGA/DSC, shown in Fig. 5.1 TGA shows multi-stage mass loss has occurred, initially 0.84% mass loss depicts the removal of moisture and reaction

with La_2O_3 to form $La(OH)_3$. Further mass loss of 2.01% and 2, 25% accompanying with endothermic peaks at 335 ºC and 450 ºC, can be attributed to La_2O_3 decomposition into LaOOH and LaOOH reaction with CO_2, respectively [145]. Final mass loss of 17.44% starts from 700 ºC, which shows Li_2CO_3 decomposition has started [146], and LLZCO, which leads to the formation of LLZCO. It can be seen that above 1050 ºC mass loss is negligible, therefore 1150 ºC and 1100 ºC are considered for sintering temperature of material.

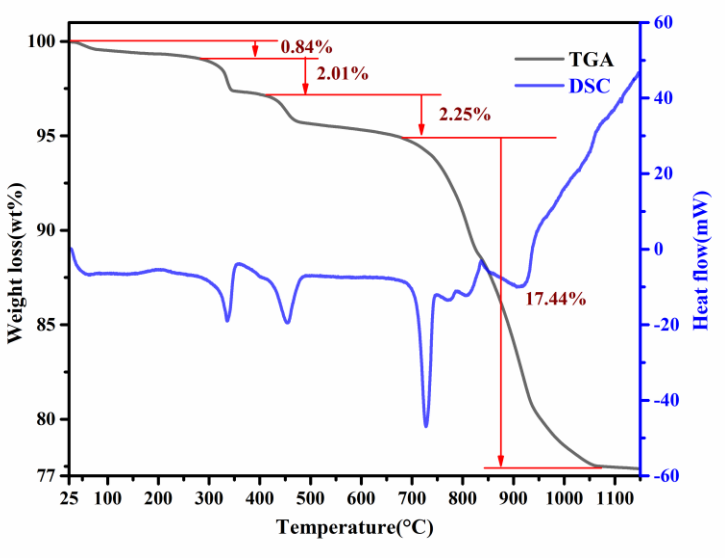

Fig. 5.1 TGA/DSC curve of ball-milled product up to 1150 ºC

5.2.2 Structural Analysis and Morphological Analysis

5.2.2.1 X-ray Diffraction (XRD) Analysis

Figure 5.2 shows the structural analysis of $Li_7La_3Zr_{2-x}Ce_xO_{12}$ (x = 0, 0.125, 0.25, 0.75, 0.5). Figure 5.2 clearly indicate the transition of phase as the concentration of Ce doping is increased in the LLZO lattice, diffractogram of sample T3 ($Li_7La_3Zr_{1.75}Ce_{0.25}O_{12}$) indicates the dominance of the cubic garnet LLZO and confirmed with Rietveld analysis

(χ^2= 5.04) as shown in fig.5.3 using the Wyckoff positions given in table 5.1 and micro-strain of 3.4 x 10^{-4} as estimated from W-H plot showed in fig. 5.4. Cubic garnet structure is a well-established high Li-ion conductivity polymorph due to its partially disordered lithium sublattice, which provides a three-dimensional network of interconnected tetrahedral and octahedral sites that enable ultrafast Li-ion migration at room temperature. However, closer inspection of the XRD pattern also reveals the presence of minor secondary phase peaks. This additional minor reflection can be assigned to Ce-rich intermediate oxide phases $Ce_{0.8}La_{0.2}O_{1.9}$ (2.3%) during high-temperature sintering, and it suggests that at high temperature, the solubility limit of Ce in the garnet lattice exceeds the partial expulsion of Ce dopants and subsequent nucleation of separate crystalline phases [147]. This is a well-known challenge in doped LLZO systems, where the beneficial effect of doping on stabilizing the cubic phase must be carefully balanced against the risk of undesired phase segregation that compromises the ionic conductivity. Unlike the high ionically conductive cubic LLZO matrix, the Ce-rich intermediate phases tend to be a slower ionic conductor, and their presence during sintering introduces the ion blocking behavior if they localize at the grain boundaries or triple junctions [147]. The XRD results are shown in the Fig. 5.2 suggests a fundamental trade-off inherent in the Ce-doping strategy in LLZO, as low doping levels can effectively stabilize the high conductivity cubic phase and reduce intrinsic Li-ion vacancy concentration. Hence, the excessive doping leads to the phase separation that can create insulating regions and degrade overall performance.

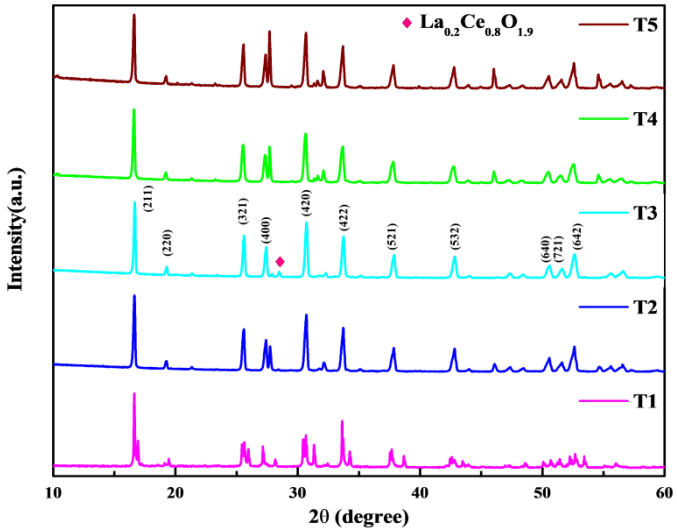

Fig. 5.2 XRD pattern of Ce-doped LLZO at different concentration ($Li_7La_3Zr_{2-x}Ce_xO_{12}$; x = 0, 0.125, 0.25, 0.75, 0.5) along with presence of $Ce_{0.8}La_{0.2}O_{1.9}$ marked in the XRD pattern of sample T3.

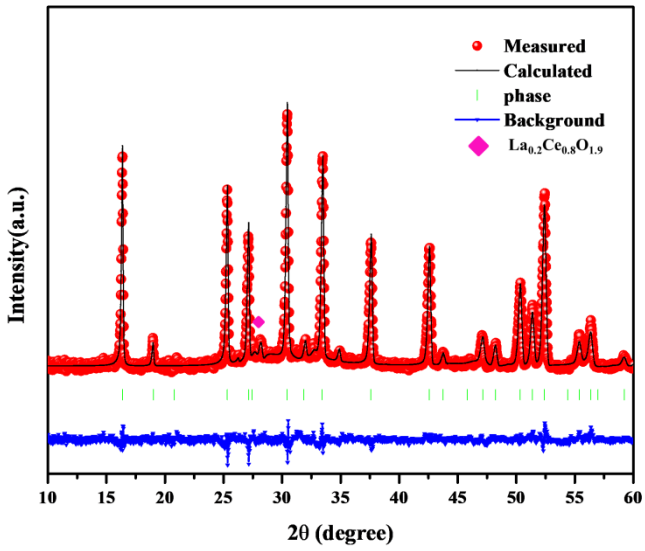

Fig 5.3 Rietveld refinement pattern of sample T3

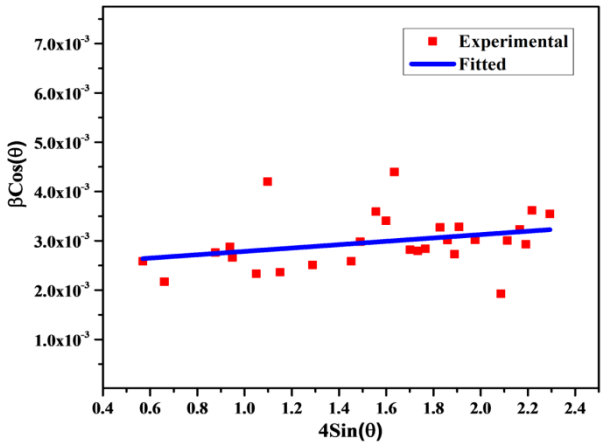

Fig 5.4 Williamson Hall plot of sample T3

Table 5.1 Rietveld refinement parameters of sample T3

Element	X	Y	Z	Occ
Li1	-0.125	0.00	0.25	0.98
Li2	-0.30	0.10	0.137	0.97
Zr	0.00	0.00	0.00	0.877
Ce	0.00	0.00	0.00	0.123
La	0.00	0.25	0.125	1
O	-0.03	0.05	0.15	0.95

5.2.2.2 Density Analysis

Density was taken as the primary parameter to evaluate the effectiveness of the sintering schedules and to establish an optimized processing window for Ce-doped LLZO. Based on the TGA/DSC analysis, which indicated negligible mass loss beyond ~1050–1100 °C,

a series of step-sintering schedules was designed to balance densification and lithium volatization. Accordingly, two distinct step-sintering strategies were explored: (i) an initial high-temperature at 1150 °C followed by holding at 1100 °C for varying durations (Schedule-1) and (ii) sintering at 1200 °C followed by a lower-temperature at 1170 °C (Schedule-2). The relative density values obtained for different sintering conditions are in Table 5.2.

Within Schedule-1, sample T2 (1150 °C for 2 h followed by 1100 °C for 4 h) exhibited the highest relative density of ~65%, indicating effective grain rearrangement during the multi-step thermal treatment. In contrast, Schedule-2 demonstrated a more pronounced improvement in densification, with sample T6 (1200 °C for 2 h) achieving the maximum relative density of ~79%. The enhanced densification in this schedule can be attributed to controlled grain growth at reduced thermal stress, which suppresses excessive lithium loss while promoting pore elimination. Hence, all the samples (T1-T5) are sintered at 1200 °C for 2 h to achieve the highest density, respectively.

Table 5.2 Step sintering schedule of $Li_7La_3Zr_{1.75}Ce_{0.25}O_{12}$ sample.

S.no	**Sample ID**	**Sintering Treatment**	**Relative Density(%)**
1.	Q1	1150 ºC for 2 h and 1100 ºC for 2 h	44
2.	Q2	1150 ºC for 2 h and 1100 ºC for 4 h	65
3.	Q3	1150 ºC for 2 h and 1100 ºC for 6 h	61
4.	Q4	1150 ºC for 2 h and 1100 ºC for 8 h	57

5.	Q5	1100 ºC for 10 mins	66
6.	Q6	1200 ºC for 2 h	79
7.	Q7	1200 ºC for 2 h and 1170 ºC for 2 h	72
8.	Q8	1200 ºC for 2 h and 1170 ºC for 4 h	54
9.	Q9	1200 ºC for 2 h and 1170 ºC for 6 h	46
10.	Q10	1200 ºC for 2 h and 1170 ºC for 8 h	40

8

5.2.2.3 Scanning Electron Microscopy (SEM), Tunneling Electron Microscopy (TEM), and Energy Dispersive X-ray Spectroscopy (EDX) Analysis

Figure 5.5 shows the TEM images of the T3 powder sample, showing the homogeneous distribution of elements all over the particle. The cross-sectional SEM analysis of the fractured pellet of sample T3 is shown in fig. 5.6 (a-c) at different magnifications, SEM analysis provides essential micro-structural context that complements the phase information estimated by XRD. Figure 5.6 (a) shows SEM images of T3 at 1KX magnification, describing densely sintered ceramic with well-developed grains. This morphology is consistent with effective densification required to minimize porosity and maximize bulk conductivity. However, higher magnification images displayed in Fig. 5.6 (a,b) at 2.5 KX and 5 KX, respectively, reveals the subtle but important feature at the grain boundaries, which display a flaky or layered morphology at or near grain boundaries [148]. Flaky structures are consistent with thin intergranular films morphology and segregated phases that can develop during sintering when local supersaturation of dopants drives expulsion and accumulation at grain boundaries.

Figure 5.6 (d,e) shows the EDS analysis of sample T3; EDS mapping corroborates this interpretation while showing uniform distribution of La, O, Zr, and Ce consistent with the LLZO matrix. The phenomenon of intergranular segregation is a classic feature in doped ceramic systems and is particularly well documented in garnet-type electrolytes. They may also contribute to space-charge regions characterized by local depletion of mobile Li-ion and an elevated electrostatic potential barrier that further resists the ionic transport. Hence, the chemical inhomogeneity and the probable resistive boundaries can increase the total impedance [149-151].

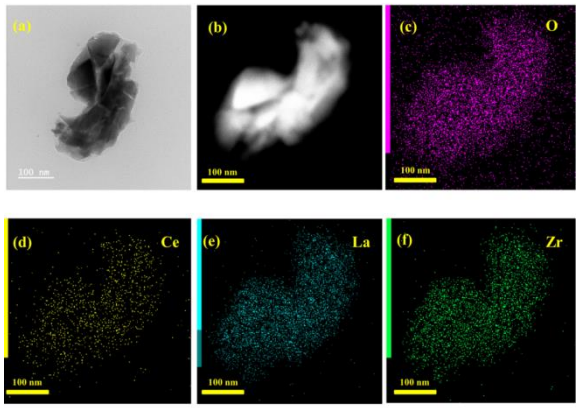

Fig.5.5 (a)TEM image of sample T3 powder at 100 nm, Elemental distribution and mapping (c) O, (d) Ce, (e) La, (f) Zr

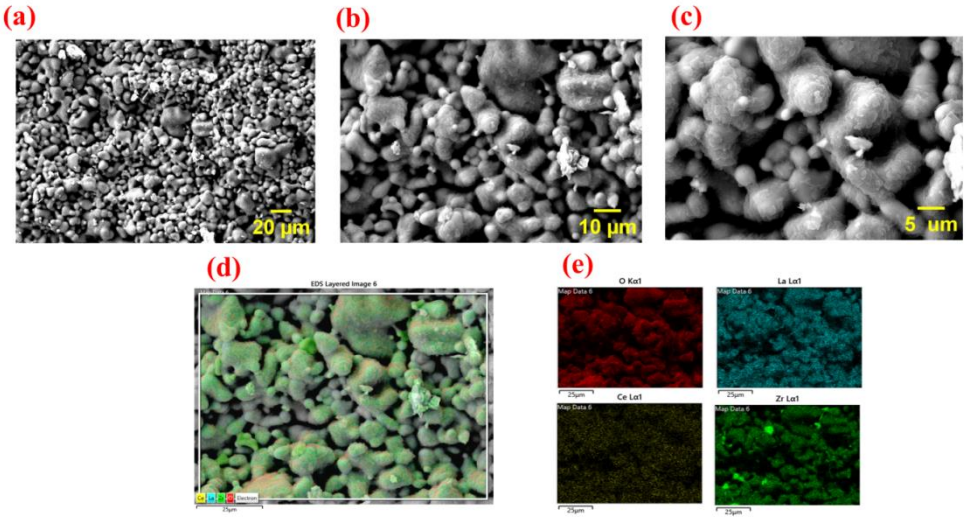

Fig 5.6 SEM micrograph of sample T3 at (a) 1 KX (b) 2.5 KX (c) 5 KX, (d,e) elemental mapping of sample T3

5.2.3 Impedance Characterization

5.2.3.1 Impedance Spectroscopy and Distribution of Relaxation Times (DRT) Analysis

Impedance analysis is crucial for resolving the total resistance experienced Li-ion during charging and discharging but the best way to resolve the physical processes taking due to crystal structure and microstructure heterogeneities inside the material, therefore predicting the electrical equivalent circuit to predict the correct value of resistance is still the crucial part of research for battery scientist, chapter 3 and 4 describes the way to predict the circuit by considering the relaxation times provided by peak maxima of loss tangent curves but there can be the possibility of other relaxation corresponding to different processes had merged in a single broad peak. Therefore, deconvolution impedance spectra are required. DRT analysis of impedance provides essential

quantitative insights into how these features, as explained through XRD and SEM results, may impact the ionic transport. Figure 5.8 shows the impedance spectra of samples T1-T5, and the temperature-dependent (30-90 °C) impedance spectra of sample T3 are shown in fig 5.7 (a), respectively. Sample T3 expected to show the lowest grain resistance as shown in the inset of Fig. 5.8 and Fig. 5.7 (a) results reveal the reduction of total resistance with increasing temperature. Unlike traditional equivalent circuit fitting of impedance data that risks conflating physically distinct relaxation processes, distribution of relaxation times (DRT) analysis deconvolutes the impedance spectrum and shows the separated relaxation times that correspond to a specific physical process in the material. Hence, each peak in the DRT graph is considered as one –RC- circuit taking in consideration of brick layer model [153]. The temperature- dependent (30-90 °C) DRT spectra analysis of sample T3 consistently resolves the seven distinct peaks spanning approximately 10^{-7} to 10^{0} sec as shown in Fig. 5.7 (b). Each peak can be interpreted in light of the XRD and SEM observation to build a detailed and unified model of ionic conduction behavior in the material. The origination of multiple peaks in the DRT plot can be attributed to the grain boundary inhomogeneity and dopant segregation in LLZO solid electrolytes system comprising the broad peaks corresponding to the bulk, grain boundary and electrode effects [154]. Based on the frequency dependence of grain as deiscussed in previous chapters, three peaks are observed at nearly about 10^{-7} s (P1), 10^{-6} s (P2) and 10^{-5} s (P3), P1 corresponds to intrinsic bulk conduction pathway within the grains and these time-scales reflects ultrafast Li-ion hopping across tetrahedral and octahedral sites in partially disordered

garnet structure [155,153]. P2 is at slightly lower intensity and likely to reflect minor local distortion or anti-site defects introduced by Ce doping, but remains fundamentally a bulk conduction feature [153,155]. P3 nearly at 10^{-5} s represents the nanoscale inhomogeneity and intergranular sub-boundary and Maxwell-Wagner polarization effects [156-158].

Most critically, the fourth(P4) peak clearly represents the signature of grain boundary impedance and space charge layer phenomenon; this presence aligns with the $Ce_{0.8}La_{0.2}O_{1.9}$ secondary phase in XRD and flaky morphology in SEM [153,154,156-157]. The fifth and sixth peaks represent the electrode polarization that can represent the fast and slow polarization of the electrode according to the frequency range. P7 (10^{-1} s) peaks correspond to the electrode/electrolyte interface polarization arising from capacitive ionic accumulation and slow diffusion related process governed by the blocking nature of electrode, respectively [155-157]. In contrast, the fitted impedance plot of sample T1 corresponding to undoped LLZO is shown in Fig. 5.10 and the origin of various resistances in T1 possessing a tetragonal phase were also analyzed via DRT, exhibiting a qualitatively similar set of relaxation features but with markedly different physical origins and magnitudes shown in Fig. 5.11. Owing to its fully ordered Li sublattice and absence of intrinsic Li vacancies, tetragonal LLZO shows two slow bulk relaxations (P1–P2) associated with collective, synchronous Li migration across the 8a/16f/32g network, in agreement with structural refinements reports and first-principles simulations demonstrating cooperative six-ion hopping with elevated activation barriers [160]. The intermediate shoulder (P3) is attributed to Maxwell–Wagner-type polarization

arising from grain orientations and elastic contrast, rather than chemical heterogeneity. Most importantly, the grain-boundary peak (P4) is significantly larger in tetragonal LLZO due to its intrinsically restricted inter granular percolation pathways, even in the absence of secondary phases [161]. The low-frequency peaks (P5–P7) remain characteristic of interfacial polarization at Au electrodes but shift to longer relaxation times because the tetragonal framework imposes inherently slower overall Li-ion dynamics. These combined results establish a direct, mechanistic link between Li-sublattice order, phase symmetry, and the hierarchy of relaxation processes governing ion transport in LLZO. Here, the area under the curve of DRT peaks expresses the resistance value involved in each physical process in the material and is used to calculate the capacitive value of that particular process at the corresponding relaxation time to design the parallel-RC-circuit. The equivalent circuit model has been prepared from the DRT spectrum of samples T3 and T1 (shown in tables 5.3 and 5.4) using 7 –RC- circuits in series, and shown in the inset of Fig 5.7 (c) concluding the total conductivity of T3 and T1 as 0.5×10^{-4} S/cm 7.21×10^{-7} S/cm respectively and the capacitive values from fitted circuits further supports the possible origin of different peaks in DRT plot [153].

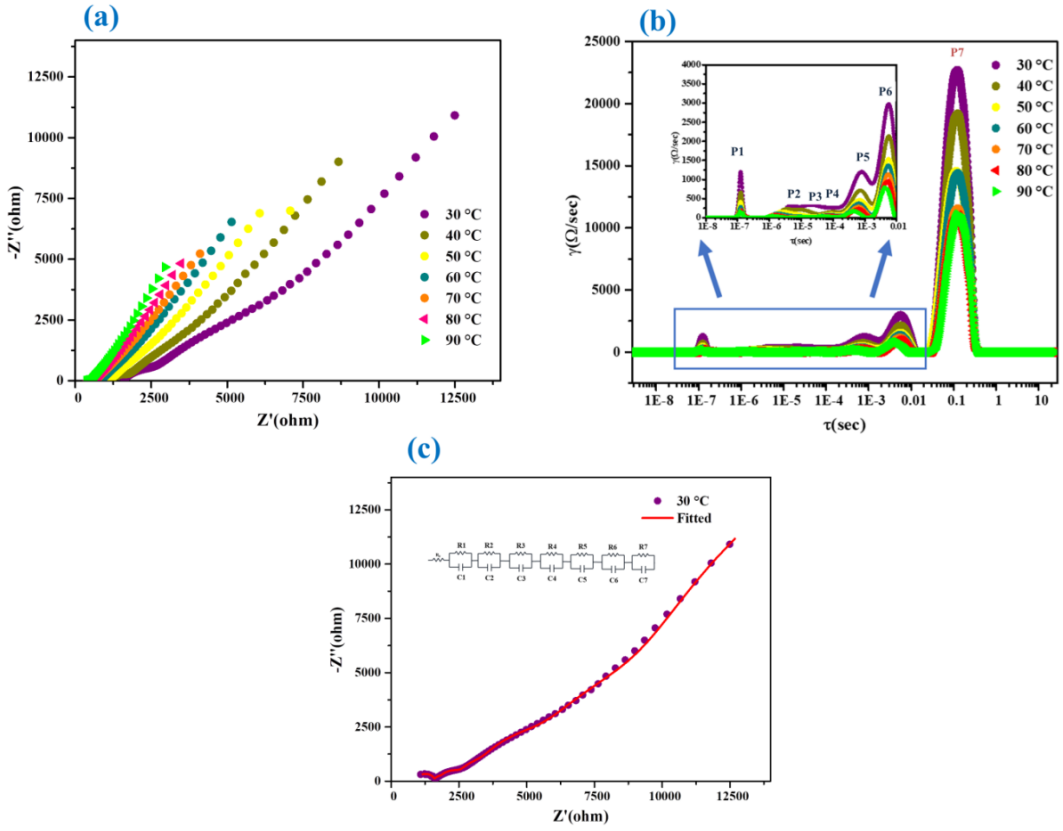

Fig 5.7(a) Impedance spectra of sample T3 from 30 °C to 90 °C (b) Distribution of Relaxation Times analysis of sample T3 from 30 °C to 90 °C (c) Fitted impedance spectra of sample T3alomg with fitting circuit in the inset of graph.

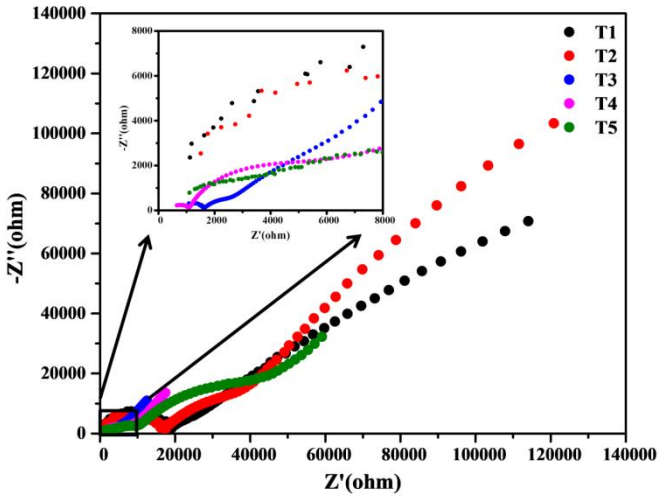

Fig 5.8 Impedance spectra of sample T1-5 at room temperature

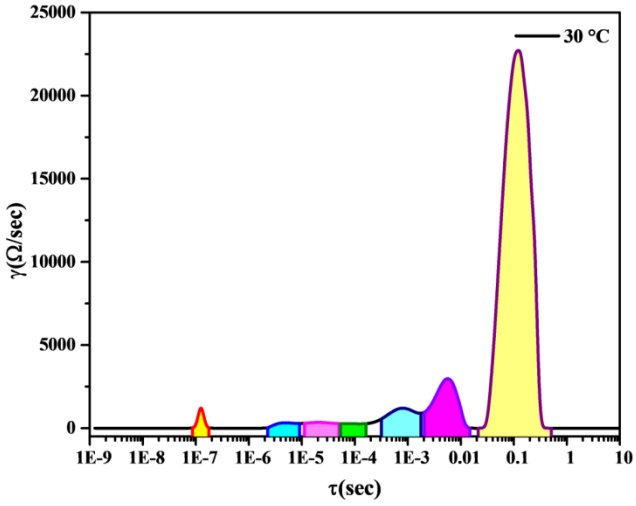

Fig. 5.9 DRT analysis of T3 at 30 °C showing particular peaks

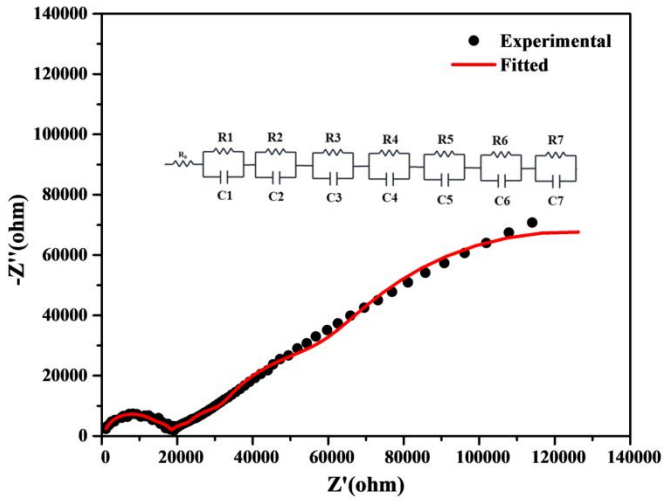

Fig 5.10 Impedance plot of tetragonal LLZO sample T1 at room temperature

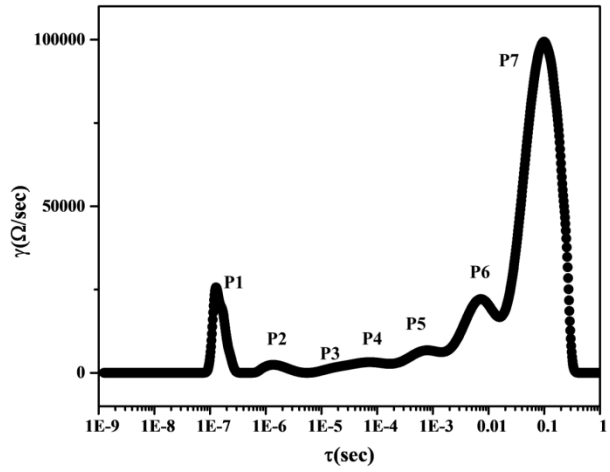

Fig. 5.11 DRT Spectra of sample T1 at room temperature

Table 5.3 Circuit fitted parameters of sample T3

Parameter	Value
R0	929 ohm

R1	373 ohm
R2	340 ohm
R3	794 ohm
R4	314 ohm
R5	1195 ohm
R6	3657 ohm
R7	32588 ohm
C1	~10^{-11} F
C2	~10^{-09} F
C3	~10^{-09} F
C4	~10^{-08} F
C5	~10^{-08} F
C6	~10^{-07} F
C7	~10^{-07} F

Table 5.4 Circuit fitted parameters of sample T1

Parameter	Value
R0	409 ohm
R1	71280 ohm
R2	11947 ohm
R3	35032 ohm

R4	5313 ohm
R5	11959 ohm
R6	5190 ohm
R7	1.43E5 ohm
C1	~10^{-12} F
C2	~10^{-11} F
C3	~10^{-09} F
C4	~10^{-08} F
C5	~10^{-07} F
C6	~10^{-07} F
C7	~10^{-06} F

5.2.4 Electrical Characterization

5.2.4.1 Chronoamperometry

The chronoamperometry curve of the LLZCO is displayed in Fig 5.12, and it is used to calculate the electronic conductivity of the electrolyte using equation 2.22 (Chapter 2, Section 2.5.1). After four hours of constant voltage input, the LTPO ceramic sample exhibits a very low I_{SS} of 5.24 $\times 10^{-6}$ mA, which results in a negligible electronic conductivity (σ_e) of 1.00 $\times$ 10^{-8} S cm^{-1} for the LTPO ceramic solid-state electrolyte. Lower values of σ_e are very crucial for battery applications, as high σ_e can favour the dendrite formation in Li-ion batteries, which results in short circuiting of the battery, decrease in coulombic efficiency, and leads to capacity loss

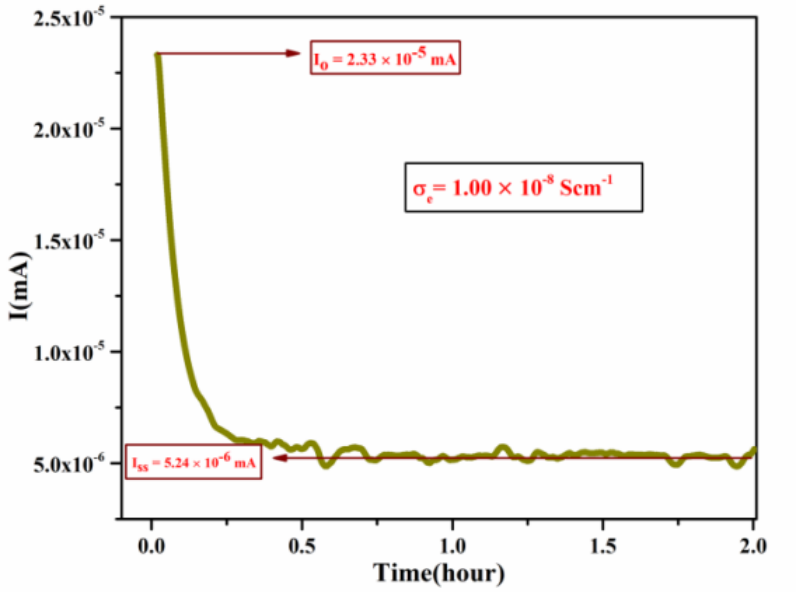

Fig 5.12 Chronoamperometry of LLZCO pellet

5.2.5 Electrochemical Performance Analysis of Ce-doped $Li_7La_3Zr_2O_{12}$ Solid State Electrolyte

5.2.5.1 Electrochemical Impedance Spectroscopy (EIS) Analysis

The electrochemical performance of the sintered LLZCO sample T3 pellet was further evaluated in a Li|Li symmetric cell with $LiPF_6$ as an ion initiator at the interface. Figure 5.13 demonstrates a significant reduction in interfacial resistance. To ensure that ceramic is a part of Li-ion kinetics in quasi-solid state system and the requirement of interface engineering in a solid state cell, two different full cell configurations have been assembled in CR2032 coin cells, one with $LiPF_6$ liquid electrolyte at the electrode/electrolyte interface and the other without LiPF6.

Figure 5.13 shows the EIS spectrum of the cell with/without $LiPF_6$. Dry cell (without $LiPF_6$) exhibits very high bulk and interfacial resistance, confirming poor charge-transfer kinetics at both the Li|LLZCO. Whereas, when a minimal amount of $LiPF_6$ (5-10 µL) electrolyte is introduced only at these interfaces, a substantial reduction in total resistance from ~2500 ohms to ~600 ohms is seen in the EIS plot, which indicates reduced interfacial and overall impedance.

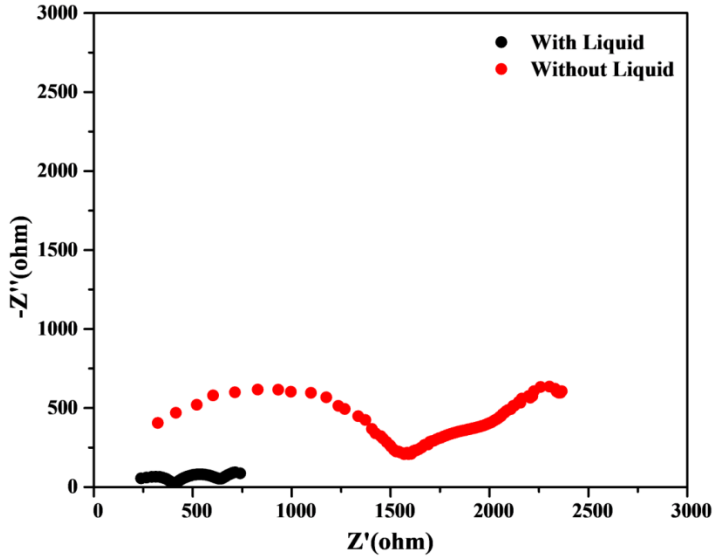

Fig.5.13 EIS spectra of full cell with Liquid electrolyte and without liquid electrolyte at the electrode/electrolyte interface

5.2.5.2. Galvanostatic Charge-Discharge (GCD) Analysis

The electrochemical performance of the sintered LLZCO sample T3 pellet was further evaluated in a Li|Li symmetric cell and a full cell in a CR2032 coin cell. Figure 5.14(a) demonstrates a significant reduction in interfacial resistance, as reflected in a markedly

lower polarization voltage of approximately ~0.04 V sustained over 700 h and shows the critical current density of ~170 μA/cm^2 as calculated from critical current density analyses shown in Fig.5.15. The Cyclic Voltametry (CV) analysis of the LLZCO sample is attempted to test the electrochemical stability and feasible working range for electrolyte in a battery using SS|LLZCO|Li cell configuration, where SS (inert electrode) is used as the working electrode, and Li chips are taken as the reference electrode. Figure 5.16 shows the CV curve ranging from -0.5 to 4 V at a scan rate of 0.5 mV/s. Peaks observed at -0.5 V and 1 V correspond to Li plating and stripping, respectively. The broadening of peaks can be explained as an additional redox process taking place due to cerium, Ce_4O_7 formation due to reaction at the interface, or insertion of excessive Li in the electrolyte structure, shown by broadening of the peak [162]. Furthermore, curve shows that there is no other extra oxidation peak from 2.5 V to 4 V, which indicates that LLZCO has a stable electrochemical window to lithium metal. To further elucidate the role of the interfacial liquid layer, $LiFePO_4$|LLZCO|Li cells were first cycled in the absence of liquid electrolyte, as shown in Fig. 5.17, the cell delivers only ~25 mAh/g during discharge. Low discharge capacity demonstrates that the high interfacial impedance inhibits stable electrochemical operation, although ionic motion through the LLZCO pellet is still evident. Figure 5.18, 4(b) shows the $LiFePO_4$ quasi-solid-state battery ($LiPF_6$ at interface) operated at 0.1C between 2.8-3.8 V. After 24 cycles, it gives charge/discharge capacity as 151/110 mAh/g with efficiency of 72% and successfully powered an LED (Fig 5.19).

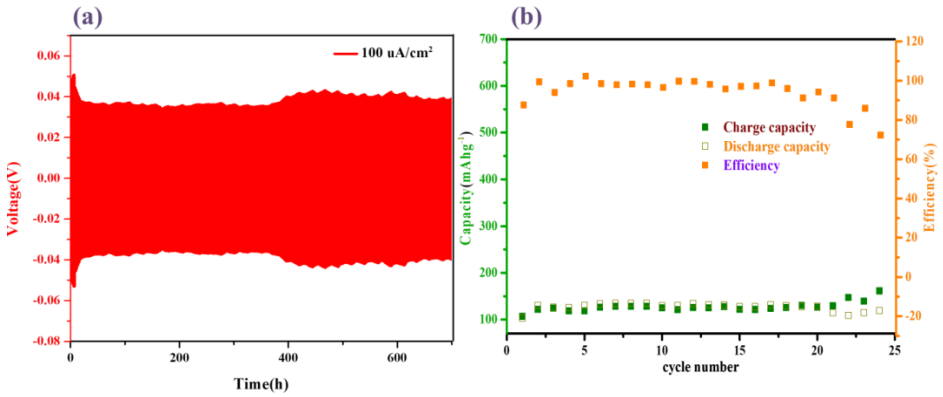

Fig 5.14 (a) Symmetric cell analysis of Sample T3 at 100 uA/cm^2 (b) Specific capacity, efficiency curve of $LiFePO_4$ quasi solid state Li metal battery up to 24 cycles

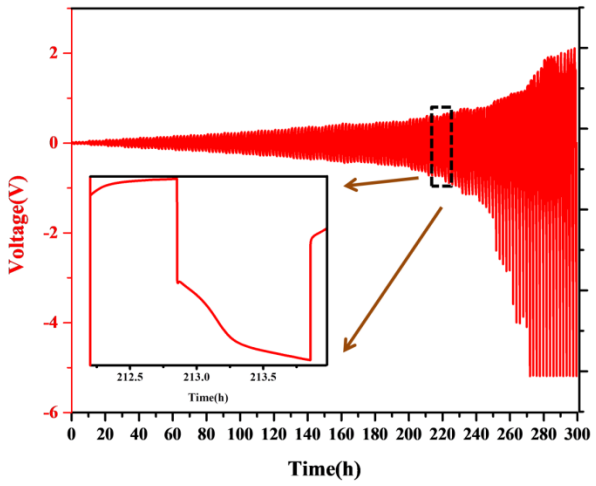

Fig 5.15 Critical current density test of LLZCO sample T3 in the range of 70 to 220 μA.cm^{-2} at the current step 5 μA.cm^{-2}

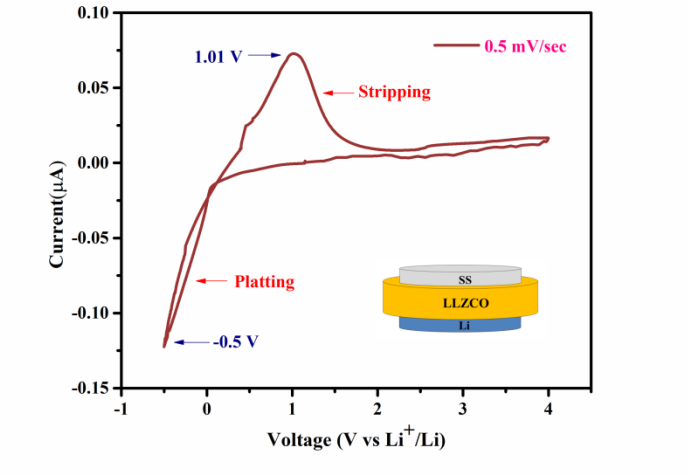

Fig 5.16 Cyclic Voltammetry analysis of LLZCO solid electrolyte in range of -0.5 V to 4 V

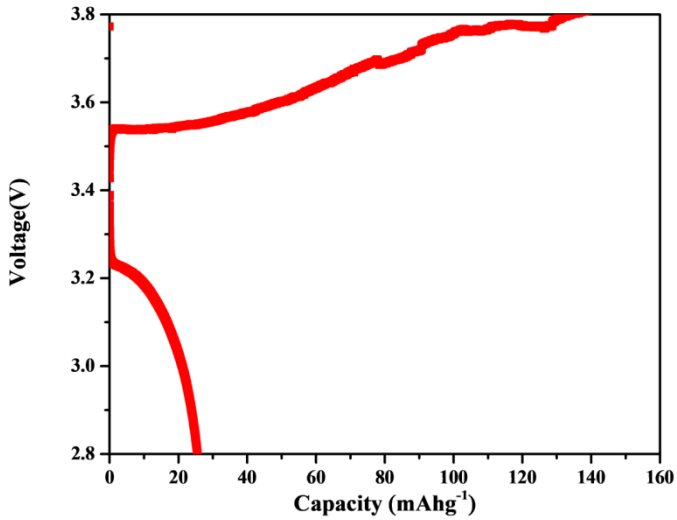

Fig 5.17 GCD graph of full cell without liquid electrolyte at 0.1C

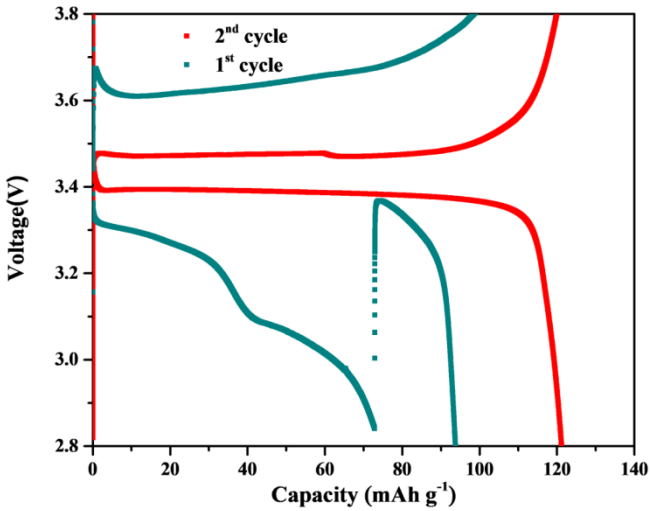

Fig 5.18 GCD graph of full cell with liquid electrolyte at the electrode electrolyte interface at 0.1C

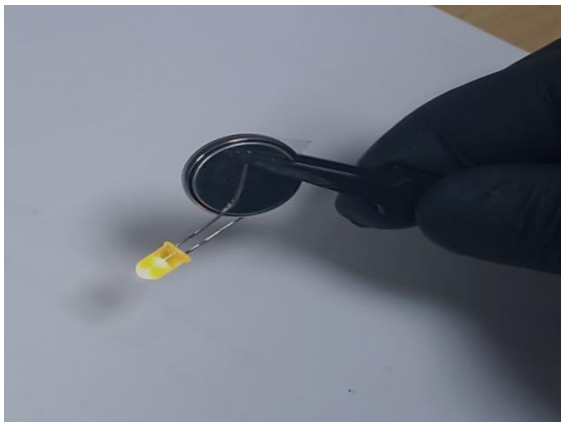

Fig 5.19 Demonstration of LED powered via cell.

In summary, DRT analysis emerges as an essential and highly valuable approach for elucidating the ionic transport mechanism in Ce doped LLZO solid state electrolyte. By rigorously deconvoluting impedance spectra into distinct relaxation processes, DRT enables precise

assignment of bulk, grain boundary and interfacial contribution across a wide time scale spectrum. In sample T3, well resolved peaks (P1-7) were identified with two fastest relaxation peaks confirming efficient bulk Li-ion transport in stabilized cubic garnet phase, intermediate four peaks were directly corelated with grain boundary and space charge impedance arising from microstructural heterogeneities. XRD analysis supported this information by revealing minor $Ce_{0.8}La_{0.2}O_{1.9}$ secondary phase, while SEM/TEM imaging identified flaky, layered feature at grain boundaries indicative of dopant oversaturation during sintering and homogeneous elemental distribution. Electrochemical testing unveils that $LiPF_6$ support the lowered overpotential value in quasi solid state lithium symmetric cell cycled for 700 h and full cell shows the efficiency of 72% after 24 cycles.

Chapter 6

LLZCO and LTZPO composite Solid State Electrolyte performance in All Solid State Batteries

This chapter investigates the electrochemical performance of LLZCO-LTZPO [(0-25%) LTZPO in LLZCO] composite solid-state electrolytes designed to improve the densification, grain-boundary characteristics, and overall ionic transport of the composite electrolyte system. SEM and DRT analyses revealed the distribution of LTZPO predominantly along grain boundaries. The all-solid-state symmetric cell has demonstrated stable cycling for 140 hours, and Full-cell testing has validated the practical applicability of the composite electrolyte by attaining a discharge capacity of 95.8 mAh g^{-1} after 80 cycles.

6.1 Introduction

All Solid-State Lithium-ion Batteries (ASSLBs) have emerged as a promising solution to the key challenges associated with liquid electrolyte-based lithium-ion batteries, including restricted operating voltage, unstable electrode/electrolyte interface, and limited cycling stability. ASSLBs employ solid-state electrolytes (SSEs) that act as a separator as well as Li ion conductor for the solid-state lithium batteries [1-3]. In recent years, ceramic electrolytes have gained much attention due to their unique advantages, such as nominal ionic conductivity, wide electrochemical potential windows, and the primary requirement of SSEs is the high ionic conductivity and electrode/electrolyte interface stability [163,164]. A ceramic-ceramic composite solid state electrolyte approach to prepare an electrolyte with multiple properties, incorporating characteristic features of both the electrolyte, can be beneficial, taking into consideration the final practical outcome as per the application. $Li_7La_3Zr_2O_{12}$-$Li_{1.3}Al_{0.3}Ti_{1.7}(PO_4)_3$ (LATP) composite was prepared by introducing LATP in LLZO ceramic, resulting in reduced sintering temperature of composite ceramic [165]. $Li_{1.4}Al_{0.4}Ti_{1.6}(PO_4)_3$(LATP)-$Li_{1.5}Al_{0.5}Ge_{1.5}(PO_4)_3$(LAGP) composite was prepared by introducing the secondary phase of LATP in the bare LAGP, resulting in enhanced ionic conductivity [166]. In this work, LTZPO concentration is varied in LLZCO ceramic electrolyte to improve the density as well as the ionic conductivity at the grain boundaries. LLZCO@LTZPO composite in different weight percent as 0%, 5%, 10%, 15%, 20%, 25% of LTZPO in LLZCO ceramic denoted as C0, C1, C2, C3, C4, C5 composite ceramic.

Synthesis of LLZCO@LTZPO composite ceramics was carried out via a solid-state route as mentioned in Chapter 2, Section 2.1.1.4. Moreover, physiochemical, electrical, and electrochemical characterizations of LLZCO@LTZPO composite material are performed and explained in Chapter 2 Section 2.4-2.5.

6.2 Results and Discussion

6.2.1 Structural and Morphological Analysis

6.2.1.1 X-ray Diffraction (XRD) Analysis

Figure 6.1 shows the XRD pattern of LTZPO and C0-C5 ceramics respectively. The diffraction profiles confirm the formation of the LLZCO primary garnet phase (space group: Ia-3d JCPDS: 01-080-6067) across all concentrations, and the magnified region near 30° is magnified to emphasize structural evolution with weight percentage variation. The characteristic reflections of LTZPO progressively intensify with increasing LTZPO (more than 10%), confirming successful incorporation of the secondary phase. The magnified inset reveals a gradual peak shift and broadening in the composite, revealing a systematic peak shift of the composite samples toward higher diffraction angles with increasing LTZPO content. Peak shift corresponds to a reduction in interplanar spacing and indicates the lattice contraction in the LLZCO. This contraction is likely caused by interfacial stress and partial ionic redistribution at the LLZCO/LTZPO boundary, which induces compressive strain in the composite structure [167]. This behavior suggests the development of interfacial strain and microstructural disorder at the LLZZCO/LTZPO boundaries. The crystallite size of all the samples is shown in Table 6.1. The evolution of this secondary LTZPO phase is particularly

significant for the ionic conductivity of the composite electrolyte. While pure LLZCO provides a stable garnet framework, the presence of LTZPO at higher concentrations can enhance Li-ion transport by reducing interfacial resistance and creating fast conduction pathways [165].

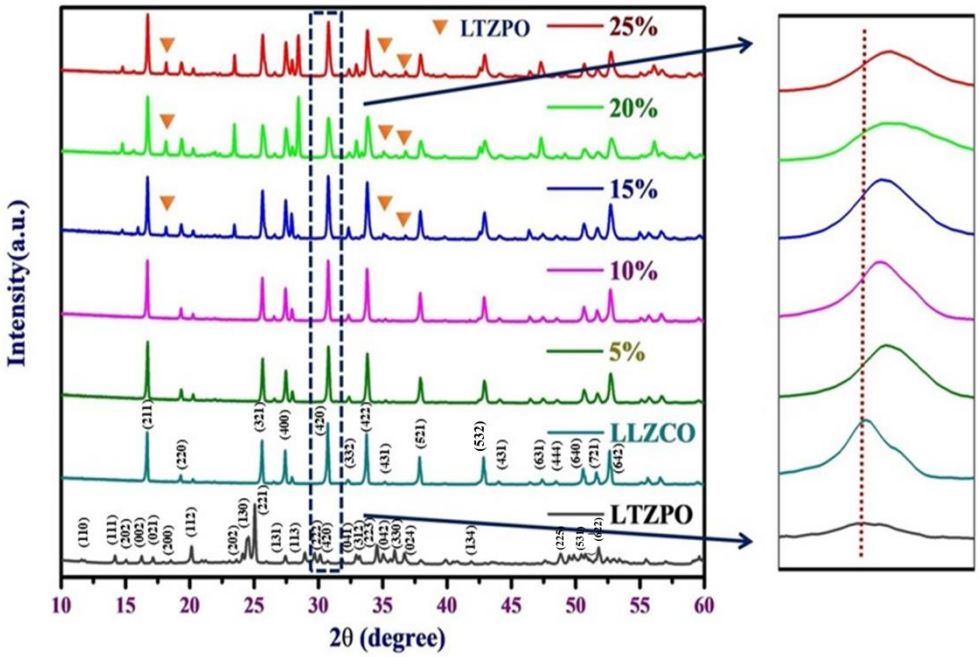

Fig 6.1 XRD pattern of LLZCO, LTZPO and C0-C5 Composite samples in the range of 10-60°

Table 6.1: Crystallite size of LTZPO and sample C0-C5

Ceramic	Crystallite Size (nm)
LTZPO	37.90053
C0	49.56223
C1	33.911

C2	37.90053
C3	53.69241
C4	24.78111
C5	30.68138

4

6.2.1.2 Scanning Electron Microscopy (SEM) and Energy Dispersive X-ray Spectroscopy (EDX) Analysis

Figure 6.2 (a)–(c) presents the cross-sectional SEM images of LLZCO, LTZPO, and the 15% composite pellet at 30KX. In Fig. 6.2 (a), the LLZCO sample shows a dense microstructure with well-formed grains but distinct grain boundaries. Figure 6.2 (b) shows the SEM image of the LTZPO sample, which reveals a comparatively different morphology from LLZCO with a smooth glassy-like surface with densely packed particles consistent with its role as a fast-ion conductor and the relative density of the dense pellets comes out to be 92%, supporting the evidence of the dense structure [168]. Figure 6.2 (c) shows the image of C3 composite pellet demonstrating the coexistence of both phases, with LTZPO appearing to be segregated preferentially along selected grain boundaries of LLZCO. This intergranular distribution is crucial as it effectively passivates high-resistance boundaries and establishes continuous Li-ion conduction pathways across the microstructure, forming a continuous or semi-continuous interfacial layer at cumulative grain junctions. The resulting morphology differs significantly from both parent materials and indicates improved grain contact and interfacial connectivity. Figure 6.3 (a-q) shows the EDS image of all the samples, demonstrating the

homogeneous distribution of all elements in the pellets. Microstructural analysis provides evidence for the origin of the DRT peak related to microstructural heterogeneity and interfacial resistance arising from the LTZPO layer.

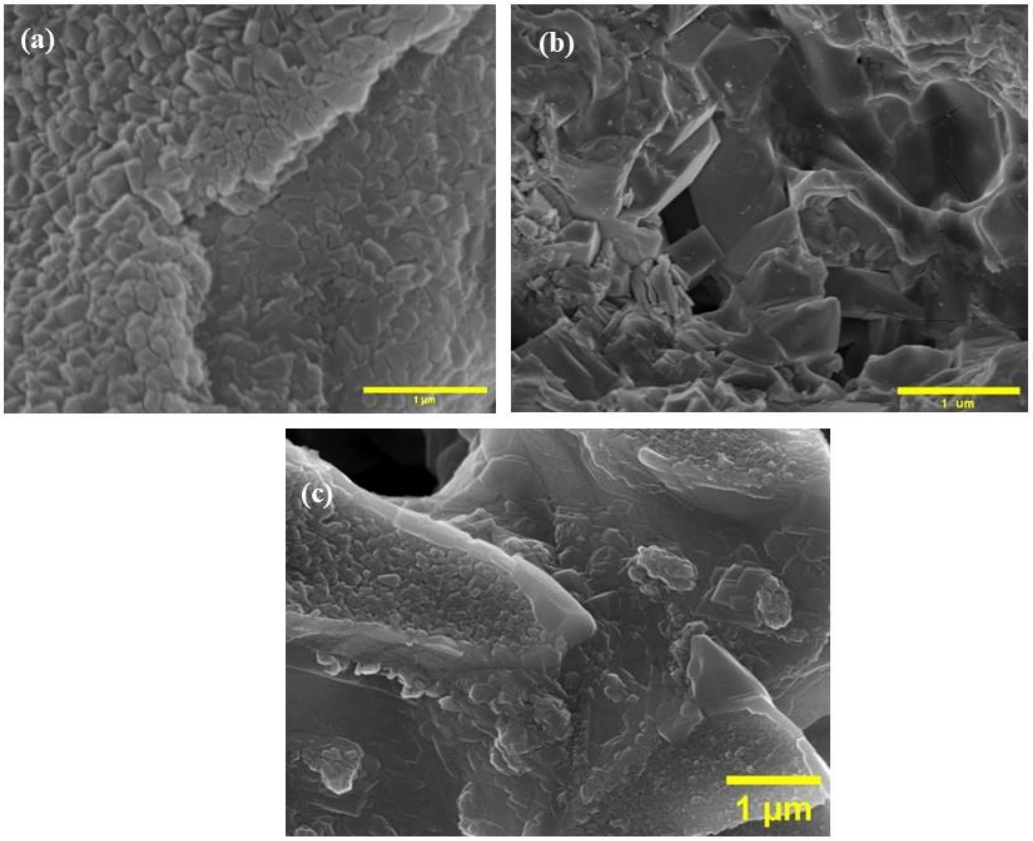

Fig 6.2 SEM Image of (a)LLZCO, (b)LTZPO and (c) C3 Ceramic at 30KX.

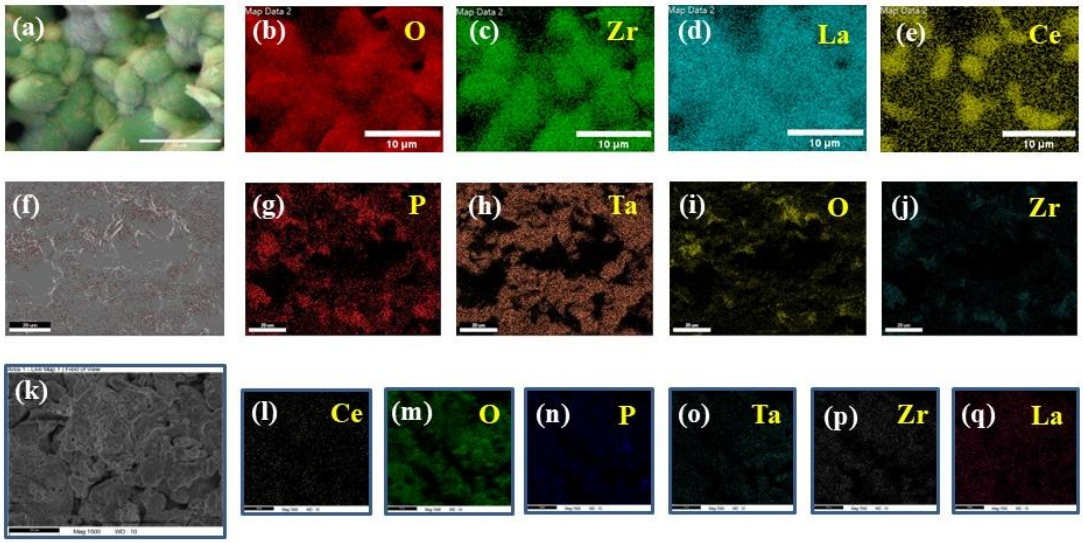

Fig 6.3 Elemental Mapping image of (a) LLZCO (b) O (c) Zr (d) La (e) Ce (f) LTZPO (g) P (h)T a (i) O (j) Zr (k) C3 Composite (l) Ce (m) O (n) P (o) Ta (p) Zr (q) La

6.2.2 Impedance Characterization

6.2.2.1 Impedance Spectroscopy and Distribution of Relaxation Times (DRT) Analysis

XRD confirms the presence and evolution of LTZPO phases in the LLZCO matrix, but does not directly quantify the transport behavior across composite ceramic. Impedance spectroscopy (IS) and its Distribution of Relaxation Times (DRT) analysis are done to find the high li ion conducting composite ceramic. The importance of impedance plot to DRT plot transition/requirement due to overlapping relaxation times of multiple physical processes inside the ceramic has been shown in chapter 5. Hence, in this chapter DRT Analysis is used to deconvolute the overlapping processes inside the ceramic. Figure 6.4(a) shows the impedance plot, justifying that the lowest resistance value is of the C3 composite ceramic. Figure 6.4(b)-(g) represents the DRT spectrum of the sample C0-

C5, and the area under the curve of DRT peaks depicts the resistance of a particular physical process. With increasing LTZPO content up to 15 wt%, a systematic decrease in overall resistance is observed; resistance values are shown in Table 6.2, concluding the total conductivity of the composite as 3×10^{-4} S/cm. This conductivity is attributed to the formation of a beneficial interfacial network between LLZCO and LTZPO, where the secondary LTZPO phase is preferentially distributed along grain boundaries and interfaces. In this composition range, LTZPO acts as an intergranular modifier that improves interparticle contact, suppresses resistive boundary barriers, and provides high ionically conducting pathways. At higher LTZPO loadings, more than 15% excessive accumulation of the LTZPO phase at grain boundaries can partially disrupt the LLZCO conduction framework. This over-segregation introduces heterogeneity and blocks continuous fast-ion pathways, leading to increased interfacial impedance. Further, Fig. 6.4 (h) shows the temperature-dependent impedance plot of C3 Composite Ceramic ranging from 30 to 90 ºC. It shows the negative temperature coefficient of resistance (NTCR) behavior, resulting in increased conductivity of the sample with temperature. Figure 6.4 (i) shows the DRT Spectrum of C3 Ceramic at 30 ºC, showing 7 different peaks that correspond to different relaxation processes. The first two peaks appearing near 10^{-7} s and 10^{-6} s correspond to the two fastest relaxation processes due to bulk lithium-ion conduction within the LLZCO grains. The third peak observed around 10^{-5} s is due to nanoscale heterogeneities, including Maxwell-Wagner-type polarization arising from local variations in dielectric and transport properties. Fourth Peak at 10^{-4} s arises due to the dominant contribution from grain boundary resistance and associated space-

charge layer effects, which is due to the contribution of a LTZPO dominance as shown in XRD patterns. The fifth, sixth and seventh peaks electrode and electrode/electrolyte interfacial polarization, which arises from capacitive lithium-ion accumulation and diffusion processes governed by the blocking nature of the electrodes. [153-161]. Figure 6.5 (a,h) shows the separate DRT pattern at different temperatures. As the temperature increases, all the relaxation peaks in the DRT spectra shift systematically toward shorter relaxation times, indicating faster lithium-ion dynamics at elevated temperatures. This shift reflects the reduction in activation energy for ion hopping and increased carrier mobility validated from NTCR behaviour of the composite shown in impedance plot in Fig. 6.4 (h) [169].

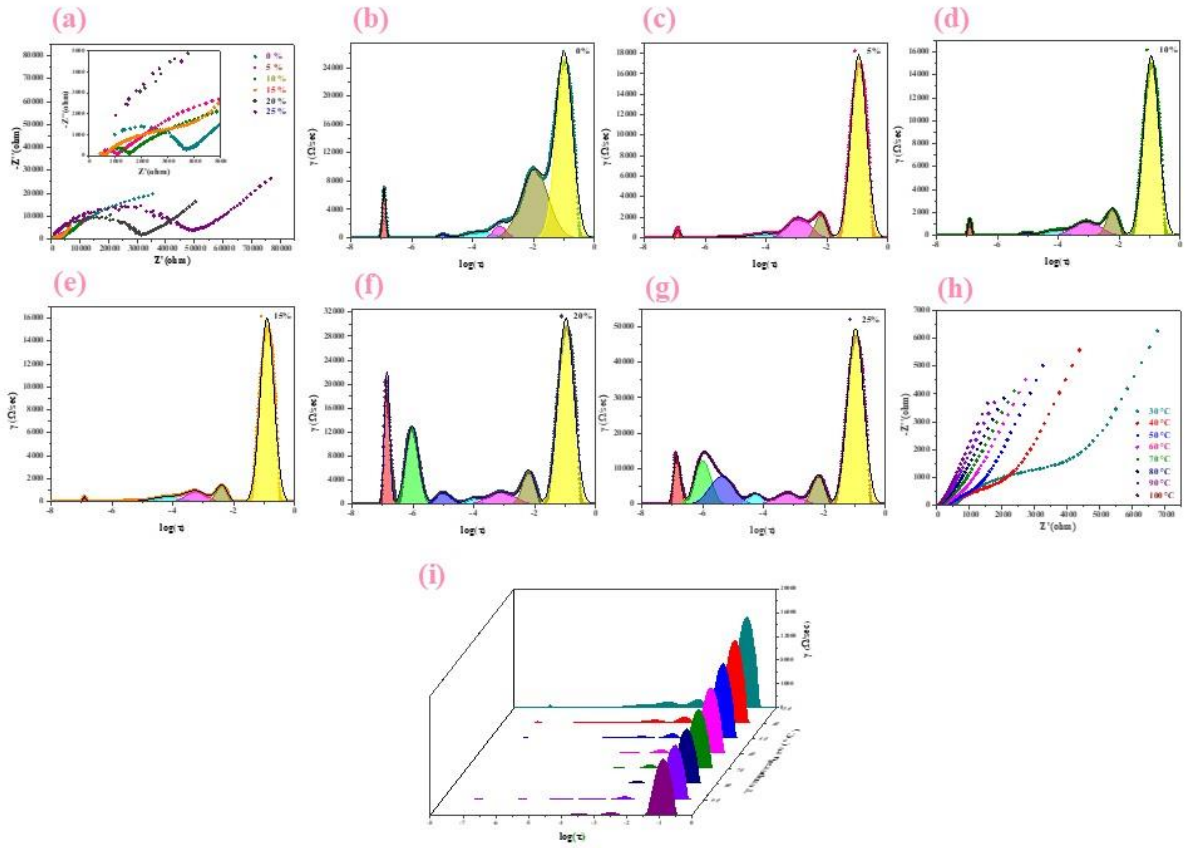

Fig. 6.4 (a) Impedance spectra of sample C0-C5, (b)-(g) DRT spectrum of composite at different concentration, (h) temperature-dependent impedance spectra of C3 composite, (i) temperature-dependent DRT spectra of C3 composite.

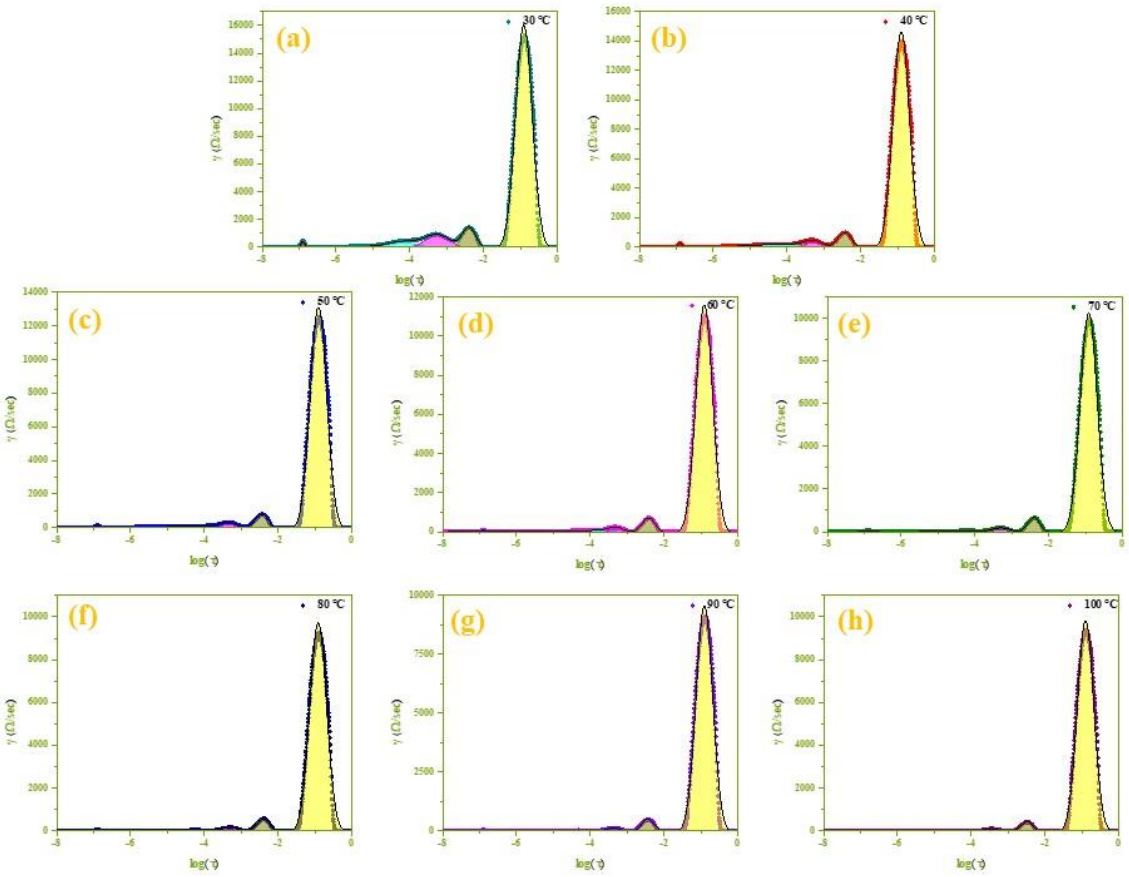

Fig 6.5 DRT(Distribution of Relaxation Time) Spectrum of C3 Composite at (a)30 °C (b)40 °C (c)50 °C (d)60 °C (e)70 °C (f)80 °C (g)90 °C (h)100 °C

Table 6.2 Value of resistances for sample C3

Peak	**Resistance(ohms)**
1	227
2	93
3	358
4	996
5	797.12
6	1829

7	18878

6.2.3 Electrical Characterization

6.2.3.1 Chronoamperometry

The chronoamperometry curve of the composite system is shown in fig. 6.6. After two hours of constant voltage input, the composite sample exhibits a low I_{SS} of 9.6 $\times 10^{-6}$ mA, which results in electronic conductivity (σ_e) of 1.8 $\times$ 10^{-8} S cm^{-1}. A low value of electronic conductivity indicates that the composite system is well established and can suppress the dendritic growth in Li-ion batteries.

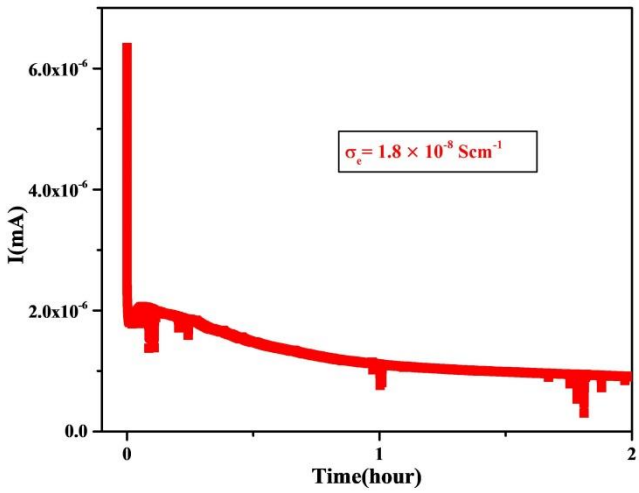

Fig 6.6 Chronoamperometry of composite pellet

6.2.3 Electrochemical Performance Analysis of LLZCO and LTZPO Composite Solid-State Electrolyte

6.2.3.1 Electrochemical Impedance Spectroscopy (EIS) Analysis

To elucidate the electrochemical performance of the composite solid-state electrolyte, an electrochemical analysis has been performed in an all- solid-state cell. To reduce the interfacial resistance and improve the interfacial Li ion kinetics, a C3 sintered pellet was coated with Al, as shown in Fig. 6.7 (a), and then Li metal was ~~is~~ melted over its surface to increase the contact area in our lab-designed setup. The Atomic Force Microscopy (AFM) Technique was used to study the roughness and surface morphology of the pellet surface before and after Al coating. The 2-D & 3-D AFM View on the C3Pellet before and after coating is shown in Fig.6.7 (b,c). Figure 6.7 (d,e) shows the cross sectional SEM- EDS images of pellets confirming the homogenous distribution of Al metal over the electrolyte surface. Roughness analysis using average surface root-mean-square roughness before and after coating reveals that the average roughness decreased from 140 nm to 52 nm, respectively. The larger roughness values signify uneven and rough surface, which results in poor contact, constituting non-uniform current distribution, which ultimately results in dendrite formation and reducing composite life [170]. Lithium wettability of the pellet is interlinked with surface roughness, as the surface roughness decreases, the surface energy increases, simultaneously increasing the contact angle, resulting in increased wettability over the surface of the ceramic electrolyte [171]. Figure 6.7 (f) shows the EIS plot of the symmetric cell before and after Li Melting. The reduction in total resistance from ~4K Kohm to ~3.5 Kohm is observed in the Nyquist plot after melting, that enhances the overall Li ion kinetics

6.2.3.2 Galvanostatic Charge-Discharge (GCD) Analysis

To elucidate the charging-discharging performance of the composite solid state electrolyte, electrochemical analysis has been performed in all solid state symmetric cell (Li|Al|C3|Al|Li) and full cell (LFP|C3|A|Li). Fig. 6.7 (g) demonstrates improved Li ion kinetics validated by low polarization voltage ~0.3V maintained over 140h at 100 $\mu A/cm^2$ current density. Figure 6.7 (h) shows a galvanostatic charge-discharge profile of a full cell with $LiFePO_4$ cathode and Li metal as anode in a CR2032 coin cell in 2.8 to 3.9 V at 0.1 C, with charge and discharge capacity calculated to be 136 mAh g^{-1} and 125 mAh g^{-1}, respectively. Figure.6.7 (i) shows that after cycling the cell for 80 cycles, cell shows the stable charge and discharge capacity of 75 mAh g^{-1} and 73 mAh g^{-1} with the efficiency of 98.39 %.

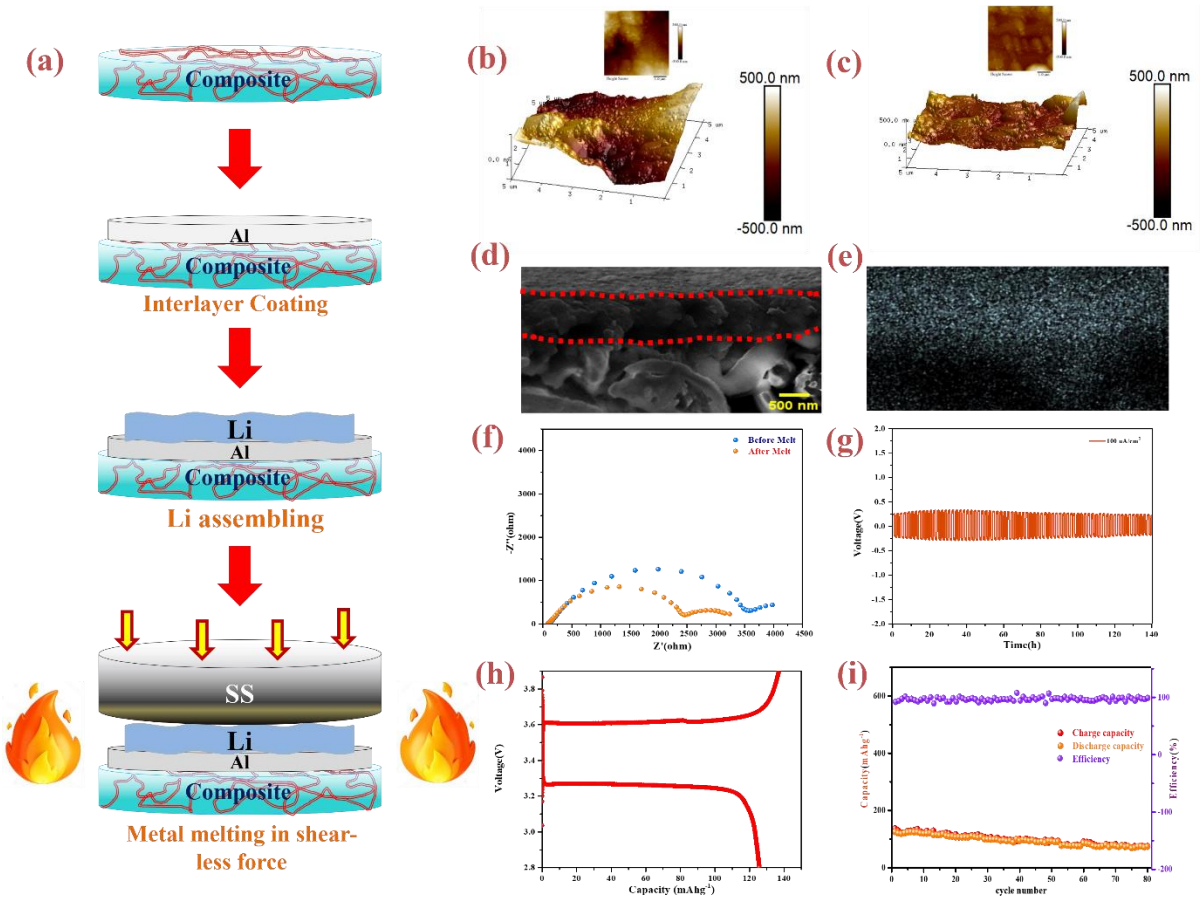

Fig. 6.7 (a) Illustration of process of Li melting in Al coated C3 pellet, (b)-(c) 2-D and 3-D AFM view of C3 pellet before and after coating, (d)-(e) Cross-section SEM and EDS of Al deposited C3 pellet, (f) The nyquist plot of Al coated C3 pellet before and after Lithium melting (g) Galvanostatic charge-discharge profile of a full-cell with $LiFePO_4$ cathode and Li-metal as anode, (h) Cyclic performance of a full-cell with $LiFePO_4$ cathode and Li-metal as anode.

In summary, LTZPO and LLZCO were synthesized using conventional solid state route and series of composite electrolyte is prepared with different weight percentage ranging from 0 to 25% of LTZPO in LLZCO. Structural analysis shows the evolution of LTZPO

phase in LLZCO with varying concentration describing the observable presence of LTZPO at 15%. Morphological analysis shows the presence of heterogeneous morphology in composite ceramic indicating the presence of both the materials. Impedance Analysis combined with DRT analysis of composite pellets shows the evolution of various resistance via LTZPO mxing confirming the lowest resistance value of sample C3. Further electrochemical performance has been studied in Half-Cell and Full Cell all solid state battery without using any liquid at the interfaces, symmetric cell cycled over 140h with stable overpotential voltage and full cell delivers a discharge capacity of 73 $mAhg^{-1}$ with the efficiency of 98.39 % after 80 cycles.

Chapter 7

Conclusion, Future Scope and Social Impact

This chapter includes the summary of the results obtained in the current research and discusses its social impact and future scope.

7.1 Conclusion

In this research investigation, a comprehensive study of the physicochemical and electrochemical performance of garnet-type solid electrolyte (LLZO, LLZCO) and phosphate-type (LTPO, LTZPO) has been investigated using a low-cost synthesis route. Moreover, the extensive research has been carried out involving doping and composite formulations. These studies aim to enhance and analyze the structural, morphological, and electrochemical properties of the synthesized electrolyte materials. Initially, synthesis and electrochemical analysis of the LTPO solid electrolyte were carried out using the solid-state reaction route. Thermogravimetric (TGA) and differential scanning calorimetry (DSC) analyses up to 1100°C were conducted to determine the optimal temperature range for phase formation, stepwise sintering, and mass loss assessment utilizing the first derivative of mass loss. The TGA results indicate an 8.4% total mass loss up to 1100°C. Thus, temperatures 1100 °C and 1050 °C have been utilized for multi step sintering. XRD analysis confirmed the formation of the monoclinic LTPO and secondary minor trigonal $LiTaO_3$ phase during different step sintering schedules. At the same time the resulting material exhibited optimal relative density, a dense microstructure, heterogeneous grain distribution when subjected to high-temperature step sintering at 1100°C for 2 hours and 1050°C for 4 hours, and the presence of $LiTaO_3$ secondary phase at the grain boundary after step sintering is confirmed using TEM. Dielectric studies revealed Maxwell-Wagner relaxation, with the dielectric dispersion of ε' and ε'' in the frequency range of 1 MHz to 4 Hz.

Impedance analysis identified two distinct semi-circular arcs, correlating grain and grain-boundary contributions to relaxation processes, further validating the Maxwell-Wagner relaxation mechanism. The AC conductivity study has indicated two conduction mechanisms, governed by the CBH and OLPT models, clarifying the role of grains and grain boundaries in charge transport. LTPO exhibits the total ionic and electronic conductivity as 0.4 x 10^{-5} Scm^{-1} and 1.22 x 10^{-8} Scm^{-1},respectively with the highest relative density of 82.4%. To enhance electrochemical performance, a buffer layer($LiPF_6$ soaked polypropylene membrane) was introduced at the electrolyte/electrode interface, improving contact and preventing electrically conductive phase in LTPO. A quasi-solid-state battery demonstrated an initial discharge capacity of 92 mAh g^{-1}, retaining 65 mAh g^{-1} after 10 cycles. To further tailor ionic transport properties, Zr-doping in LTPO (LTZPO) has been systematically investigated. XRD confirmed the stabilization of the modified monoclinic structure with slight lattice expansion due to Zr substitution. SEM analysis demonstrated improved densification and reduced porosity for optimized compositions LTZPO-0.1($Li_{1.1}Ta_{1.9}Zr_{0.1}PO_8$). Impedance results revealed reduced total resistance and temperature-dependent studies confirmed the enhanced ionic conductivity as 0.24 x 10^{-4} Scm^{-1} with low electronic conductivity 0.3 x 10^{-8} Scm^{-1} and the increased density of 87%. Symmetric Li|LTZPO|Li cell testing exhibited remarkable electrochemical stability for up to 1500 hours, indicating improved interfacial compatibility and structural robustness. The conduction mechanism remained dominated by CBH and OLPT processes, highlighting the role of dopant-induced defect chemistry in modifying lithium-ion mobility. Electrochemical performance of LTZPO-0.1 shows

the highly stable charging-discharging performance in Li|Li symmetric cells using a buffer layer at the electrolyte/electrode interface, improving contact and a quasi-solid-state battery demonstrated an initial discharge capacity of 88 mAh g^{-1}, retaining 81 mAh g^{-1} after 20 cycles. Further, Ce-doped garnet-type LLZO was synthesized using a multi-step sintering approach to stabilize the cubic phase with high densification. XRD confirmed cubic garnet phase formation with minor $Ce_{0.8}La_{0.2}O_{1.9}$ secondary phase. Optimized sintering achieved a relative density of ~79% for $Li_7La_3Zr_{1.75}Ce_{0.25}O_{12}$. Impedance deconvolution using Distribution of Relaxation Time (DRT) analysis enables the resolution of bulk and grain-boundary impedance contributions and reveals the dominant influence of grain-boundary impedance on Li-ion transport with the ionic conductivity of 0.5 x 10^{-4} Scm^{-1}. The chronoamperometry results shows the low electronic conductivity values for LLZCO as 1 x 10^{-4} Scm^{-8}. Symmetric cell Li|LLZCO|Li test with buffer layer demonstrated stable cycling for ~700 hours with the overpotential of ~0.05 V. Full cell configuration delivered a discharge capacity of ~110 mAh g^{-1} after 24 cycles. Finally, a composite electrolyte system made of LLZCO (at Ce-0.25) and LTZPO (at Zr-0.1) has been designed to overcome the grain-boundary bottleneck. Hence, the phase coexistence was verified by XRD analysis when the weight percent of LTZPO increased above 10% in LLZCO. The distribution of LTZPO along the LLZCO grain boundaries was revealed by SEM and quantitatively analysed with DRT indicates the successfully altered intergranular ionic transport pathways resulting into the increased ionic conductivity values of LLZCO system from 0.5 x 10^{-4} $Scm^{-1}$to 3 x 10^{-4} Scm^{-1} and increment in relative density values from 79% to 92%. Electrochemical

performance of LLZCO@LTZPO composite electrolyte system has been performed using Al interlayer at the electrode/electrolyte interface replacing the use of $LiPF_6$ buffer layer and converting the quasi solid state configuration of battery to all solid state battery configuration. All solid state symmetric cell testing of LLZCO@LTZPO system shows the reduced overpotential of ~0.35 V and steady cycling over 140 hours. Moreover, all solid state full cell performance showed a discharge capacity of 95.8 mAh g^{-1} after 80 cycles, confirming the composite construction is a viable way to improve electrochemical stability in an all-solid-state battery system. Based on the ionic conductivity, electronic conductivity and electrochemical performance of all the electrolyte materials, it can be suggested that LLZCO@LTZPO ceramic solid-state electrolyte materials shows the adequate performance in the all solid state battery and have the potential to replace liquid electrolyte materials.

7.2 Future scope

- **Interface Optimization:** Design of multifunctional buffer layers to suppress interfacial resistance and lithium dendrite formation.
- **Other Sintering Routes:** Explore other sintering routes, such as spark plasma sintering, laser abilation or field-assisted sintering methods to reduce sintering temperature and improve densification.
- **Scalability Assessments:** Translate pellet-scale synthesis to tape casting or thin-film processing for industrially relevant architectures.

- **Polymer Electrolyte:** Use of ceramic electrolytes as a filler polymer matrix to further increase their strength and properties and finally, to be use in solid-state battery.
- **Long-term Cycling:** Evaluate symmetric-cell stability for more than 2000 h at various temperatures and full cell performance for LTZPO, LLZCO and LLZCO@LTZPO composite ceramic electrolytes.

7.3 Social Impact

- Solid electrolytes eliminate flammable and dangerous liquid electrolytes, reducing thermal runaway risks.
- Improved cycling stability supports for batteries used for EV and grid storage systems.
- The development of high-performance solid-state lithium batteries would be supportive for renewable-energy integration and develop sustainable systems.
- More efficient batteries would accelerate the adoption of electric mobility & renewable energy sectors.
- Advances in solid-state battery materials contribute to national leadership in next-generation energy technologies.